

Review

Recent Progress on Transition Metal Based Layered Double Hydroxides Tailored for Oxygen Electrode Reactions

Jing Wang¹, Heng Kong², Haihong Zhong^{1,*}, Yu Jiang², Fei Guo²,
Nicolas Alonso-Vante³ and Yongjun Feng^{1,*}

¹ State Key Laboratory of Chemical Resource Engineering, Beijing Engineering Center for Hierarchical Catalysts, Beijing University of Chemical Technology, Beijing 100029, China; wangjing2019127@163.com

² Beijing Municipal Construction Group Co., Ltd., A40 Xingshikou Road, Haidian District, Beijing 100195, China; hengkh@163.com (H.K.); jy558833@163.com (Y.J.); guofei2007@163.com (F.G.)

³ Institut de Chimie des Milieux et Matériaux de Poitiers (IC2MP), UMR-CNRS 7285, University of Poitiers, 86073 Poitiers, France; nicolas.alonso.vante@univ-poitiers.fr

* Correspondence: hzhong@buct.edu.cn (H.Z.); yjfeng@mail.buct.edu.cn (Y.F.); Tel.: +86-106-443-6992 (Y.F.)

Abstract: The oxygen reduction reaction (ORR) and oxygen evolution reaction (OER), namely, so-called oxygen electrode reactions, are two fundamental half-cell reactions in the energy storage and conversion devices, e.g., zinc–air batteries and fuel cells. However, the oxygen electrode reactions suffer from sluggish kinetics, large overpotential and complicated reaction paths, and thus require efficient and stable electrocatalysts. Transition-metal-based layered double hydroxides (LDHs) and their derivatives have displayed excellent catalytic performance, suggesting a major contribution to accelerate electrochemical reactions. The rational regulation of electronic structure, defects, and coordination environment of active sites via various functionalized strategies, including tuning the chemical composition, structural architecture, and topotactic transformation process of LDHs precursors, has a great influence on the resulting electrocatalytic behavior. In addition, an in-depth understanding of the structural performance and chemical-composition-performance relationships of LDHs-based electrocatalysts can promote further rational design and optimization of high-performance electrocatalysts. Finally, prospects for the design of efficient and stable LDHs-based materials, for mass-production and large-scale application in practice, are discussed.

Keywords: layered double hydroxides (LDHs); bifunctional electrocatalysts; electrocatalysis; oxygen reduction reaction (ORR); oxygen evolution reaction (OER)



Citation: Wang, J.; Kong, H.; Zhong, H.; Jiang, Y.; Guo, F.; Alonso-Vante, N.; Feng, Y. Recent Progress on Transition Metal Based Layered Double Hydroxides Tailored for Oxygen Electrode Reactions. *Catalysts* **2021**, *11*, 1394. <https://doi.org/10.3390/catal11111394>

Academic Editors: Alessandro Di Michele and Carlo Pirola

Received: 29 October 2021

Accepted: 16 November 2021

Published: 18 November 2021

Publisher's Note: MDPI stays neutral with regard to jurisdictional claims in published maps and institutional affiliations.



Copyright: © 2021 by the authors. Licensee MDPI, Basel, Switzerland. This article is an open access article distributed under the terms and conditions of the Creative Commons Attribution (CC BY) license (<https://creativecommons.org/licenses/by/4.0/>).

1. Introduction

The excessive consumption of fossil fuels and accompanying environmental issues, e.g., greenhouse effect and NO_x/SO_x pollutants emission, have caused serious effect on the development of global society. Under the “new policies” or “current policies” scenarios from the International Energy Agency (IEA), the world’s energy demand will increase from 12 TW in 2009 to 17 or 18 TW by 2035, respectively, accompanied by CO₂ emissions soaring from 29 Gt yr^{−1} in 2009 to 36 or 43 Gt yr^{−1} in 2035 [1]. Consequently, the exploitation and use of renewable, and sustainable energy sources, such as solar, wind, biomass, and tide, are of vital importance in reducing the dependence on fossil fuels [2–5].

Hydrogen (H₂), an ideal and zero-carbon energy carrier with high heat value (142 MJ kg^{−1}) and energy conversion efficiency has been considered as the most promising candidate to replace fossil fuels in the twenty-first century [6–8]. Recently, electrochemical water splitting is regarded as a highly efficient and sustainable H₂ production technology, in which the generated electricity from renewable energy sources is stored in the form of chemical energy: 2H₂O + energy → 2H_{2(g)} + O_{2(g)} [9]. The produced H₂ can be further converted into electricity: 2H_{2(g)} + O_{2(g)} → 2H₂O + electricity, in fuel cells (FCs) system. The pivotal processes of energy storage and

conversion devices like fuel cells, and metal-air batteries (MABs) are four electrochemical “half-reactions”, namely, hydrogen evolution reaction (HER), hydrogen oxidation reaction (HOR), oxygen reduction reaction (ORR), and oxygen evolution reaction (OER) [10–12]. Alkaline HER process involves, in alkaline electrolyte, the water dissociation, namely, the two-electron transfer HER ($2\text{H}_2\text{O} + 2\text{e}^- \rightarrow \text{H}_2 + 2\text{OH}^-$) at the cathode of electrochemical water splitting device, whereas the anodic OER shows a more complex reaction mechanism involving four-electron- OH^- -coupling processes ($4\text{OH}^- \rightarrow \text{O}_2 + 2\text{H}_2\text{O} + 4\text{e}^-$). The formation of various OER intermediates (O_{ad} , OH_{ad} , and OOH_{ad}), as well as adsorption/desorption of oxygen molecules, which leads to a sluggish kinetics and high overpotential (η) [13]. The OER mechanism depends mainly on the surface property of the catalyst. There are several proposed possible mechanisms for OER, i.e., traditional adsorption evolution mechanism (AEM) and a lattice-oxygen-mediated mechanism (LOM) [14]. For example, the traditional adsorption evolution process, in alkaline environment, can be described by the following steps (“*” denotes an active site): (i) OH^- species is adsorbed on the electrode surface, and form the *OH intermediate ($\text{OH}^- + * \rightarrow *\text{OH} + \text{e}^-$); (ii) generated *OH intermediate interacts with OH^- to produce *O specie ($*\text{OH} + \text{OH}^- \rightarrow *\text{O} + \text{H}_2\text{O} + \text{e}^-$); (iii) the *O specie is combined with OH^- , forming *OOH intermediate; (iv) the above *OOH intermediate is further oxidized to O_2 molecule ($*\text{OOH} + \text{OH}^- \rightarrow \text{O}_2 + \text{H}_2\text{O} + \text{e}^- + *$) [14]. In comparison with the AEM, the existence of lattice oxygen is found in the LOM process. Initially, the OH^- species on two neighboring metal sites undergo deprotonation and form metal-oxo intermediates. Next, the metal-oxo intermediates directly couple to form O-O bond instead of producing *OOH species. Finally, the molecular oxygen (O_2) is released with the generation of two oxygen vacancies, which are subsequently occupied by OH^- for a continuous OER process [14]. To achieve low overpotentials, extensive efforts have been devoted to developing highly efficient electrocatalysts with optimal binding energy for OER intermediates to reduce the reaction energy barrier, and thus accelerate the reaction rate [15].

Until now, the benchmark electrocatalysts towards OER are precious metal materials, such as ruthenium oxides (RuO_2) and iridium oxides (IrO_2) [16–18], but their high cost and scarcity hinder their industrial use [19–21]. Therefore, the development of non-precious electrocatalysts towards OER, with high efficiency, excellent electrical conductivity, abundant active surface, as well as structural stability, is crucially important to achieve large-scale commercial application of clean energy infrastructures. The first 3d transition metals such as Mn, Fe, Co, and Ni oxides [22–29]; hydroxides [30–35]; phosphides [36–42]; chalcogenides [43–48]; and layered double hydroxides (LDHs) [49–56] have aroused great interest in the OER as potential alternatives to precious metals due to their intriguing intrinsic activity and stability. It is worth mentioning that one of the first reports, in 1983, on the electrocatalytic performance of metal hydroxides, revealed a good OER activity of α -Ni(OH)₂ [57], and it was further confirmed that the Fe impurities in the α -Ni(OH)₂ greatly lower the OER overpotential [58,59]. Since then, the LDHs of 3d iron group metals (Fe, Co and Ni)—such as Ni-Fe [60–64], Ni-Co [65–68], Co-Ni [69–71], Fe-Ni [72–74], Fe-Co [75–78], and Co-Co [79–82]—and the corresponding derivatives—e.g., NiFe₂O₄ [83–86], CoFe₂O₄ [87], NiCo₂O₄ [88,89], and Co₃O₄ [90–92]—have been employed as OER or bifunctional ORR/OER electrocatalysts with high kinetics in alkaline solution.

Several review articles have summarized the multidimensional applications of LDHs including energy storage and conversion [21,93,94]. For example, Gong’s group [95] published a mini review in 2014, which was focused on the early discovery and recent progress on NiFe-LDHs for OER electrocatalysis in terms of chemical properties, synthetic methodologies, as well as catalytic performances. Kundu and co-workers [93] provided a detailed review with insights on the structure, activity, and mechanism of LDHs and layered-oxide materials in the electrochemical and photoelectrochemical water oxidation. Recently, a review by Sun’s group [50] covered the identification of active sites in LDHs materials at the atomic level for the OER, the superaerophobic nanoarray electrode assembly as well as the current optimization strategies of active sites. However, there is still a lack of a comprehensive review on the functionalization strategies of LDHs and their derivatives as OER or ORR/OER bifunctional electrocatalysts.

Herein, we summarize the most recent advances in the functionalization strategies, structural performance and chemical-composition-performance relationships of transition metal based LDHs and corresponding derivatives served as catalysts in the OER electrocatalysis in alkaline medium. Specifically, common functionalization strategies involving LDHs are designed into the following major categories, in Figure 1, namely: (1) layer composition tuning; (2) intercalation; (3) vacancy engineering; (4) ultrathin nanosheets; (5) nanostructuring; and (6) hybridization. In addition, the application of LDHs-based materials used as bifunctional ORR/OER electrocatalysts is also shown. Finally, we briefly point out the remaining challenges to achieve large-scale commercial applications of renewable energy storage and conversion devices, as well as opportunities in developing advanced, efficient, and stable transition metal-based LDHs materials towards ORR and OER processes.

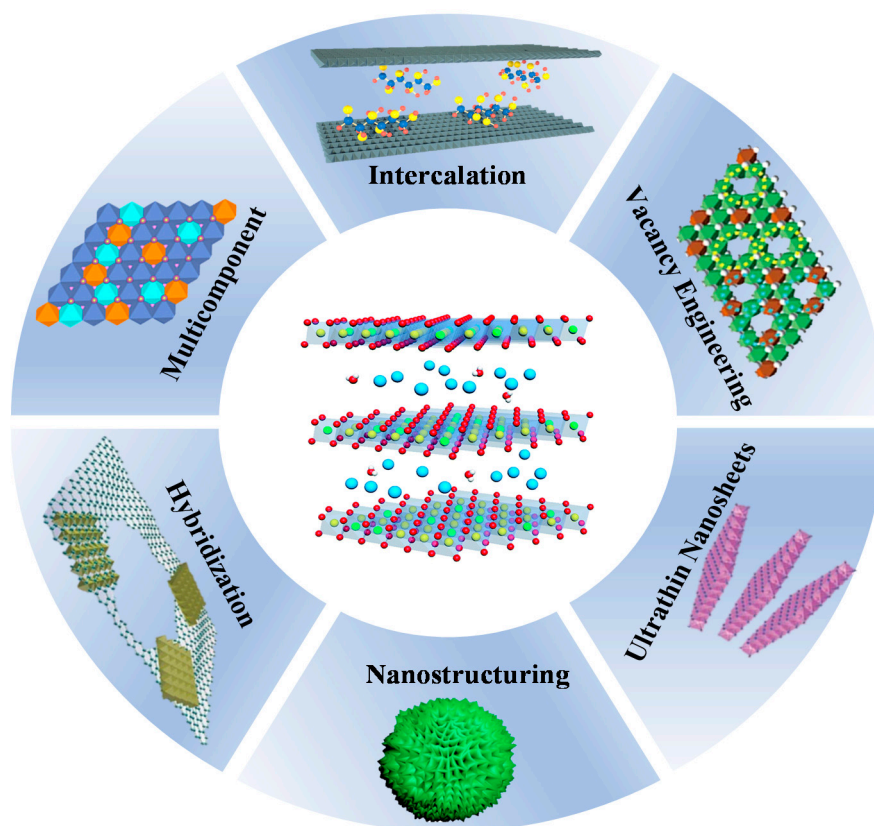


Figure 1. The design of the different modification strategies for LDHs materials.

2. Fundamental Characteristics of LDHs

Layered double hydroxides (LDHs) or hydrotalcite-like compounds, are a typical kind of two-dimensional (2D) layered anionic clay materials [96,97], which can be described by a generic formula $[M^{II}_{1-x}M^{III}_x(OH)_2(A^{n-})_{x/n} \cdot yH_2O]$, where M^{II} and M^{III} represent the divalent (e.g., Mg^{2+} , Co^{2+} , Ni^{2+} , Cu^{2+} or Zn^{2+}) and trivalent (e.g., Al^{3+} , Fe^{3+} , or Cr^{3+}) metal cations, respectively; A^{n-} is the interlayer anion (e.g., CO_3^{2-} , NO_3^- , Cl^- , SO_4^{2-} or HPO_4^{2-}) compensating the positive charge of the host-sheet; x is the molar ratio of $M^{II}/(M^{II} + M^{III})$ and generally ranges from 0.20 to 0.33; y is the amount of molecular H_2O [98,99]. Within the 2D structure, LDHs consist of the positively charged host sheets and the interlayer guests containing negatively charged anions and water molecules (Figure 2) [100]. Due to various host–guest assemblies and nanoarchitectures with versatile physico-chemical properties, LDHs have been proved to be promising candidates for a wide range of applications like flame retardant [101], anticorrosive coating [102,103], catalysis [104–106], and energy storage and conversion [107–109]. Particularly, in the OER

electrocatalysis, LDHs offer a number of advantages: (i) the tunable chemical composition, including the type of metal cations and molar ratio of $M^{II}/(M^{II} + M^{III})$, favors to improve the intrinsic catalytic activity or introduce the extra active sites; (ii) the exchangeable interlayer anions (A^{n-}) with large sizes can enlarge the interlayer region, resulting in the exposure of more inner active sites; (iii) the synergistic interaction between the highly dispersed M^{II} and M^{III} cations, in the host sheets, favors the enhancement of the electrocatalytic activity; (iv) the geometric morphology, coordination environment and surface defects of LDHs can be modulated by precisely designing and controlling the chemical compositions of LDHs, which not only provide unsaturated active centers, such as low-coordinated metal cations, corner or edge sites, but also improve the porosity and electronic conductivity; and (v) a series of mixed metal oxides (MMOs) with high electrocatalytic performance can be acquired from LDHs via topological structure transformation process.

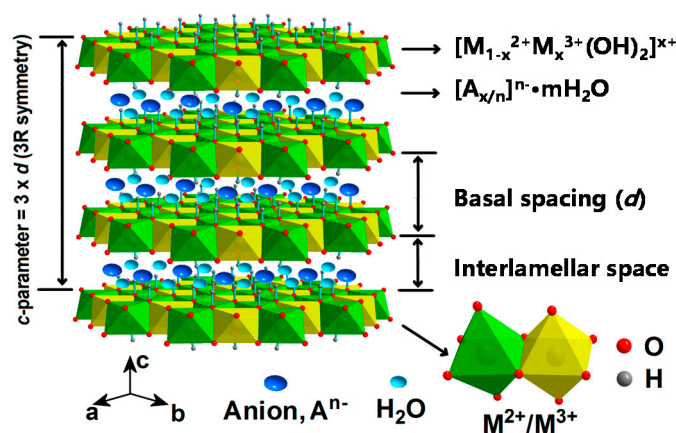


Figure 2. Schematic representation of the typical LDHs structure [100]. Copyright 2017, MDPI.

2.1. Binary LDHs

In mono-metallic hydroxides of divalent cations, the activity trend is directly correlated with the d -electron configuration. The decrease in the OER activity of $3d$ mono-metallic (oxy)hydroxides that followed the order: $Ni > Co > Fe > Mn$, was first reported by Subbaraman et al. [110], along with the increase in the oxophilicity of the $3d$ -M elements. Based on the interaction between $3d$ metal (oxy)hydroxides and OH_{ad} , the authors concluded that the OER reactivity trend was determined by the strength of $OH_{ad}-M^{2+\delta}$ (δ : valence state), with M ($Ni < Co < Fe < Mn$), and δ variation ($0 \leq \delta \leq 1.5$). When the interaction between OH_{ad} and metals was too strong, the reaction intermediates were stabilized, leading to a lower turnover frequency (defined as the number of complete reaction events per site per second). This was called “poisoning” effect of catalytic sites by preventing them from coordinating with hydroxide/oxyhydroxide ligands. Thus, among these $3d$ metals, Ni, with an optimal interaction strength with OH_{ad} , satisfied the Sabatier principle for OER catalyst design.

In addition, when other metal elements are incorporated in the mono-metallic hydroxides, the formed binary hydroxides possess near-optimal binding energies of O^* intermediates that facilitate the absorption/desorption for OER process, which is ascribed to the modulation of the local coordination environment and electronic structure [111]. In this context, Chen et al. [112] prepared Cu-doped cobalt hydroxide ($Cu-Co(OH)_2$) nanosheets with an excellent performance for OER. Interestingly, the Cu-doping favored the increase of the positive charge in the matrix of Co ions. The valence states of Co ions in $Cu-Co(OH)_2$ were $2 + \delta$ ($0 < \delta < 1$), higher than $2+$ as in $Co(OH)_2$, which tended to absorb OH^- and facilitates the formation of $Co^{(+)}-OH_{ad}$ and $Co-OOH$ species. Similarly, Qiao et al. [113] developed porous ZnCo-LDH nanosheets as an efficient OER electrocatalyst delivering a current density of $\sim 15.06 \text{ mA cm}^{-2}$ at $\eta = 0.54 \text{ V}$. It explained that the inactive Zn element, in the alternately distributed binary LDH host-sheets, played a key role in overlapping of

e_g orbital of active sites and $O-2p_\sigma$ orbital of reactant OH^- , which facilitated the formation of $\text{M}=\text{O}$ bonds, thus reducing the OER kinetic energy barrier. Similarly, an ultrathin amorphous cobalt-vanadium hydr(oxy)oxide (CoV-hydr(oxy)oxide) for water oxidation was synthesized by Liu et al. [114]. They suggested that the Co active sites with near-optimal energetics for OER in CoV-hydr(oxy)oxides could be attributed to the modification of the coordination environment of Co atoms caused by lattice mismatch, originating from the V-doping.

The NiFe-LDHs have recently documented to possess the highest OER catalytic activity and stability among the binary LDHs, especially when the Ni/Fe ratio is 3:1 [115]; which was firstly developed for OER electrocatalysis in 2013, thanks to the work of Gong and co-workers [116]. The active site for OER process in alkaline conditions on NiFe-LDHs has been studied and reported in many publications over the years. In the early 21st century, the so-called “Ni active site” mechanism was proposed, and then turned out to be that the Fe element was the active site (“Fe active site” mechanism); while some recent findings propose that the synergistic effect of Ni and Fe sites are responsible for the high OER activity. A pioneering study carried out by Bell’s group [117], probed the active sites of Ni-Fe films on the OER activity. They found that the Ni-Fe film, with a surface composition of 40% Fe, exhibited an enhanced OER activity that was roughly 2 orders of magnitude higher than that of a fresh Ni film. In addition, the in situ Raman spectra results demonstrated that the local environment of Ni-O, modified by Fe correlated with the increasing OER activity. These observations suggested that the OER was catalyzed by Ni in Ni-Fe films, and the incorporation of Fe gave rise to an increase in the potential at which $\text{Ni}(\text{OH})_2/\text{NiOOH}$ redox took place. Additionally, Trotochaud et al. [118] proposed that in a $\text{Ni}_{1-x}\text{Fe}_x\text{OOH}$ OER electrocatalyst, Fe played an activated effect on Ni active centers via a partial-charge-transfer mechanism, which led to a lower dependence of thickness for $\text{Ni}_{1-x}\text{Fe}_x\text{OOH}$ than NiOOH . This work showed that the incorporation of Fe-impurities was responsible for the dramatic increase in OER activity of aged $\text{Ni}(\text{OH})_2/\text{NiOOH}$ and held a view that β - NiOOH was less active for OER than the disordered γ - NiOOH .

Some research groups argued that, although iron ion existed in OER catalysts (NiFe oxides/(oxy)hydroxides) in the form of +3 oxidation state, it still acted as the main active site of the catalytic reaction [58,118,119]. Bell et al. [120] probed the short-range structure at Fe and Ni sites in electrodeposited (Ni,Fe) oxyhydroxide catalysts through operando X-ray absorption spectroscopy (XAS), using high energy resolution fluorescence detection (HERFD). They showed that a 500-fold increase in the OER activity originated from $\text{Ni}_{1-x}\text{Fe}_x\text{OOH}$ as compared with NiOOH and FeOOH . The in situ HERFD and XAS data revealed that Fe^{3+} , located in the octahedral sites with short Fe-O bond distances, was triggered by the edge-sharing with the surrounding $[\text{NiO}_6]$ octahedra. This explanation was reinforced by the density function theory with Hubbard U (DFT+U) calculations. More importantly, DFT+U calculations established that the active sites in $\text{Ni}_{1-x}\text{Fe}_x\text{OOH}$ for the oxidation of water were Fe^{3+} ions. These species presented an extremely lower overpotential than Ni^{3+} cations in either γ - $\text{Ni}_{1-x}\text{Fe}_x\text{OOH}$ or γ - NiOOH .

To elucidate the role of Fe cation in NiFe-LDHs with a metal molar ratio of 3:1, Chen et al. [121] carried out an operando Mössbauer spectroscopy study. Figure 3A displays the dynamic CV curves recorded in the operando cell, as well as the Mössbauer spectrum collected initially at the open-circuit potential (OCP), and then at 1.49 V, 1.62 V and 1.72 V, respectively. In Figure 3B, under the OCP, the Mössbauer spectrum showed a doublet with an isomer shift (δ) of 0.34 mm/s and quadrupole splitting (Δ) of 0.46 mm/s, which remained unchanged until 1.49 V, cf. Figure 3C. When the applied potential increased to 1.62 V, in Figure 3D, there was a new singlet at $\delta = -0.27$ mm/s, and the intensity reflected the oxidation of approximately 12% of the Fe sites in the material, which was conferred to the oxidized Fe species as Fe^{4+} . With an applied electrode potential of 1.76 V, a growth of this oxidized Fe peak with ~21% of the total Fe (Figure 3E) was observed. When the potential was returned to 1.49 V, the oxidized Fe peak was still evident in the Mössbauer spectrum (~20% of total Fe, Figure 3F). This work provides the obvious evidence for the

formation of Fe^{4+} in NiFe oxides during the OER process, suggesting that more attention is needed to be paid on the role of reactive Fe^{4+} species generated at edge, corner, or defect sites within Fe-doped NiOOH lattice. Bard et al. [122] reported the direct measurement of surface OER kinetics of Ni^{4+} and Fe^{4+} in NiOOH, FeOOH, and $\text{Ni}_{1-x}\text{Fe}_x\text{OOH}$ ($0 < x < 0.27$) by performing surface interrogation scanning electrochemical microscopy (SI-SECM). Two types of surface sites showing “fast” and “slow” OER kinetics were found in FeOOH and $\text{Ni}_{1-x}\text{Fe}_x\text{OOH}$ electrodes, where the fraction of “fast” sites in $\text{Ni}_{1-x}\text{Fe}_x\text{OOH}$ coincided well with the Fe atom content in the film, suggesting that the dispersed Fe atoms, in a NiOOH matrix, were indeed the active sites for OER process.

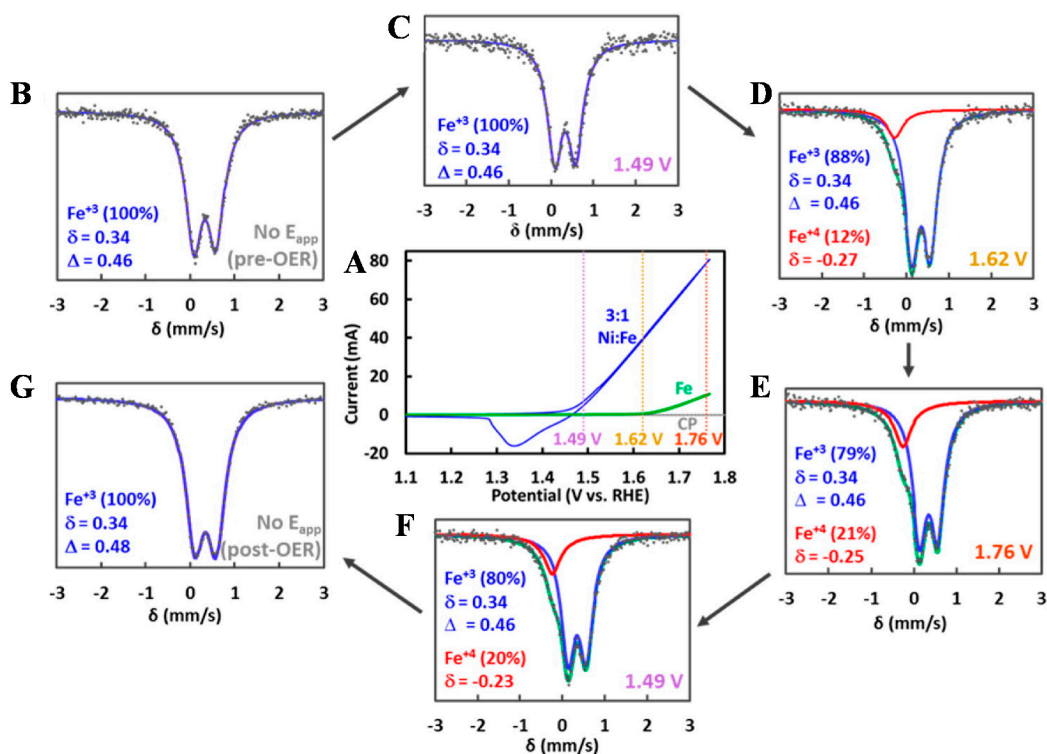


Figure 3. (A) CV curves of NiFe layered oxyhydroxide electrocatalysts used for the operando experiments with (B,G) Mössbauer spectra collected at open circuit (gray), at (C,F) 1.49 V (purple), (D) 1.62 V (yellow), and (E) 1.76 V (red). CV data were recorded in the Mössbauer-electrochemical cell with a scan rate of 25 mV/s prior to Mössbauer measurements [121]. Copyright © 2015 American Chemical Society.

Many reports have shown that the Fe ion that exist in the form of +3 oxidation state in the OER process, assist to accelerate the OER process, and improve the electrocatalytic performance [123–126]. Strasser et al. [123] explored the active metal redox states of Fe and Ni in amorphous NiFe oxyhydroxide by means of operando differential electrochemical mass spectrometry (DEMS) and XAS (Figure 4A,B). Under OER conditions in 0.1 M KOH, Ni centers were present in the +4 oxidation states at Fe content < 4 at%. However, Ni atoms were stabilized in low-valent +2 oxidation states at > 4 at% Fe contents, while the faradaic efficiency of O_2 was increased, suggesting that the OER active state could be designated as $\text{Ni}^{+2}\text{Fe}^{+3}\text{OOH}$. Nocera et al. [124] suggested that the incorporation of Fe^{3+} , as a superior Lewis acid into Ni oxide matrix, helped to increase the acidity of OH_x moieties and then engendered a greater population of Ni^{4+} , which in turn led to an increase in the oxyl character along with an enhanced activity of the catalyst in promoting OER. Based on in situ Raman spectro-electrochemistry, Edvinsson et al. [127] proposed that the synergistic electronic interplay between Fe and Ni is crucial for alkaline water splitting. As shown in Figure 4C–E, with increased overpotentials, on the NiFe LDHs, the $\text{Ni}(\text{OH})_2$ gradually converts to γ -NiOOH with a high OER reactivity. Compared with single $\text{Ni}(\text{OH})_2$ in

Figure 4C, the binary NiFe-LDHs showed a sluggish transition period from Ni(OH)₂ to γ -NiOOH at high overpotentials, indicating that the presence of Fe in the NiFe-LDHs inhibited the electrochemical oxidation of Ni(OH)₂ to γ -NiOOH. The authors suggested that at low overpotentials OH_{ad} was adsorbed at Fe sites to form FeOOH species whereas at high potentials it tended to be anchored at (or migrated to) Ni sites. It was explained that the electronic effect of Fe³⁺ could induce the formation of γ -NiOOH phase with a higher Ni valence state, and thus the OH_{ad} selectively adsorbed on Ni site to form O_{Had}-Ni ^{δ +} intermediate to accelerate the water dissociation (Figure 4E).

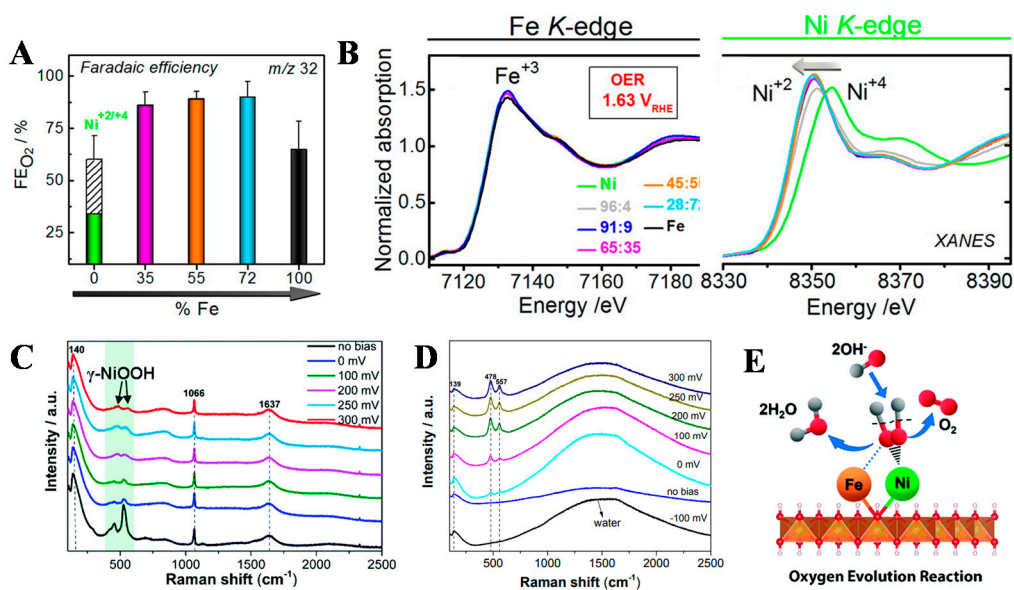


Figure 4. (A) Faradaic O₂ efficiencies of NiFe oxyhydroxide catalysts as a function of Fe-content (Ni_{100-x}Fe_x) given as atomic%. The hatched bar represented the O₂ efficiency excluding the charge associated with Q_{F,Ni+2/+3}, corresponding to the Ni(OH)₂/NiOOH redox process. The Faradaic O₂ efficiency was derived from FE_{O₂} (%) = Q_{F,O₂}^{DEMS} / Q_F^{tot}; (B) X-ray absorption spectra of the NiFe catalysts with varying catalyst composition (Ni_{100-x}Fe_x) freeze-quenched under application of catalytic potential after conditioning at 1.63 V for 30 min in 0.1 M KOH [123]. Copyright © 2016 American Chemical Society. (C) In situ Raman spectra collected in a large wavenumber region from NiFe-LDHs during OER process in 1 M KOH at various overpotentials vs. RHE; (D) In situ Raman spectra collected in 1 M KOH with different applied overpotentials vs. RHE from -100 mV to 300 mV for Ni(OH)₂ on Ni foam. The peaks appeared at ~478 ± 1 and ~557 ± 1 cm⁻¹, indicating the transformation of Ni(OH)₂ to NiOOH during oxygen evolution reaction in alkaline media; (E) the OER mechanism of NiFe LDH: OH⁻ from the aqueous electrolyte was adsorbed on the Ni²⁺ center at modest overpotentials (η ~ 200–300 mV), forming OH_{ad} intermediate on the Ni site [127]. Copyright © The Royal Society of Chemistry 2019.

Although in recent decades, numerous advanced ex- and in situ technologies as well as theory calculation have been employed to get an insight of the roles of Ni and Fe elements in determining the OER activity of NiFe-LDHs electrocatalysts, it still remains a matter of controversy as to the true active centers for OER electrocatalysis. Thus far, regarding to the roles of Ni and Fe in NiFe-LDHs system, there are several possibilities: (1) Ni is the active site and Fe plays an activated effect on it; (2) Fe is the active site and Ni provides a conductive support for OER process; and (3) Ni works with Fe to boost the OER activity.

3. Strategies to Functionalize LDHs

Although LDHs materials with unique properties have been proved to be promising candidates for OER catalysis, they still suffer from intrinsic drawbacks, e.g., low electrical conductivity (10⁻¹³–10⁻¹⁷ S cm⁻¹), poor intrinsic activity of active sites, and structural collapsibility. These factors limit the electrocatalytic performance improvement of LDHs materials. To overcome these constraints, various functionalization strategies were proposed, namely: (1) increasing the number of active sites (e.g., through increased mass

loading or improved catalyst structuring to expose more active sites per gram) and (2) improving the intrinsic activity of each active site. For example, by regulating the layer composition, through changing the metal components, relative molar ratio and oxidation state, the electronic structure can be optimized to improve the intrinsic active sites. The exfoliated LDHs nanosheets are prone to expose more active sites on the surface than the LDHs bulk, leading to a fast electron transfer process coupled to protons and rapid diffusion of reactants, thus accelerating the rate of the redox reaction. The construction of three-dimensional (3D) hierarchical nano-architecture of LDHs can remarkably facilitate the electron/charge transfer and the diffusion of reactants during the water oxidation.

3.1. Regulation of Layer Composition

The layer composition of LDHs is adjustable, i.e., the metal components, the relative molar ratio, and the chemical valence state can be modulated in the host-sheets, which can be achieved by adding reducing metal element(s) or replacing the metal element(s) with different metals. As mentioned in Section 2.1, the incorporation of additional cations into the metal hydroxides causes the lattice mismatch, modifying the coordination environment and the electronic structure of active sites. Taking NiFe-LDHs as a benchmark for OER catalysis, in which Fe^{3+} centers are atomically surrounded and isolated by Ni^{2+} sites to form Ni-O-Fe motifs; there are several representative studies involving doping with a third metal cation selected from $\text{M}^{\text{II}} = \text{Co}^{2+}, \text{Mn}^{2+}, \text{Fe}^{2+}$ and $\text{M}^{\text{III}} = \text{Fe}^{3+}, \text{Co}^{3+}, \text{Cr}^{3+}, \text{V}^{3+}$.

According to a well-known “adsorbate evolution mechanism” (AEM), the metal sites with electron-rich structure are more easily oxidized, thus possessing higher reactivity for OER catalysis. Zhou et al. [128] reported that the doping of Mn cations with a weaker electronegativity than Ni and Fe led to activation of basal plane in NiFe-LDHs. Compared to pristine NiFe-LDHs, Mn^{2+} -doped NiFe-LDHs showed increased electron densities on Ni and Fe sites in the basal plane (initial: Ni^{2+} (8.92), Fe^{3+} (6.72); after doping: Ni^{2+} (8.96), Fe^{3+} (6.83)), as revealed by the DFT+U calculation, cf. Figure 5. Such surface electronic structure modification of Ni and Fe sites encountered in Mn^{2+} -doped NiFe-LDHs led to an overpotential of 230 mV at 100 mA cm^{-2} and a Tafel slope of 68 mV dec^{-1} in 1 M KOH solution. Such data were much lower than those of pristine NiFe-LDHs. Apart from Mn cation with an oxidation state of +2, the Mn^{4+} was also chosen to dope the laminate of NiFe-LDHs to improve the intrinsic electric conductivity, which displayed a narrower bandgap than that of NiFe-LDHs [129]. Moreover, Cai et al. [130] modified the local atomic structure of NiFe-LDHs by partially replacing Ni^{2+} with Fe^{2+} , forming Fe-O-Fe motifs in $\text{Ni}^{2+}\text{Fe}^{2+}\text{Fe}^{3+}$ -LDHs system. The in situ spectroscopic characterization results combined with DFT study demonstrated that the Fe-O-Fe sites could stabilize the high-valent Fe sites (i.e., $\text{Fe}^{(3+\delta)+}$, where $\delta > 0$), decreasing the energy barrier of the deprotonation step and resulting in an ultralow overpotential of 195 mV at 10 mA cm^{-2} for OER.

Additionally, the Co-doped NiFe-LDHs also exhibited an enhanced OER activity relative to pristine NiFe-LDHs. Strongin et al. [131] found that the doping amount of Co cations into NiFe-LDHs was strongly associated with their corresponding OER performance. The $\text{Ni}_{15}\text{Fe}_5\text{Co}_{2.5}$ -LDHs with cobalt substitution of ~12% showed an improvement in catalysis while a higher degree of substitution resulted in a slight decrease in OER activity. Such phenomenon was attributed to the modified energetics of OER reaction intermediates (O^* , *OH , and *OOH), which led to the improvement in OER catalysis. In another case, Co^{2+} and Co^{3+} were doped into NiFe-LDHs to substitute Ni^{2+} and Fe^{3+} , forming Co^{2+} -doped NiFe-LDHs and Co^{3+} -doped NiFe-LDHs, respectively [132]. The authors considered that Fe^{3+} in Co^{2+} -doped NiFe-LDHs and Co^{3+} in Co^{3+} -doped NiFe-LDHs were responsible for the high OER activity. In particular, the DFT+U simulation found that Co^{3+} with an optimal electronic structure could easily accept electrons from H_2O molecules, and thus accelerated the deprotonation step ($\text{*OH} \rightarrow \text{*O}$). The Co^{3+} -doped NiFe-LDHs and Co^{2+} -doped NiFe-LDHs exhibited onset overpotentials of 249 mV and 264 mV, respectively, lower than those of pristine NiFe-LDHs (282 mV). The results evidenced that the modification of electronic

structure of the active sites by doping extra metal cations (Co^{2+} or Co^{3+}) could successfully overcome the disadvantage of insufficient active sites of pristine NiFe-LDHs.

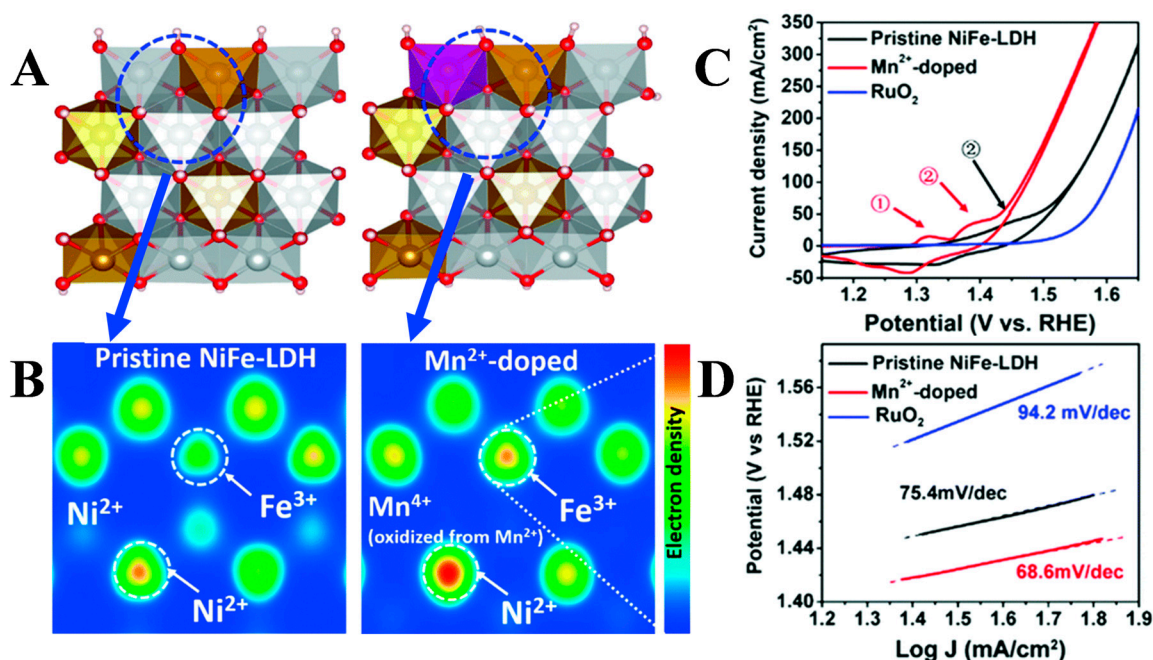


Figure 5. (A) Schematic structure of pristine NiFe-LDH and Mn^{2+} -doped NiFe-LDH. (B) Electronic structure of Ni and Fe sites in pristine NiFe-LDH and Mn^{2+} -doped NiFe-LDH in (A), respectively. (C) CV curves at a scan rate of 1 mV s^{-1} ; (D) Tafel slopes of pristine NiFe-LDH, Mn^{2+} -doped NiFe-LDH and RuO_2 in 1 M KOH solution [128]. Copyright © The Royal Society of Chemistry 2018.

The vanadium (V) doping had also been recognized as an efficient strategy to improve the intrinsic OER activity of pristine NiFe-LDHs [133]. Li et al. [134] reported that V-doping could modify the electronic structure of Fe sites in NiFeV-LDHs, and the strong electronic interaction in NiFeV-LDHs resulted in an unprecedented OER activity, which only required an overpotential of 195 mV to achieve a current density of 20 mA cm^{-2} and a Tafel slope of 42 mV dec^{-1} (Figure 6A–D). Due to the different electronegativity between Fe and V, a charge compensation in NiFeV-LDHs was generated, leading to the oxidation of V^{3+} to V^{4+} and V^{5+} , accompanied by the reduction of Fe^{3+} . The DFT calculation results showed that V-doping into NiFe-LDHs decreased the free energy difference from $^*\text{OH}$ to $^*\text{O}$, and thus resulted in a fast water oxidation reaction rate at the low overpotential. The total density of states (TDOS) spectrum further confirmed that V-doping could change the conduction band state of LDHs, and narrow its bandgap to provide a more conductive electronic structure for OER catalysis, which was in agreement with the results of the decreased resistivity from $(2.4 \pm 0.3) \times 10^3 \Omega \text{ sq}^{-1}$ to $(1.3 \pm 0.2) \times 10^3 \Omega \text{ sq}^{-1}$ in (NiFe-LDHs), and (NiFeV-LDHs), respectively. On the other hand, a study carried by Jiang et al. [111] suggested that the V-doping with distorted geometric and disturbed electronic structures made a crucial contribution to high activity of the Ni/Fe/V trimetallic catalysts. The XANES and XPS results revealed that the partial electron transfer from Ni^{2+} to Fe^{3+} in NiFe-LDHs or V^{4+} and V^{5+} in NiV-LDHs, or Fe^{3+} in NiFeV-LDH took place from Ni^{2+} through the oxygen bridges (O^{2-}) between metal cations via π -donation. After that, the electron-rich t_{2g} d -orbital of Fe^{3+} transferred electrons to the strongly electron-deficient t_{2g} d -orbitals of V^{4+} and V^{5+} through the bridging O^{2-} ions, which led to a better π -symmetry electron delocalization among Ni, Fe, and V cations in the host matrix, as shown in Figure 6E. The optimized $\text{Ni}_3\text{Fe}_{0.5}\text{V}_{0.5}$ catalyst exhibited an outstanding OER performance with a low overpotential of 200 mV at 10 mA cm^{-2} .

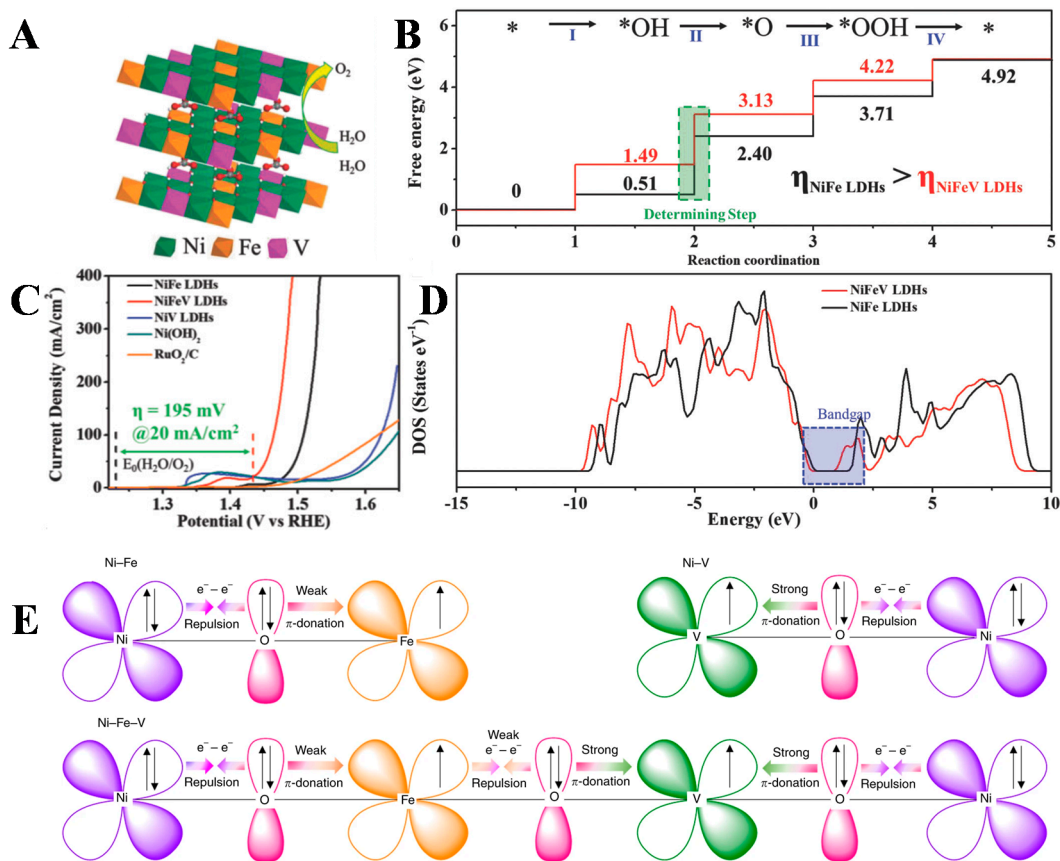


Figure 6. (A) The schematic diagram of NiFeV-LDHs structure. (B) Polarization curves of the non-noble metal catalysts (NiFeV-LDHs, NiFe-LDHs, Ni(OH)₂, and NiV-LDHs) and the commercial RuO₂/C catalyst (C) Gibbs free energy diagram for the four steps of OER on NiFe LDHs (black line) and NiFeV LDHs (red line). (D) Total density of states (TDOS) curves of NiFeV LDHs and NiFe LDHs [134]. Copyright © 2018 WILEY-VCH Verlag GmbH & Co. KGaA, Weinheim. (E) Schematic representations of the electronic coupling among Ni, Fe, and V in Ni₃Fe, Ni₃V, and Ni₃Fe_{0.5}V_{0.5} [111]. Copyright © 2018 Nature Publishing Group.

Moreover, the dopants could serve as new active sites in the resultant metal-doped LDHs, thus improving the reactivity of the active sites. Wang's group [135] reported a highly active ORR electrocatalyst: Cr-doped CoFe-LDHs, which only demanded an overpotential of 238 mV to obtain a current density of 10 mA cm⁻² in 1 M KOH electrolyte. The experimental and theoretical simulation studies demonstrated that the engineered electronic modulation aroused from the Cr-doping effect in Cr-doped CoFe-LDHs, and the Cr dopants as new active sites donated more electrons to the reactants thanks to the smaller electronegativity of Cr in comparison with Fe and Co. Consequently, the larger charge transfers of Cr–O resulted in the larger binding energy relative to Co–O bonds, which assisted to break the scaling relation between ΔG^*_{OOH} and ΔG^*_{OH} and boosted the OER activity. A similar phenomenon was also observed for Cr³⁺-doped CoFe-LDHs with partial-oxidized Cr⁶⁺ cations [136]. By virtue of the strong electron-withdrawing ability for Cr⁶⁺ cations, the electronic structure of active sites was modified, forming new Co-active sites with high oxidation state for H₂O absorption in the OER process. Enhanced OER activity was achieved by partially oxidized Cr⁶⁺ in Cr³⁺-doped CoFe-LDHs with an overpotential of 202 mV at 10 mA cm⁻².

It is noteworthy that the doping of non-metallic atoms (i.e., Se, S, B, F, and P) is another efficient protocol to modify the electronic structure to boost the intrinsic conductivity of LDHs materials. For example, an active S-doped NiFe-LDH electrocatalyst was synthesized through a one-step hydrothermal process [137]. Herein, S introduced in trace amount in Ni_{4/5}Fe_{1/5}-LDHs played a vital role in boosting its catalytic activity towards OER. When

the S doping amount was ~0.43 at%, the sample Ni_{4/5}Fe_{1/5}-LDHs-S-2 demonstrated the best OER activity in alkaline media, featuring an overpotential of 257 mV at 10 mA cm⁻² lower than that of Ni_{4/5}Fe_{1/5}-LDHs without S doping (325 mV). Such enhanced OER activity of S-doped NiFe-LDHs was the result of the synergistic effect between S and the Fe sites to reduce the energy barriers for the formation of the OER intermediates on Fe sites, and thus enhancing the OER activity. Inspired by amorphous boron-based catalysts, with a mass of percolation pathways and a fast-diffusion rate, amorphous boron-modified LDHs (B-Co₂Fe-LDHs) material decorated by numerous nanosheet-nanoflakes, was prepared [78]. The defective interfaces in the crystalline-amorphous phase boundaries allowed for enhanced electronic kinetics with an overpotential of 309 mV at 100 mA cm⁻² and high corrosion resistance of more than 100 h both in fresh and saltwater. This work provides a simple and scalable strategy to develop efficient and stable LDHs materials for highly selective seawater oxidation. Zhang et al. [138] fabricated a surface reconstructed NiFe-OH-F-SR catalyst derived from fluoride-incorporated NiFe hydroxide nanosheets (NiFe-OH-F) as an excellent OER catalyst. The OER activity of the NiFe-OH-F-SR electrode was increased by ~58 folds compared with the original NiFe-OH-F. This phenomenon could be attributed to: (i) the reconstructed amorphous surface layer, with defect-rich and the high defect concentration, played an important role in improving the conductivity of the NiFe-OH-F-SR; (ii) the increased surface area, desirable nanostructure, as well as enhanced charge-transfer ability helped to improve the electrocatalytic activity of NiFe-OH-F-SR; and (iii) the hierarchical framework with three levels of porosity of NiFe-OH-F-SR, was beneficial for exposing catalytic active sites and making them completely in contact with the electrolyte, promoting the electrochemical reaction.

Moreover, the intrinsic activity of LDHs can be fine-tuned by adjusting the molar ratio of the metal components. For example, Liu et al. [139] found that the molar ratio of Co/Fe greatly affected the OER electrocatalytic performance of CoFe-LDHs by controlling the ratio of CoO₆ octahedrons and CoO₄ tetrahedrons. With increasing Fe content, there were fewer CoO₄ tetrahedra when the ratio reached a certain degree (Co/Fe = 5:1), resulting in higher OER performance than the other with a Co/Fe ratio of 3:1. The appropriate Fe content could activate the inactive octahedral coordinated Co²⁺, giving rise to an enhanced reactivity. When the Fe content was further increased, there was a loss of catalytic activity of tetrahedrally coordinated Co²⁺. Moreover, a series of CoMo-LDHs with different Co/Mo weight ratios (1:4, 2:3, 3:2, and 4:1) were synthesized by Lee's group [140]. Among these catalysts, the Co₃Mo₂-LDHs showed the highest OER activity due to the synergic effect between Co and Mo, and compositional merits with adequate number of active Co and Mo species.

3.2. Intercalation

The intercalation of LDHs, with a layer-by-layer structure, is a process of inserting a foreign species between the edge-shared metal hydroxide layers of the LDHs. The host-guest interaction in LDHs can be modulated by controlling the properties of interlayer guests, e.g., the radii, redox activity, acid and/or base. In many reported works, it has been proposed that the intercalation can lead to remarkably improved OER performance for LDHs materials.

An early study revealed that the divalent anions possessed higher ion selectivity than monovalent ones, and the ion-exchange equilibrium constants followed the sequence: CO₃²⁻ > SO₄²⁻ > OH⁻ > F⁻ > Cl⁻ > I⁻ [141]. Later, Müller's group [142] further studied the effect of the anions (A^{m-}) with different valence states on water oxidation activity for NiFe-LDHs. Based on the Gaussian fits of the (003) peaks results, the calculated basal spacings of NiFe-A^{m-}-LDHs materials with different intercalated anions, were depicted in Figure 7A. It was worth noting that this analysis was limited to the spherical halogen anions. It obviously showed that there was a linear correlation of the calculated basal spacings with anionic radii. However, the measured overpotentials were not dependent on the basal spacings. On the other hand, they discovered that the water oxidation

activity was strongly correlated with the pK_a of the conjugate acid of the interlayer anions, e.g., the larger pK_a value, the higher OER activity of the intercalated LDHs (Figure 7B). This result suggested that the anions' Brønsted or Lewis basicity played a role in the water oxidation mechanism of transition metals-based LDHs. In the same context, Sun's group correlated the intercalated phosphorus oxo-anions (e.g., phosphate, phosphite, and hypophosphite) and the OER performance of NiFe-LDHs [143]. They found that the intercalation of phosphorus oxo-anions dramatically enhanced the OER activity and durability over the carbonate-intercalated NiFe-LDHs in an alkaline solution. Specifically, the optimal performance (e.g., a low onset potential of 215 mV and a small Tafel slope of 37.7 mV dec^{-1}) was achieved by the hypophosphite-intercalated NiFe-LDHs, which was attributed to its stronger donor-electron ability than phosphate and phosphite. Later, Zhou and Sun [144] proposed a universal relationship between sixteen anions-intercalated NiFe-LDHs and their OER activity from a different viewpoint. The authors deemed that the OER performance was not completely relevant to the pK_a of the conjugate acid of the interlayer anions, but a linear relationship between the redox potential of the intercalated anions and the corresponding OER activity, as shown in Figure 7C. For example, the intercalated hypophosphite anions with a high reducing ability led to the formation of electron-rich metal sites, which could be easily oxidized to higher-valence states then acted as active sites in the OER process, providing a higher OER activity. DFT+U calculations and XPS analysis demonstrated the introduced anions modified the electronic structure of the exposed metal atoms, increasing the electron density of the laminate metal sites and stabilizing the high-valence states, which was beneficial to lower the activation energy and improve the OER performance.

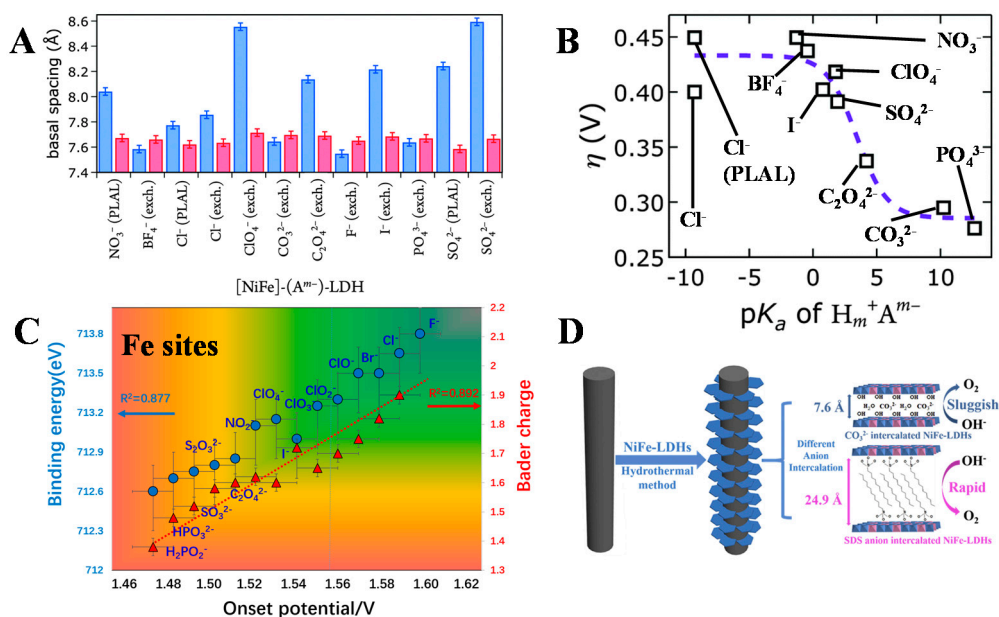


Figure 7. (A) Basal spacings of NiFe-LDHs nanosheets with different interlayer anions as synthesized (blue) and after suspension in 1 M KOH in ambient air (red). (B) Overpotentials η of NiFe-LDHs materials with different interlayer anions A^{m-} derived from constant current electrolysis at 1 mA cm^{-2} in virtually carbonate-free electrolyte as a function of anion basicity [142]. Copyright © The Royal Society of Chemistry 2016. (C) Relationship between onset potentials with the standard redox potentials of the examined anions [144]. Copyright © Tsinghua University Press and Springer-Verlag GmbH Germany 2017. (D) Schematic illustration of the fabrication process of $\text{Ni}_2\text{Fe-CO}_3^{2-}$ -LDH/CFP and $\text{Ni}_2\text{Fe-SDS}^{2-}$ -LDH/CFP [60]. Copyright © 2017 Elsevier Ltd.

The intercalated anions, with larger basal spacing, benefit the OER performance of the LDHs by providing more space for mass diffusion during the oxygen evolution. Xu and Hao [145] fabricated two intercalated NiFe-NO₃⁻-LDHs and NiFe-CO₃²⁻-LDHs catalysts

and compared their OER activity differences. The NiFe-NO₃⁻-LDHs with an interlayer spacing of 7.69 Å displayed a higher OER activity than NiFe-CO₃²⁻-LDHs (interlayer spacing of 8.04 Å), as a result of more exposed active sites and a low charge transferring resistance. Zhong et al. [60] intercalated dodecyl sulfonate (DS⁻) into the interlayer spaces of NiFe-LDHs through a one-step hydrothermal method, which increased the basal spacing (Figure 7D) from 7.6 Å to 24.9 Å. As a result, the overpotential for OER to reach the current density of 10 mA cm⁻² reduced from 333 mV to 289 mV. Li et al. [146] developed an in situ intercalation method to prepare formamide intercalated NiFe-LDHs electrodes, and the corresponding interlayer spacing increased from 7.8 Å to 9.5 Å. More importantly, compared with ex situ intercalation/exfoliation approach, the in situ intercalation method largely maintained the good interfacial connection and long-term stability of LDHs materials, which provided an overpotential of 203 mV at 10 mA cm⁻² and a stability of up to 16 h. Komarneni et al. [147] intercalated several dicarboxylic acids of different alkyl chain lengths (suberic acid, adipic acid and succinic acid) into the interlayer spaces of NiFe-LDHs and studied the effect of basal spacing on the OER activity. It was discovered that suberic acid, intercalated in NiFe-LDH, exhibited a remarkable activity for OER in a pH-near-neutral K-B_i electrolyte (pH = 9.2), which was mainly ascribed to the “structural instability” induced “in situ” anion exchange” process in which borate anions entered the interlayer and activated inner Ni sites. This work further proved that the pillaring of NiFe-LDHs with large organic anions was a promising method to create LDH-type high-performance catalysts for the OER in a pH-near-neutral K-B_i electrolyte.

The intercalation of homogeneous species (i.e., inorganic anions, organic acid/base, and organic complexes) favors improving the electrocatalytic performance for LDHs in three different aspects: (i) the enlarged basal spacing with more exposed inner active sites can facilitate the electron/charge transfer and the mass diffusion to bring about a more favorable OER kinetics; (ii) the intercalation could induce structural changes, such as lattice expansion or phase change, providing novel physicochemical properties; and (iii) due to the different redox ability between the metal sites and intercalated anions, the intercalation significantly modulates the electronic structure of metal sites in the laminate, endowing them with optimal binding of reaction intermediates and enhanced chemical reactivity.

3.3. Vacancy Engineering

Recently, the vacancy engineering has emerged as an interesting strategy to improve the OER electrocatalytic performance of LDHs materials. Many studies manifested that the oxygen vacancies could decrease the absorption energies of OER intermediates, and the metal vacancies would lead to the formation of unsaturated-coordination metal centers which can serve as active sites and subsequently improve OER activity. What is more, the vacancy can also act as new active sites, narrowing the bandgap to increase the conductivity [148]. It is noteworthy that the different types of the vacancy (oxygen vacancies and metal vacancies) make different contribution to the OER performance of LDHs due to the different working mechanisms and functions. To be specific, the creation of metal vacancies leads to “positive holes”, to facilitate the adsorption of *O intermediates on the surface, which renders the conversion of *O to *OH energetically quite favorable and results in a small overpotential [149]. The oxygen vacancies can induce the bonding interaction between the exposed oxygen-coordination-deficient metal atoms/centers and *OH intermediates to promote the uptake and conversion of *OH [150].

There are various post-synthesis methodologies for introducing vacancies, such as thermal treatment [151], acidic/alkaline etching [152], ball mill [153], and laser ablation [154]. Especially, the aqueous chemical reduction by strong reducing agents (NaBH₄/N₂H₄) [155] or high-temperature (e.g., >600 °C) annealing under H₂ atmosphere [148] can selectively create the oxygen vacancies. Xiong et al. [155] introduced the oxygen vacancies into NiFe-LDH nanosheets by a simple immersion in NaBH₄ solution at room temperature (Figure 8A). The role of oxygen vacancies in NiFe-LDHs during the OER process was investigated by DFT+U calculations. Taking the bridge sites between Ni and Fe (Ni-O-Fe)

as the active sites, the calculation results elucidated that the potential determining step (PDS) of pristine NiFe-LDHs was the deprotonation step with a high overpotential of 0.86 V, and after introducing oxygen vacancies, the potential determining step (PDS) of defective NiFe-LDHs tuned to be the *OOH formation step with a lower overpotential (0.65 V), showing a higher intrinsic activity. In another case, Zhou et al. [151] synthesized oxygen vacancies-rich NiFe-LDH nanosheets through a fast (30 s) and facile (operated at room temperature) flame-engraving method. In Figure 8B, the inner core of a burner flame was typically deficient in oxygen, yielding a reducing and high-temperature environment to rapidly create oxygen vacancies in NiFe-LDHs structure. After flame treatment, the thickness of NiFe-LDH nanosheets decreased from 4.5 to 3.5 nm, while many well-defined hexagonal cavities with (110) edges appeared. Abundant oxygen vacancies, lower coordination numbers, and electron-rich structures of Ni and Fe sites emerged in the flame-engraved NiFe-LDHs array electrode, leading to its onset potential as low as 1.40 V.

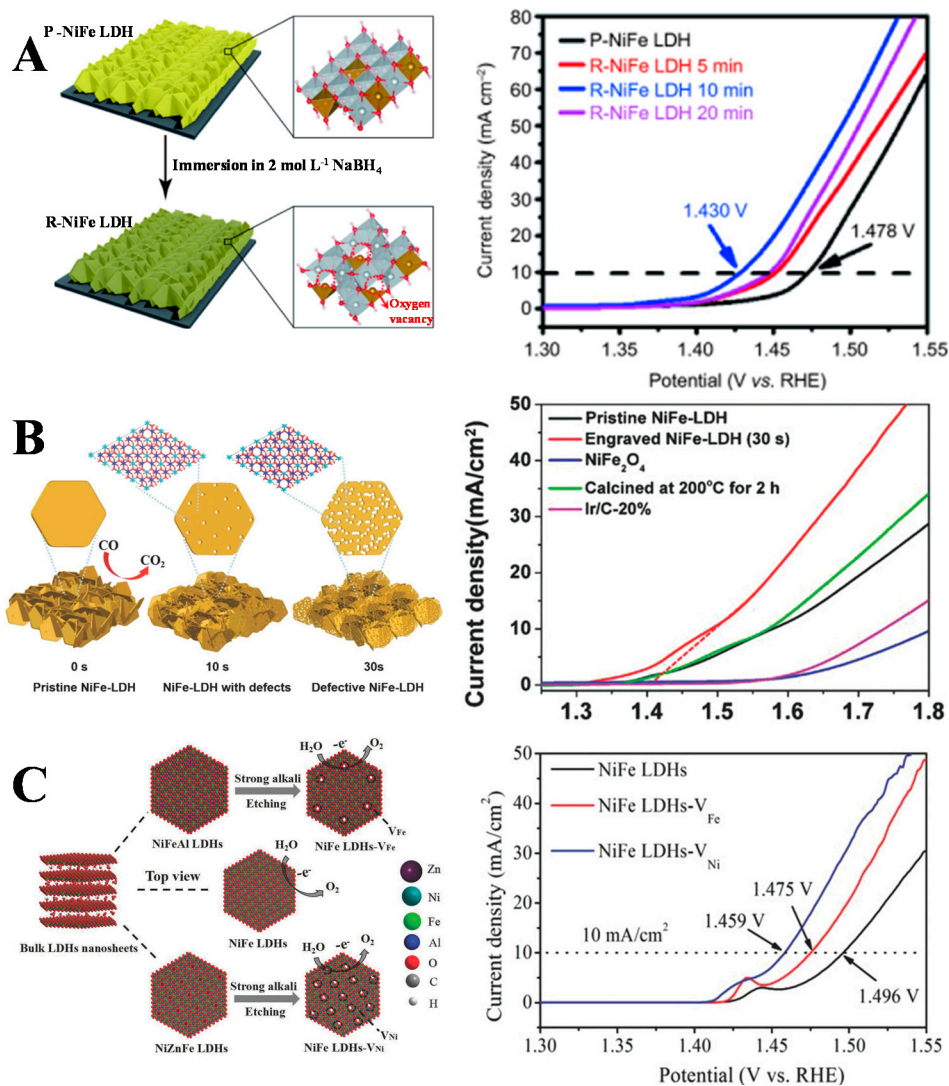


Figure 8. (A) Schematic illustration of introducing oxygen vacancy defects to NiFe-LDHs nanoarray electrode and the corresponding OER performance [155]. Copyright © Science China Press and Springer-Verlag GmbH Germany 2018. (B) Schematic illustration of defective NiFe-LDH with oxygen vacancies prepared by fast reducing flame treatment for different periods of time and the corresponding OER performance [151]. Copyright © 2018 WILEY-VCH Verlag GmbH & Co. KGaA, Weinheim. (C) The synthesis of NiFe LDHs-V_{Fe} and NiFe LDHs-V_{Ni} by strong alkali etching LDHs and the corresponding OER performance [49]. Copyright © 2018 WILEY-VCH Verlag GmbH & Co. KGaA, Weinheim.

In addition to oxygen vacancies, introduction of metal vacancies via etching could selectively create M^{II} or M^{III} metal vacancies in LDH nanosheets. Xie et al. [156] reported a novel method of ionic reductive complexation extraction (IRCE) to etch the target Cu(II) ions and create atomically dispersed cation vacancies in SAV-NiCu_x-LDHs. In a typical procedure, based on the different equilibrium constant (K) of transition metal ions, SCN[−] was used as the extractant because of the large log K of Cu(I)-SCN (12.11), which was more than six-folds higher than that of Cu(II)-SCN (1.9) and Ni(II)-SCN (1.18). To achieve selective extraction of Cu from NiCu-LDHs, Na₂SO₃ was added to in situ reduce the Cu(II) to Cu(I). The overpotential at 100 mA cm^{−2} and Tafel slope of SAV-NiCu_x-LDHs were evaluated to be as low as 355 mV and 45 mV dec^{−1}. This work provides a promising direction for engineering atomically dispersed vacancies and alleviating the mechanical collapse of LDHs, greatly guaranteeing the superior OER activity of the electrocatalysts. Besides, the alkaline etching treatment in 1 M KOH solution, was also employed to manufacture Fe³⁺ (Ni²⁺) vacancies in NiFeAl-LDHs (NiZnFe-LDHs) to prepare NiFe-LDHs-V_{Fe} (NiFe-LDHs-V_{Ni}) electrocatalysts, respectively (Figure 8C) [49]. The NiFe-LDHs-V_{Fe} and NiFe-LDH-V_{Ni} nanosheets exhibited faster OER kinetics and smaller charge transfer resistance compared with NiFe-LDHs, which could be ascribed to the following reasons: (i) the edge and corner sites with numerous coordinated unsaturated sites helped to enhance the catalytic activity of defective LDHs; (ii) the redistributed electronic structure of reactive sites surrounding Fe or Ni vacancies led to form more Ni³⁺ with an optimal orbital distribution of $t_{2g}^6 e_g^1$ (the e_g orbital occupancy of surface metal ion is 1, being regarded as the optimal electronic configuration for OER) [157], facilitating the adsorption of OER intermediates; and (iii) the defective states that appeared in the conduction and valence bands could hybridize with $2p$ states of *O resulted in a strong *O adsorption, which essentially enhanced the OER activity.

Both of the oxygen and cation vacancies engineering in one NiFe-LDHs system was reported by Zhang et al. [158], through a fast, one-step synthetic strategy in the presence of formamide. The defective-LDHs showed excellent OER performance with a low overpotential of 230 mV at 10 mA cm^{−2}, and a Tafel slope of 47 mV dec^{−1}. The synergistic effect between the oxygen vacancies and metal vacancies increased the electro-positivity of the LDH nanosheets, and thus facilitated the adsorption of H₂O and increased the *OH bonding energy. In the same context, Zhou et al. [159] prepared multiple vacancy-rich (Co, Fe, and O vacancies) CoFe-LDHs nanosheets, via an HNO₃-etched reaction (labeled E-CoFe-LDHs). Since the solubility of Co(OH)₂ was greater than Fe(OH)₃, the former was more active to react with HNO₃, leaving more Co vacancies in LDHs. Benefiting from modified electronic structure and more active sites, the E-CoFe-LDHs showed better OER performance than the pristine LDHs.

In summary, vacancies can offer the following advantages to electrocatalysts: (i) it can build atomic defects and influence the chemical environment on the catalyst surface; (ii) it can form a porous structure, increase specific surface area, and expose more edge sites and active sites to expend the electrochemical area; and (iii) it can also reduce the electron transfer resistance and speed up the mass transfer to accelerate the reaction kinetics. Consequently, etching layered double hydroxides is an alternative strategy to get highly efficient catalysts.

3.4. Ultrathin Nanosheets

The exposure and accessibility of active sites and the surface adsorption capability of the reactants are strongly associated with the morphology of the catalysts, which plays a crucial role in the electrocatalytic performance. Usually, the pristine LDHs with several self-stacking layers display inferior electrocatalytic activity. In contrast, ultrathin LDHs nanosheets with single-or few-atoms thickness and large lateral size show excellent electrocatalytic performance due to their ultrahigh specific surface area and highly intrinsic activity of active sites [160]. The layer modification/engineering methods generally include the “top-down” exfoliation and the “bottom-up” direct synthesis. The former is in virtue of

strongly physical shear force or chemical intercalation to break interlayers bonding forces, and then exfoliate the bulk into single or few-layered nanosheets, while the latter tends to directly prepare ultrathin 2D LDHs nanosheets based on the chemical reaction.

The chemical exfoliation is recognized as a “top-down” route, through which ultrathin LDHs nanosheets were prepared. The chemical exfoliation usually involves multi-chemical processes, including anion-exchange, osmotic swelling, and exfoliation [161]. Typically, the anion-exchange initializes the process by enlarging the interlayer spacing and weakening the interaction between host layers, which is conducive to the following osmotic swelling. The swelling is triggered by intercalating organo-ammonium anions into the interlayer region, and the corresponding degree can be adjusted by the balance of osmotic pressure between the interlayer region and the solvent. The pristine LDHs can be exfoliated into unilamellar nanosheets with a molecular-level thickness of about 1 nm versus 2D lateral size in submicrometer or micrometer scale.

The liquid exfoliation of LDHs nanosheets in the presence of various anionic surfactants has motivated a strong interest since Adachi-Pagano et al. [162] reported, in 2000, the successful delamination of layered double hydroxide structure $[\text{Zn}_2\text{Al}(\text{OH})_6][\text{C}_{12}\text{H}_{25}\text{SO}_4 \cdot n\text{H}_2\text{O}]$ in butanol solution. The authors pointed out that the van der Waals interlayer interactions were introduced by the intercalation of dodecyl sulfate anions in $\text{Zn}_2\text{Al}(\text{OH})_6\text{Cl} \cdot 2\text{H}_2\text{O}$, which weakened the stacking of the layers and favored interactions with butanol solvent. Later in 2014, inspired by the topochemical transformation, Song and Hu [160] conducted a pioneering study to prepare NiFe-LDHs, NiCo-LDHs, and CoCo-LDHs with single-layer nanosheets via an anion-exchange process and a formamide-exfoliation process. After anion exchange, the increased inter-layer distance allowed the delamination of the bulk LDHs to monolayer nanosheets in the purged formamide. In Figure 9A, the exfoliated LDHs nanosheets showed remarkably enhanced OER activity with a decrease (40–54 mV) of the overpotential at the current density of 10 mA cm^{-2} compared with its original bulk one. They suggested that the higher intrinsic activity of exfoliated nanosheets was mainly due to the increased active site density, rather than the higher electrochemically active surface area (ECSA). Additionally, the edges in the exfoliated nanosheets, with open coordination sites, could serve as active sites for water oxidation. Zhang’s group [163] synthesized ultrathin and ultrafine monolayer ZnCo-LDHs with abundant oxygen vacancies and unsaturated coordination edge-sites through a simple ultrasonic exfoliation procedure in formamide. On the one hand, the ultrathin and ultrafine nanostructure provided numerous accessible and coordinately unsaturated active sites for H_2O adsorption. On the other hand, the ultrafine monolayer nanosheets offered short diffusion paths for charge transfer to the current collector. As a result, the monolayer ZnCo-LDHs exhibited an enhanced OER activity with an overpotential of 340 mV at 5 mA cm^{-1} , which was smaller than that of the bulk counterpart (530 mV) in 1 M KOH electrolyte.

Nevertheless, the liquid-phase exfoliation is typically time-consuming and expensive, and the exfoliating solvent molecules, e.g., formamide and surfactants, are easily adsorbed on the exfoliated nanosheets, thus blocking the exposed active sites and reducing the catalytic activity. Recently, Yong et al. [164] reported a novel Ostwald ripening driven exfoliation (ORDE) of NiFe-LDHs on Cu mesh without the assistance of any exfoliating reagent or surfactant, which efficiently realized the in situ exfoliation of LDHs bulk into stable ultrathin nanosheets with significantly improved OER performance (Figure 9C). In the thermodynamic process, the tiny stacked layers on each bulk LDH surface tended to dissolve in solution and redeposited on the edge sites of relatively large layers to reach a more stable equilibrium state with lower overall energy, resulting in the larger lateral dimension (*X* and *Y* directions) and thinner thickness of each bulk bundle, and creating abundant active edge-sites at the same time. This ultrathin NiFe-LDHs/Cu with increased surface area exhibited a competitive OER activity with an overpotential of 292 mV at 10 mA cm^{-2} , and a superior stability for 60 h at the fixed current density. The plasma etching is also a highly efficient strategy for exfoliation of LDHs into stable and clean ultrathin nanosheets. Compared with liquid-phase exfoliation, plasma-induced exfoliation process only involved solid powders and plasma, which avoids the adsorption of solvent

molecules and prevents the re-stacking of LDHs nanosheets. For example, Wang et al. [165] exfoliated bulk CoFe-LDHs into ultrathin LDH nanosheets by Ar plasma etching, which also caused the formation of multiple vacancies (V_{Co} , V_{Fe} , and V_O), cf. Figure 9B. The XRD spectra and atomic force microscopy (AFM) images confirmed the successful exfoliation of the LDHs into monolayer nanosheets because of the disappearance of the (003) and (006) diffraction peaks and the decreased layer thickness from 20.6 nm to 0.6 nm. The multiple vacancies effectively modulated the surface electronic structure and decreased the coordination numbers of catalytic sites, which in turn improved the intrinsic activity of ultrathin LDH nanosheets. Upon exfoliation, the ultrathin CoFe-LDHs-Ar catalyst only acquired a small overpotential of 266 mV to reach the current density of 10 mA cm^{-2} in 1 M KOH, whereas it was 321 mV for bulk CoFe-LDHs. With the same strategy, Liu et al. [166] applied the CHF_3 -plasma etching technique to exfoliate the $\text{Co}_3\text{Fe-LDH}$ s and obtain F-doped $\text{Co}_3\text{Fe-LDH}$ ultrathin nanosheets. Interestingly, during the CHF_3 -plasma treatment process, F^- ions selectively filled oxygen vacancies, and tuning the electronic structure with a high electronegativity. The previous literature reported that the F-doping can enhance the electronic conductivity of electrocatalysts, and then facilitate the electron transfer and the formation of active sites to decrease the Gibbs reaction energy barrier [167]. As expected, the OER activity of CoFe-LDHs supported on Ni foam was optimized, which only needed a small overpotential of 276 mV to reach 10 mA cm^{-2} .

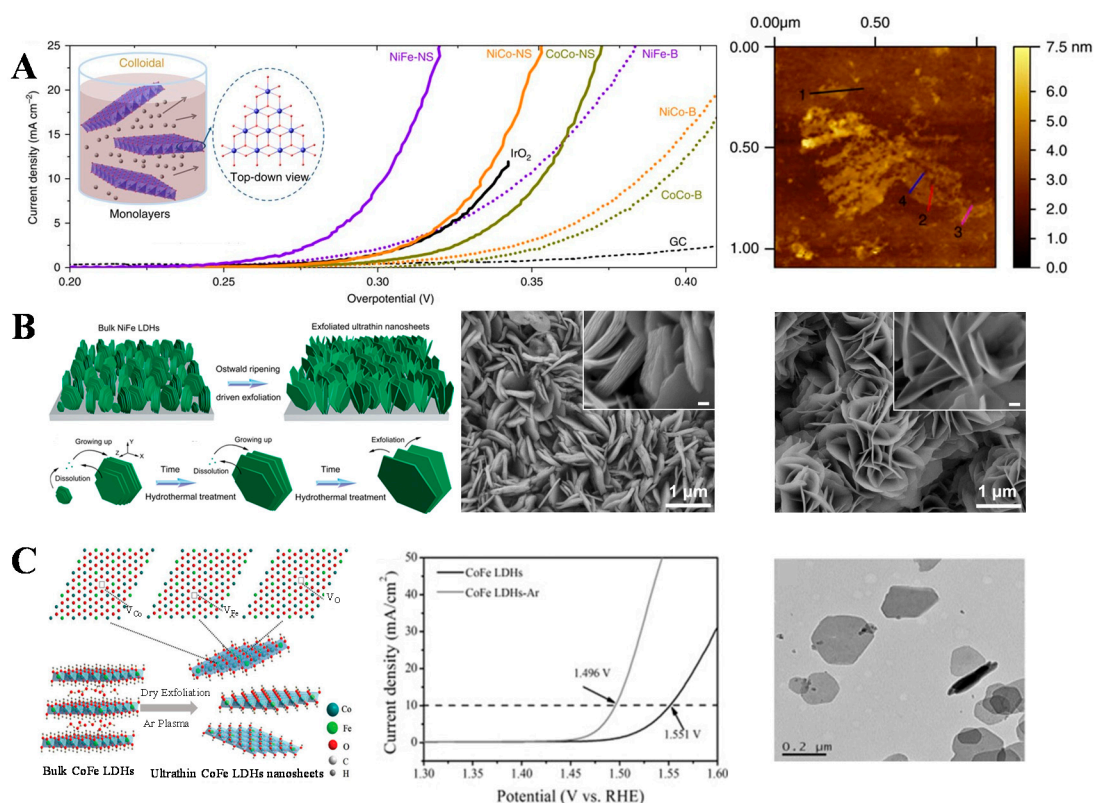


Figure 9. (A) Schematic representation of materials structures, the corresponding polarization curves at 1600 rpm in 1 M KOH and the AFM image of exfoliated single-layer nanosheets of NiCo LDH [160]. Copyright © 2014 Macmillan Publishers Limited. (B) Schematic illustration for pristine bulk NiFe-LDHs transformed to exfoliated ultrathin nanosheets via the ORDE process, and the SEM characterizations of the pristine bulk (left) and exfoliated NiFe LDHs (right) [164]. Copyright © 2018 American Chemical Society. (C) CoFe-LDH nanosheets by Ar plasma exfoliation, the corresponding OER performance at 1600 rpm in 1 M KOH and the TEM image of the ultrathin CoFe LDHs-Ar nanosheets [165]. Copyright © 2017 Wiley-VCH Verlag GmbH & Co. KGaA, Weinheim.

The “bottom-up” chemical methods including microemulsion method and layer growth inhibitors, can realize the direct synthesis of ultrathin 2D LDH nanostructures

by creating a “microreactor” environment or inhibiting the growth of the layers by a layer growth inhibitor (e.g., formamide, acetylacetone, and ethylene glycol) [168,169]. For example, Gao et al. [168] constructed a series of ultrathin atomic-thick LDH nanosheets through a facile and rapid precipitation method with both formamide and water as solvents (Figure 10A). The AFM image manifested that the individual nanosheet had an average thickness of ca. 1.3 nm and width of 40 nm. The height was very close to the single-unit-cell spacing in the (001) direction (~ 0.8 nm) for CO_3^{2-} /LDHs, confirming the successful synthesis of ultrathin single-unit-cell LDHs nanosheets. The overpotential at 10 mA cm^{-2} of the ultrathin LDH NSs was 72 mV lower than the bulk counterpart, which mainly originated from the increase in active site density and C_{dl} values in the ultrathin single-unit-cell-thick LDHs (Figure 10B). Very recently, Zhao et al. [170] synthesized sub-3 nm monolayer LDHs (LDH-UF), namely, the lateral size less than 3 nm, by means of the pulsed ultrasonication of monolayer LDHs nanosheet precursors in formamide, cf. Figure 10C. EXAFS studies and DFT calculations revealed that the sub-3 nm monolayer LDHs possessed a higher concentration of metal and oxygen vacancies compared with the monolayer NiFe-LDHs precursor or bulk NiFe-LDHs, which gave the former semi-metallic character. The high conductivity of LDH-UF, along with an abundance of exposed surface sites (especially sheet edges), all contributed to the ultrafine nanosheets displaying enhanced performance for electrocatalytic water oxidation relative to monolayer LDH nanosheets. (Figure 10D). Kuai and Du [171] developed an alcohol intercalation method to prepare ultrathin NiFe-LDHs with a $1/3$ unit-cell thickness. Operando synchrotron X-ray analysis indicated that the metallic ions in ultrathin Ni-Fe LDHs were fully oxidized into tetravalence states at low applied potentials and that the OER occurred on the tetravalent Ni and Fe ions following a decoupled proton/electron mechanism. Furthermore, it was found that a full oxidation of metal ions played a vital role in highly active NiFe LDHs and that it can be accomplished by engineering ultrathin nanostructures.

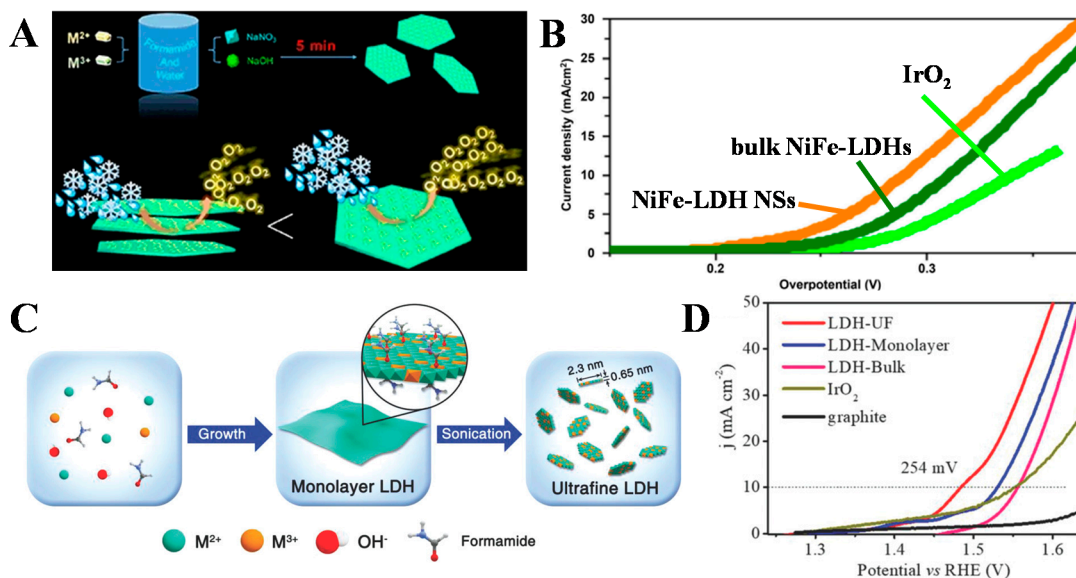


Figure 10. (A) Schematic illustration for the formation of ultrathin single-unit-cell-thick LDH NSs; (B) LSV curves for the ultrathin single-unit-cell NiFe-LDH NSs, bulk NiFe-LDHs, IrO_2 nanoparticles at 1600 rpm in 0.1 M KOH solution [168]. Copyright © Tsinghua University Press and Springer-Verlag GmbH Germany 2017. (C) Synthetic strategy used for the synthesis of ultrafine monolayer LDH nanosheets; (D) OER polarization curves for LDH-Bulk, LDH-Monolayer, LDH-UF, IrO_2 , and graphite, respectively at 1600 rpm in 1 M KOH solution [170]. Copyright © 2018 WILEY-VCH Verlag GmbH & Co. KGaA, Weinheim.

3.5. Nanostructuring

The controllable synthesis of the electrocatalysts with well-defined nanostructure, morphology, size, and crystallinity provides solid foundation for the development of LDHs. Among many nanostructures, the hierarchical porous structures received particular attention due to their better electrolyte permeability, shorten mass and electron transport paths. There are several common strategies to prepare the porous electrocatalysts as follows: (i) in situ growing on a porous substrate (carbon paper, carbon cloth, Ni foam, etc.); (ii) external-template methods: the hard templates including SiO₂, MgO, and Al₂O₃, which need to be removed using etching agents such as HF and NaOH; the soft templates usually used in the preparation of organic compounds are not eco-friendly; and (iii) self-template methods utilizing a porous precursor, e.g., metal organic frameworks (MOFs). For instance, Zhong et al. [172] fabricated a series of 3D flower-like NiFe-LDH hollow microspheres (3D NiFe-LDHs HMS) by adjusting the concentration of NH₄F and reaction time during the hydrothermal treatment. This fluoride-mediated self-transformation process or Ostwald ripening for the preparation of hollow microspheres, was beneficial for the exposure of more inner-active sites and improvement of the hydrophilicity, which can reduce the ion-transport resistance and thus enhance the OER dynamics. The optimized NiFe-LDH-0.4M HMS showed an excellent OER performance with $\eta = 290 \text{ mV}@10 \text{ mA cm}^{-2}$ and a Tafel slope of 51 mV dec^{-1} in 1 M KOH solution. A similar phenomenon was also observed for NiFe-LDHs hollow microspheres (HMS) with a shell thickness of 50 nm synthesized by [173] in situ grew NiFe-LDHs on the SiO₂ surface as a self-sacrificial template, which was subsequently etched, as displayed in Figure 11A. The NiFe-LDHs HMS showed highly efficient OER electrocatalytic activity with a preferable current density (71.69 mA cm^{-2} at $\eta = 300 \text{ mV}$) and a small onset overpotential (239 mV at 10 mA cm^{-2}), which outperformed the 20 wt.% commercial Ir/C catalyst. Moreover, it exhibited a low Tafel slope (53 mV dec^{-1}) as well as a desirable long-time stability. Such outstanding OER performance was ascribed to its high specific surface area, flourishing pore structure, and excellent hydrophilicity, which facilitated a full exposure of active sites and facile ion transport kinetics. Similarly, Lou's group prepared hierarchical NiFe-LDHs hollow nanoprisms via a facile self-templated strategy by using nickel tetragonal nanoprism precursors as the self-sacrificial template [174]. It was found that, the NiFe-LDHs hollow nanoprisms had a higher OER activity, larger double-layer capacitance (C_{dl}), and more stable than the NiFe-LDHs nanocluster, suggesting that the open and porous structure was responsible for the enhanced OER performance.

Metal organic frameworks (MOFs), a self-assembly porous material, links organic and inorganic moieties through covalent coordination linkages, possessing tunable structures and versatile functionalities that render catalytic materials with large surface areas and pore sizes. As an example, Xu et al. [175] prepared a uniform and hollow 3D NiFeCe-LDHs microcapsule electrocatalyst by a facile one-step solvothermal reaction with the help of Ce-doping. As shown in Figure 11B, in the early stage, the formed MIL-88A templates became more stable after coordinating with Ce³⁺ ions; as the reaction progressed, urea gradually released more OH⁻ ions, which prompted the dissolution of the inner core and the precipitation of Fe³⁺, Ni²⁺ and extra Ce³⁺ to construct a hierarchical shell with vertical and interconnected NiFeCe-LDHs nanosheets on the surface of MOF precursors. By precisely controlling the concentration of Ce³⁺ ion, well-defined hierarchical hollow NiFeCe-LDHs microcapsules with a high specific surface area of $286.33 \text{ m}^2 \text{ g}^{-1}$ were obtained. The NiFeCe-LDHs microcapsules displayed a superior OER performance with a low overpotential of 242 mV at 10 mA cm^{-2} and good stability over 24 h. Zhu et al. [176] prepared the hollow Rh-doped CoFe-LDHs derived from the zeolitic imidazolate framework-67 (ZIF-67) nanotriangles by an efficient simultaneous etching-doping sedimentation equilibrium (EDSE) strategy. During the EDSE process, urea dissolved in aqueous solution and converted to ammonium cyanate, and the latter rapidly hydrolyzed to produce NH₄⁺ and CO₃²⁻. Then, the ammonium decomposed and formed an alkaline environment when temperature rose above 60 °C. The outer ZIF-67 nano-triangles were gradually etched,

while the generated Co^{2+} coprecipitated with the metal cations and form more stable CoFe-LDHs nanosheets, along with the simultaneous doping of Ru. The double-layer capacitance results demonstrated that the hollow Rh-doped CoFe-LDHs catalyst exhibited higher active area and more active sites than solid LDHs, which originated from the typical hollow hierarchical structure.

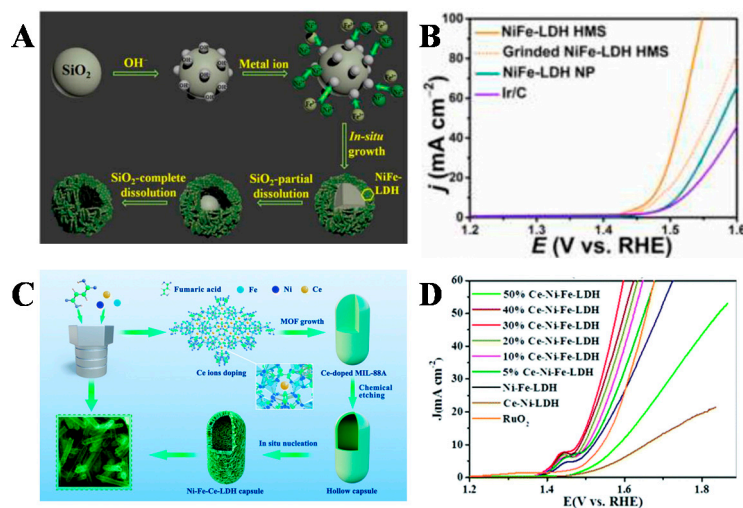


Figure 11. (A) Scheme of the Synthesis of NiFe-LDH HMS; (B) LSV curves of the catalysts at 1600 rpm in 1 M KOH [173]. Copyright © 2016 American Chemical Society. (C) Schematic illustration of the fabrication of hollow Ni-Fe-Ce-LDH microcapsules mediated by cerium doping in MIL-88A; (D) polarization curves of Ni-Fe-Ce-LDH with different Ce/Fe ratios at 1600 rpm in 1 M KOH solution [175]. Copyright © The Royal Society of Chemistry 2020.

3.6. Hybridization

The combination of two or more distinct properties into an integrated composite is a fascinating direction to develop multi-functional materials. Construction of LDH-based hybrids, especially one with a nanostructure, by interacting LDHs with other materials (e.g., carbon materials, metal/metal oxides, and 3D conductive substrate), has attracted extensive attention in the field of energy conversion and storage.

Coupling catalysts with conductive carbonaceous materials, e.g., graphene, carbon black, carbon nanotubes (CNTs), graphene quantum dots (GQDs) and carbon fiber papers (CFPs), is an extremely effective and reliable approach to promote their electrocatalytic performance by exposing more active sites and facilitating electron transfer [177]. Dai et al. [116] synthesized a novel hybrid of NiFe-LDHs/CNTs, in which mildly oxidized multiwalled CNTs served as the support; the electrostatic force between negatively charged functional groups on the CNTs can adsorb positively charged metal cation precursors. The NiFe-LDHs/CNTs exhibited outstanding OER performance due to more exposed active sites and the faster electron transfer. In a similar process, Guo et al. [178] hybridized Ni-based LDHs (NiM-LDHs, M=Fe, Co, Mn) and GQDs with the help of electrostatic-adsorption effect, and successfully fabricated a series of LDHs/GQDs hybrids, cf. Figure 12A. Due to the electron absorption/donation effects, electrons transferred from LDHs to GQDs, leading to the of new Ni^{3+} species, which were favorable for enhancing the electrocatalytic activity of OER (Figure 12B). Interestingly, they found, compared with NiMn-LDHs/GQDs, that NiFe-LDHs/GQDs and NiCo-LDH/GQDs with higher activity had a higher shift degree in Ni $2p_{3/2}$ binding energy, further attesting that Ni with high oxidation states has a positive effect on the OER activity. The NiFe-LDHs/GQDs with a strong interfacial electronic coupling exhibited a conspicuous catalytic performance with an overpotential of only 189 mV at 10 mA cm $^{-2}$. Further, Li et al. [179] reported an enhanced OER performance of superhydrophilic CoAl layered double hydroxides/graphdiyne (CoAl-LDHs/GDY) hybrid. They suggested that superhydrophilic GDY had strong interaction

with CoAl-LDHs catalysts and attracted H₂O molecules around the catalysts' sites, thus facilitating interfacial mass/electron transportation. By comparison, a lower overpotential of ~258 mV to reach 10 mA cm⁻² and higher turnover frequency (TOF) of ~0.60 s⁻¹ at $\eta = 300$ mV were observed on CoAl-LDHs/GDY than that of pure CoAl-LDHs.

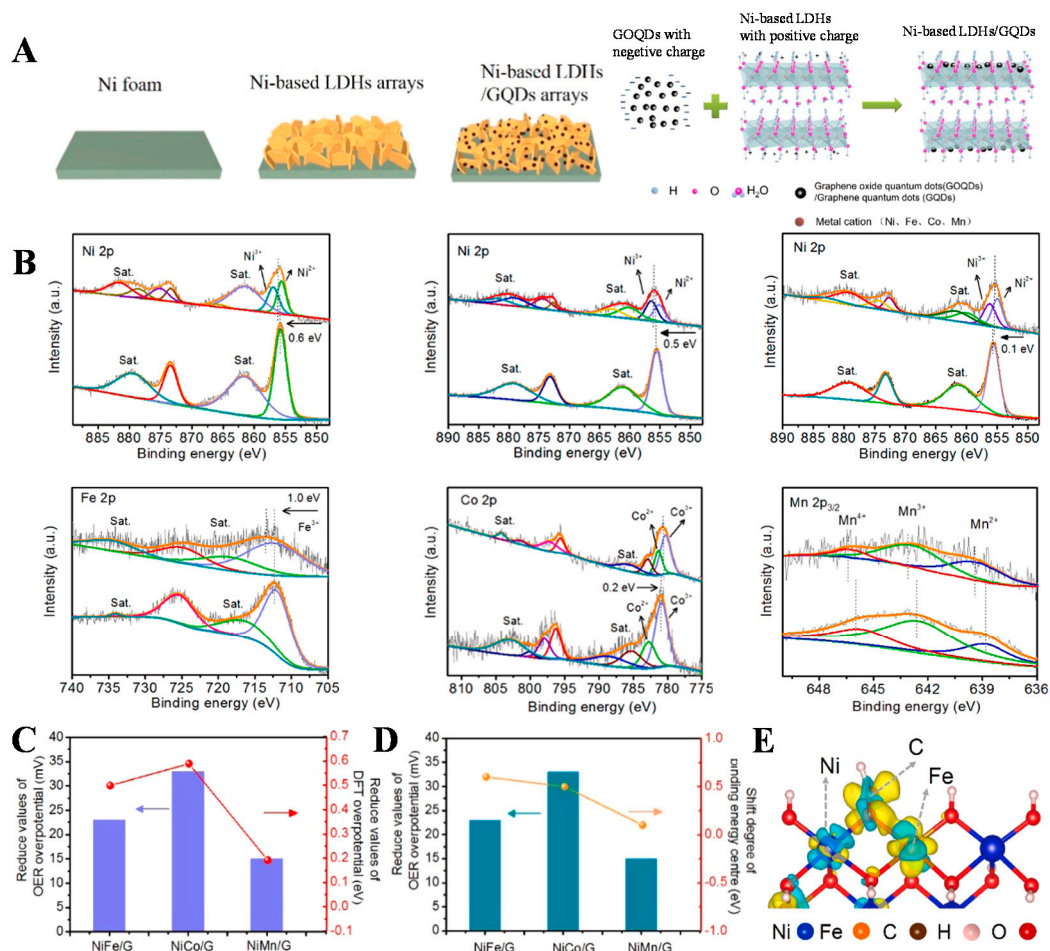


Figure 12. (A) Schematic illustration of the fabrication and synthesis principle of the Ni-based LDH/GQDs nanosheet arrays; (B) XPS spectra of the NiFe-LDHs/GQD (left), NiCo-LDHs/GQD (middle), NiMn-LDHs/GQD (right) electrocatalysts, respectively; (C) Reduced LSV overpotentials at 10 mA cm⁻² vs. shift degree of Ni 2p_{3/2} binding energy center for Ni-based LDHs/GQDs; (D) Reduced LSV overpotentials at 10 mA cm⁻² vs. reduced DFT overpotentials of Ni-based LDHs/GQDs; (E) Charge density difference of NiFe/G when O-CH bonds with Ni/Fe (iso-surface levels are 0.0036 eÅ⁻³, cyan and yellow represented electron depletion and accumulation, respectively) [178]. Copyright © 2021 Elsevier Ltd.

Metal-based materials (i.e., metal single atom, metal compounds, and 3D metal scaffolds) have been recognized as a sort of robust candidates for the enhanced electrocatalytic performance of LDHs due to their good conductivity, abundant active sites and large surface area. In particular, the integration of LDHs and 3D conductive substrates not only provides a conductive framework with numerous internal electron transport channels, but also can prevent the aggregation of catalysts and increase the effective ECSA for electrocatalytic process. For example, Zhang et al. [180] reported that single-atom Au supported on NiFe-LDHs (⁸Au/NiFe-LDHs) showed a 6-fold enhancement of OER performance by 0.4 wt.% ⁸Au decoration. Such behavior was ascribed to the charge redistribution of active Fe atoms in NiFe oxyhydroxide supported by LDHs and stabilized by interlayer CO₃²⁻ anions and H₂O molecules, resulting from the electron-donation effect of Au atoms. Generally, the core-shell nanostructure is well-known for a better stability, for being able to protect the core material from the surrounding environment. The properties of the

“core” and “shell”, and their synergistic effect, play an important role in the functions of core–shell catalysts [97]. Therefore, the construction of core–shell nanostructure has become an intriguing avenue to functionalize LDHs for OER catalysis. For instance, self-standing Cu@NiFe-LDHs/CuF (CuF stands for Cu foams) with a core–shell nanostructure: NiFe-LDHs were the “shells” and Cu nanowires were the “cores”, are shown in Figure 13A [181]. Clearly, this 3D core–shell nanostructures can provide large surface areas with increased exposure of active sites, efficient electron transport from the inner Cu NWs to the surrounding NiFe-LDHs, and a fast release of gaseous products. Additionally, the core–shell Cu@NiFe-LDHs/CuF had a good mechanical structure since the Cu NWs were directly grown on the Cu foam, and the Cu NWs firmly grasped the shell of NiFe-LDHs NSs, ensuring a good electronic transport. Summing up, the Cu@NiFe-LDHs/CuF catalyst displayed a high OER activity with an overpotential of 199 mV at 10 mA cm^{-2} , and good stability of more than 48 h at fixed current densities of 10 and 100 mA cm^{-2} in 1 M KOH solution. A similar phenomenon was also observed for NiCo₂O₄@FeNi-LDHs electrode [182]. It was found that, the core NiCo₂O₄ nanocones acted as scaffolds to offer more reactive sites and accelerate charge transfer to the shell FeNi-LDHs. Enhanced OER activity was achieved by hybridizing the conductive NiCo₂O₄ building blocks with active FeNi-LDHs into a compact structure. The authors further suggested that the electrocatalytic performance of NiCo₂O₄@FeNi-LDHs was governed by a synergy between electronic effects (core–shell) and morphological effects.

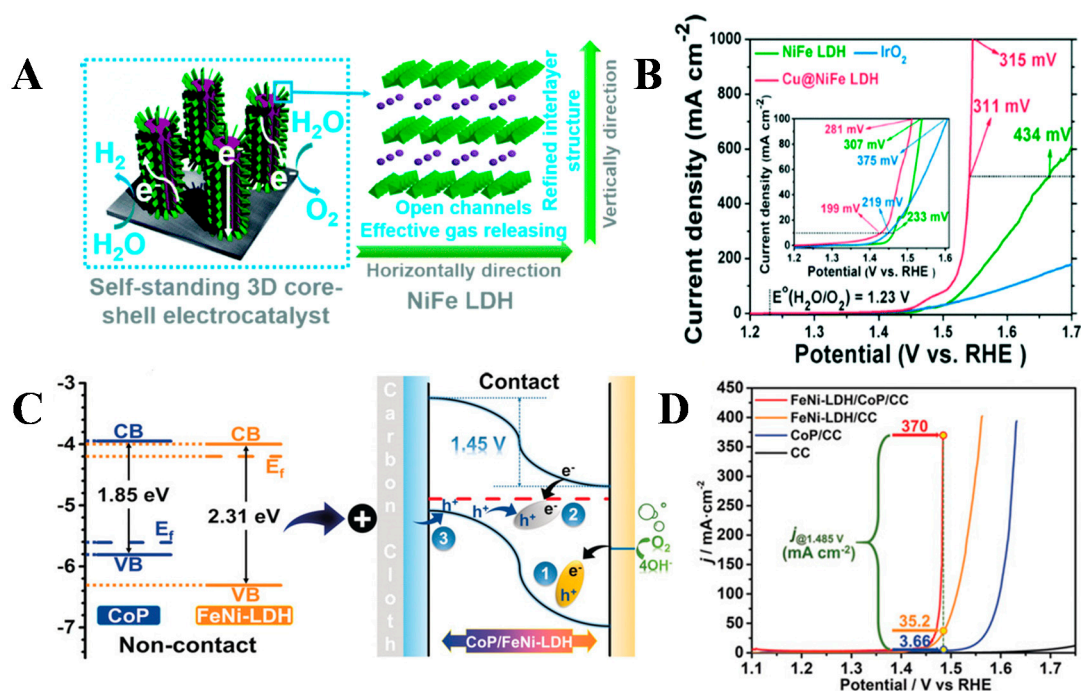


Figure 13. (A) Schematic illustration of the fabrication procedure of the self-standing 3D core–shell Cu@NiFe-LDH electrocatalysts; (B) OER performance of Cu@NiFe-LDH conducted in 1 M KOH [181]. Copyright © The Royal Society of Chemistry 2017. (C) The energy diagrams of CoP and FeNi-LDH and the proposed mechanism for electrocatalyzing OER in the FeNi-LDH/CoP/CC *p-n* junction under the condition of applying enough potential via the external circuit; (D) LSV curves toward OER in 1 M KOH electrolyte at a scan rate of 5 mV s^{-1} [183]. Copyright © 2019 Wiley-VCH Verlag GmbH & Co. KGaA, Weinheim.

To break the scaling relationship, namely, the adsorption energies of OER intermediates, a NiO/NiFe LDHs hybrid was prepared through laser ablation of urea solution and subsequent electrochemical oxidation [184]. The synchrotron radiation soft X-ray absorption spectroscopy (sXAS) analysis and spin-polarized DFT+U calculations verified that Ni⁴⁺ at the NiO/NiFe LDHs intersection was an active site for OER, and one or two additional

chemical bonds assisted it to adsorb intermediates, forming the dynamic tridimensional adsorption. In particular, the configuration of tridimensional adsorption varied with the type of intermediate, hence, the linear correlation among the adsorption energies of intermediates was broken. As a result, the scaling relationship was successfully circumvented by the NiO/NiFe LDHs composite. Liu et al. [185] constructed a NiCo₂S₄@NiFe-LDHs heterostructure by directly growing NiFe-LDHs nanosheets on NiCo₂S₄/NF precursors. This NiCo₂S₄@NiFe-LDHs/NF catalyst exhibited the improved OER performance with a low overpotential of 201 mV at the current density of 60 mA cm⁻² and low Tafel slope of 46.3 mV dec⁻¹ due to the strong interaction and electron transfer. Qiu et al. [186] synthesized hierarchically porous and hydrophilic 3D NiFe-LDHs/MXene composites through electrodeposition. Due to the strong interfacial coupling, rapid charge transfer at the interface, and high hydrophilicity of MXene, the complex showed improved electrical conductivity and fast OER process compared to the individual part, which only required a low overpotential of 300 mV to reach 500 mA cm⁻².

As is well-known, the formation of semiconductor junction can reach a state of thermal equilibrium and, especially, constitute two regions with opposite charged, and strong built-in fields at the interface can change the electron densities of the atoms around the interfaces. The NiFe-LDHs, is a typical *n*-type semiconductor. Once it is in contact with a *p*-type semiconductor forming a *p-n* junction, energy levels of E_F of *n*- and *p*-type semiconductors shift until the two are aligned in a thermal equilibrium state. Inspired by this view, He et al. [183] constructed a 3D free-standing NiFe-LDHs/CoP/carbon cloth (CC) with three-level hierarchical *p-n* junction structure. The 3D NiFe-LDHs/CoP/CC electrode only required an overpotential of 231.1 mV to deliver the current density of 20 mA cm⁻² in 1 M KOH solution. Notably, the current density at 1.485 V of NiFe-LDHs/CoP/CC achieved ~10-fold and ~100-fold increase compared to those of *n*-type NiFe-LDHs/CC and *p*-type CoP/CC, respectively, in Figure 13B. The energy-level diagrams illustrated that in the intimate-contact interface, the electrons flowed from *p*-type CoP to *n*-type NiFe-LDHs until the E_F of CoP and NiFe-LDHs turned to be aligned, which lead to opposite space-charge region at the *p-n* junction interface and further resulted in energy level shifting and band edge bending. As a result, positively charged active centers at the surface of NiFe-LDHs can effectively adsorb the OH⁻ ions, while the electrons of OH⁻ transferred to the valence band (VB) of NiFe-LDHs, and then recombined with the holes at the VB of NiFe-LDHs. The redundant electrons at the conduction band (CB) of NiFe-LDHs further recombined with the holes at VB of CoP to keep the charge balance. The above representative LDHs electrocatalysts for the OER process, modulated by various strategies, are summarized in Table 1.

Table 1. Representative LDHs electrocatalysts for the OER process in 1 M KOH electrolyte.

Catalysts	Modification Method	Overpotential/mV	Tafel Slope/mV dec ⁻¹	Stability	Ref.
Co ²⁺ -doped NiFe-LDHs	Cation-doping	264@10 mA cm ⁻²	58.1	10 h	[132]
Co ³⁺ -doped NiFe-LDHs	-	249@10 mA cm ⁻²	50.5	10 h	[132]
Ni ₆ Fe ₂ Cr ₁ -LDHs	-	225@25 mA cm ⁻²	69	At 10 mA cm ⁻² for 6 h	[187]
NiFeZr-LDHs	-	198@10 mA cm ⁻²	53.1	At 1.47 V for 12 h	[188]
Mn ²⁺ -doped NiFe-LDHs	-	190@10 mA cm ⁻²	68.6	At 50 mA cm ⁻² for 40 h; 750 cycles at 5 mV s ⁻¹	[128]
NiFeV-LDHs	-	195@20 mA cm ⁻²	42	At 1.48 V for 18 h	[134]
NiVRu-LDHs	-	190@10 mA cm ⁻²	83	2000 cycles; at 50 mA cm ⁻² for 600 h; at 200 mA cm ⁻² for 400 h	[189]
NiFeMn ⁴⁺ -LDHs	-	289@20 mA cm ⁻²	47	At $\eta = 310$ mV for 15 h; at 10 mA cm ⁻² for 15 h	[129]
NiVlr-LDHs	-	203@10 mA cm ⁻²	55.3	At 10 mA cm ⁻² for 15 h	[190]

Table 1. Cont.

Catalysts	Modification Method	Overpotential/mV	Tafel Slope/mV dec ⁻¹	Stability	Ref.
NiCoRu-LDHs	-	270@100 mA cm ⁻²	40	At 100 mA cm ⁻² for 55 h	[191]
CoFeV-LDHs	-	242@10 mA cm ⁻²	57	At $\eta = 250$ mV for 32 h	[192]
CoFeCr-LDHs	-	270@100 mA cm ⁻²	32	At 1.58 V for 24 h	[193]
Cr-CoFe LDHs	-	238@10 mA cm ⁻²	107	1000, 3000, and 5000 cycles at 50 mV s ⁻¹ ; at 20 mA cm ⁻² for 20 h	[135]
W _{0.5} Co _{0.4} Fe _{0.1} -LDHs	-	310@100 mA cm ⁻²	32	3000 cycles at 5 mV s ⁻¹ ; at 20 mA cm ⁻² for 50 h	[194]
CoMoV-LDHs	-	270	106	At $\eta = 300$ mV for 20 h	[195]
ZnFe-VO ₄ -LDHs	Anion-intercalation	250@10 mA cm ⁻²	26	At 2.4 V for 4000 s; 200 cycles at 200 100 mV s ⁻¹	[196]
NiFe-WO ₄ -LDHs	-	290@10 mA cm ⁻²	41.5	At 10 mA cm ⁻² for 20 h	[197]
Ni ₂ Fe-SDS-LDHs/CFP	-	289@10 mA cm ⁻²	39	At 50 mV s ⁻¹ for 10 h	[60]
H ₂ PO ₂ ⁻ /NiFe-LDHs	-	250@10 mA cm ⁻²	37.7	30,000 s	[143]
Formamide intercalated NiFe-LDHs/CR	-	210@10 mA cm ⁻²	39	At 0.5 V for 18 h	[146]
NiFe-LDHs (POM)	-	287@10 mA cm ⁻²	43	At 50 mA cm ⁻² for 35 h; at 10 mA cm ⁻² for 40 h	[198]
0.05-SB-Ni _{0.8} Fe _{0.2} (OH) ₂	-	301@10 mA cm ⁻²	42	250, 500, 750 and 1000 cycles at 100 mA s ⁻¹ ; at $\eta = 300$ mV for 20 h	[199]
R-NiFe-LDHs	Defect engineering	200@10 mA cm ⁻²	59.3	at 1.43 V for 10 h	[155]
CoFe-LDHs-Ar	-	266@10 mA cm ⁻²	37.85	2000 CV cycles at 5 mV s ⁻¹	[165]
PM-LDHs	-	230@10 mA cm ⁻²	47	At $\eta = 230$ mV for 100 h	[158]
N-CoFe-LDHs	-	310@10 mA cm ⁻²	74	10 h	
NiFe-LDHs-V _{Fe}	-	255@10 mA cm ⁻²	70	2000 cycles at 10 mA cm ⁻²	[49]
NiFe-LDHs-V _{Ni}	-	229@10 mA cm ⁻²	62.9	2000 CV cycles at 10 mA cm ⁻²	[49]
D-NiFeZn-LDHs	-	200@20 mA cm ⁻²	34.9	At 30 mA cm ⁻² for 10 h	[200]
ZnCo-UF	ultrathin nanosheets	360@10 mA cm ⁻²	66		[163]
NiFe-LDHs	-	254@10 mA cm ⁻²	32	At $\eta = 254$ mV for 12 h	[170]
E-CoFe-LDHs	-	302@10 mA cm ⁻²	41	At 10 mA cm ⁻² for 10 h	[159]
DH-CoFe-LDHs	-	276@10 mA cm ⁻²	40.3	At $\eta = 276$ mV for 10 h	[169]
N-CoFe-LDHs	-	233@10 mA cm ⁻²	40.03	2000 cycles at 5 mV s ⁻¹	[201]
Ni ₃ FeAl _{0.91} -LDHs/NF	-	304@10 mA cm ⁻²	50	18 h	
NiFe-LDHs	-	300@10 mA cm ⁻²	40	At 10 mA cm ⁻² for 13 h	[160]
FeNi-GO	LDH/carbon composites	206@10 mA cm ⁻²	39	At 10 mA cm ⁻² for 8 h	[202]
NiFe-LDHs-NS@DG10	-	210@10 mA cm ⁻²	52	At 5 mA cm ⁻¹ for 10 h; at 10 mA cm ⁻¹ for 10 h	[203]
NiFe LDHs/GQDs	-	189@10 mA cm ⁻²	52.1	At 10 mA cm ⁻² for 15 h	[178]
CoFe-LDHs/TEG	-	301@10 mA cm ⁻²	80	At 1.50 V for 25 h	[179]
NiFe-LDHs/CNT	-	290@10 mA cm ⁻²	31	At 10 and 20 mA cm ⁻² for 1 h	[116]

Table 1. Cont.

Catalysts	Modification Method	Overpotential/mV	Tafel Slope/mV dec ⁻¹	Stability	Ref.
Ce-NiFe-LDHs/CNT	-	227@10 mA cm ⁻²	33	At 10 mA cm ⁻² for 30,000 s	[204]
Ag NWs/Ni _{0.95} Fe _{0.05} -LDHs	LDHs/Metal Compounds	330@10 mA cm ⁻²	89	At 10 mA cm ⁻² for 12 h	[205]
FeNi-LDHs/FeNi foil	-	130@10 mA cm ⁻²	39.8	At 1.5 V for 10 h	[206]
FeNi-LDHs@NWSSF	-	210@10 mA cm ⁻²	56	At 10 mA cm ⁻² for 18 h	[207]
FeOOH/NiFe-LDHs	-	174@10 mA cm ⁻²	27	1000 cycles at 300 mV s ⁻¹ ; at 10 mA cm ⁻² for 25 h; at 50 mA cm ⁻² for 15 h	[208]
NiO/NiFe-LDHs	-	205@30 mA cm ⁻²	30	At 20 mA cm ⁻² for 10 h	[184]
NiMn-LDHs/NiCo ₂ O ₄	-	310@10 mA cm ⁻²	99	1000 cycles at 10 mA cm ⁻² ; at 1.65 V for 8 h	[209]
Ni ₃ S ₂ /NiFe-LDHs	-	200@10 mA cm ⁻²	29.71	1000 cycles at 2 mV s ⁻¹ ; at 10 mA cm ⁻² for 45,000 s	[210]
NiFe-LDHs/(NiFe)S _x /CMT	-	210@10 mA cm ⁻²	31	1000 cycles at 10 mA cm ⁻² ; at 10 mA cm ⁻² for 15 h	[211]
FeNi-LDHs/CoP	-	254@350 mA cm ⁻²	33.5	18.5 h	[183]
Ni ₅ P ₄ /NiP ₂ /NiFe-LDHs	-	197@10 mA cm ⁻²	46.6	At 10, 100, and 200 mA cm ⁻² for 24 h	[212]
FeNi-LDHs/Ti ₃ C ₂ -MXene	-	240@10 mA cm ⁻²	43	At 10 mA cm ⁻² for 12 h	[213]
FeCo-LDHs/MXene	-	268@10 mA cm ⁻²	85	At 10 mA cm ⁻² for 30,000 s	[214]

4. Applications of LDHs-Based Bifunctional Electrocatalysts

Bifunctional electrocatalysts with both brilliant ORR and OER, or HER and OER performance are essential for energy conversion and storage devices, such as rechargeable zinc-air batteries (ZABs), unitized regenerative fuel cells (URFCs), electrolyzers, and so on. In such closed-loop systems, the essential component is the desired bifunctional oxygen electrode catalysts with high catalytic activity, long-term durability, and strongly resistance to anodic corrosion. Although the LDHs show a promising OER activity, the intrinsically poor electrical conductivity, and easily degradable active sites due to stacking of the material greatly prevent them from serving as bifunctional ORR/OER catalysts. It is fascinating to design and build a bifunctional oxygen electrode catalyst based on the combination of highly OER-active LDHs and highly ORR-active materials like conductive metals, carbon materials, and M-N-C compounds.

The hierarchical structure design and novel material chemistry endow high activity propelling O₂ redox. Inspired by the excellent electrical conductivity of Ag, Hwang's group [215] developed a hierarchical 3D core-shell architecture, where the shell NiMn-LDHs nanosheets, was grown on the Ag nanowires (NWs) core, labeled as Ag NWs@NiMn-LDHs. This latter exhibited a preeminent bifunctional activity with onset potentials of 0.19 V and 0.27 V for OER and ORR, respectively. Furthermore, the Ag NWs@NiMn-LDHs had an outstanding overvoltage difference (ΔE) of 0.75 V between the OER overpotential at the current density of 10 mA cm⁻² and the ORR half-wave overpotential at the current density of -3 mA cm⁻². Analogously, Ag nanoparticles decorated NiRu-LDHs nanosheets (Ag NPs/NiRu-LDHs) were reported as bifunctional catalysts (Figure 14A) [216]. The Ag NPs/NiRu-LDHs revealed significantly higher ORR/OER bifunctional activity than

pristine NiRu-LDHs in alkaline conditions, cf. Figure 14B. They inferred that the enhanced ORR activity of Ag NPs/NiRu-LDHs was mainly attributed to the increased Ag sites and accessible Ag site populations; the increase in the OER activity was due to intrinsically active Ni sites with multiple vacancies (oxygen vacancy, V_O and metal vacancies, V_M) after decoration strategy. The extraordinary low overpotential for ORR/OER was ascribed to the synergetic effects between Ag NPs and NiRu-LDHs.

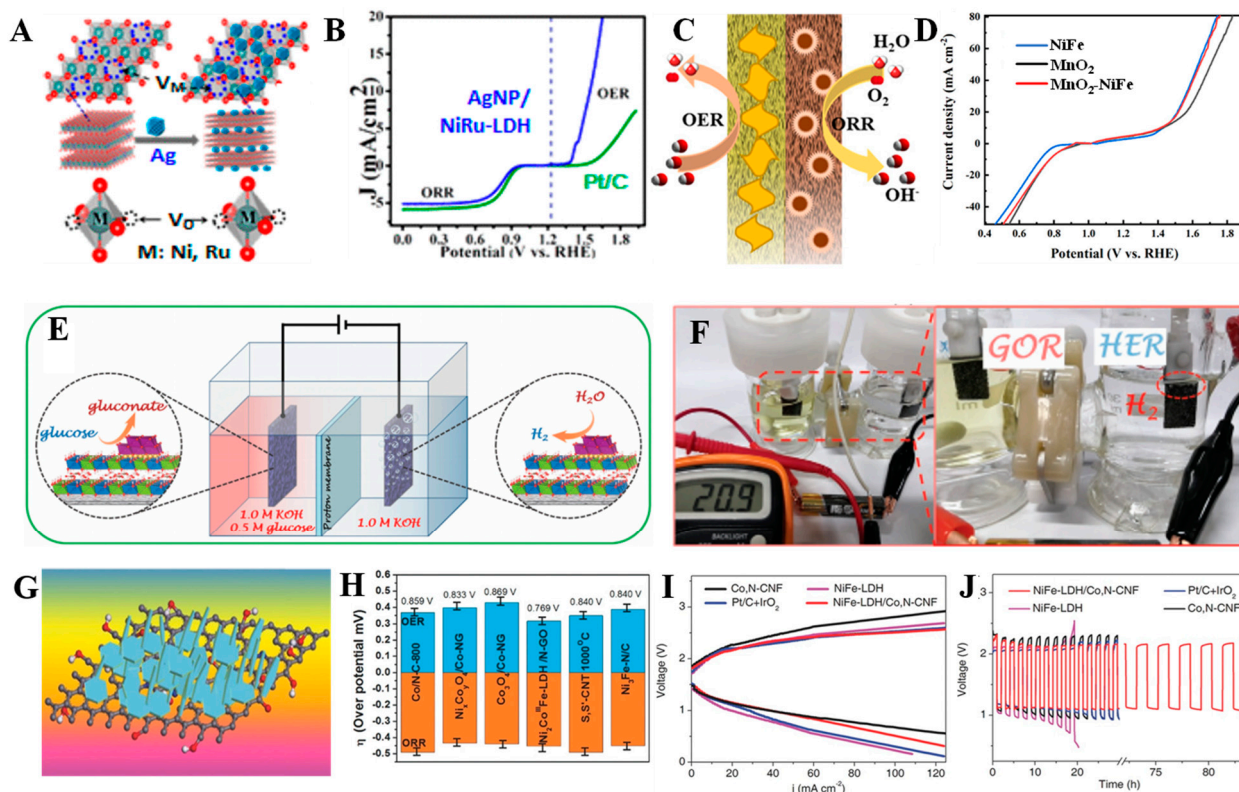


Figure 14. (A) Formation of metal/oxygen vacancies (V_M , V_O) in LDHs; (B) Bifunctional catalytic activity of Ag NP/NiRu-LDHs and commercial Pt/C catalysts toward ORR/OER activities at 1600 rpm in 0.1 M KOH electrolyte [216]. Copyright © 2018 American Chemical Society. (C) Schematic illustration of the selective growth for the fabrication of Janus MnO_2 -NiFe/Ni with the assistance of Vaseline. (D) OER and ORR polarization curves of air electrodes at 1600 rpm in 1 M KOH solution [217]. Copyright © 2019 American Chemical Society. (E) Structural representation of the asymmetrical electrolytic cell (AEC). (F) Electrolysis test with AA battery (1.5 V rated voltage) as the power source [218]. Copyright © 2021 Wiley-VCH GmbH. (G) Schematic of the in situ growth of LDH nanosheets on nitrogen doped GO (N-GO); (H) Individual ORR and OER, and total overpotentials for $Ni_2Co^{III}Fe$ -LDH/N-GO of this study in comparison to the published literature [219]. Copyright © 2017 WILEY-VCH Verlag GmbH & Co. KGaA, Weinheim. (I) Charge and discharge polarization curves of rechargeable zinc-air batteries in 6 M KOH and 0.2 M zinc acetate. (J) Charge and discharge cycling curves of rechargeable zinc-air batteries at a current density of 25 mA cm^{-2} [220]. Copyright © 2017 WILEY-VCH Verlag GmbH & Co. KGaA, Weinheim.

Wang et al. [217] designed a hierarchical structure constructed a MnO_2 -NiFe Janus electrode by selectively electrodepositing MnO_2 and NiFe-LDH on two sides of a porous nickel foam (MnO_2 -NiFe/NF), in which the MnO_2 nanoflakes and NiFe-LDHs nanosheets served as the ORR and OER active centers, respectively (Figure 14C). Such a Janus MnO_2 -NiFe air electrode endowed the zinc-air battery with better cycling stability and energy efficiency than the bare MnO_2 and NiFe-LDHs electrodes, as illustrated in Figure 14D. In another interesting example, a bifunctional electrocatalyst: Fe_3O_4 /Au/CoFe-LDH with sandwich structured, was used for the hydrogen evolution reaction and the electrocatalytic glucose oxidation reaction (GOR) [219]. The combination of structural characterizations with electrochemical characterizations revealed that Fe_3O_4 and CoFe-LDHs played key roles in catalyzing the HER, whereas metallic Au was responsible for the GOR, Figure 14E.

In a self-assembled asymmetrical electrolyzer-cell, in which the two-electrode electrolysis test was carried out using an AA battery (1.5 V rated voltage), the current density could achieve 20.9 mA cm^{-2} , cf. Figure 14F. During the test, bubbles were only observed on the cathode, while the solution in the anode compartment gradually turned yellow, indicating the formation of gluconate. These results manifested that this bifunctional electrocatalyst, built in a two-electrode cell system, achieved the replacement for OER with organic molecules oxidation reaction.

Nitrogen-doped graphene oxides (N-doped GO), as one of conductive carbon materials, with numerous functional oxygen groups ($-\text{OH}^-$, $-\text{CO}$, $-\text{COO}^-$) and defects, not only can provide catalysts with good hydrophilicity, but also provide ideal sites for metal sites to anchor by electrostatic force. Hence, the combination of ORR-active N-doped GO and LDHs materials have also been considered as an effective method for designing highly bifunctional electrocatalysts towards ORR and OER [218,221–226]. For example, a ternary $\text{NiCo}^{\text{III}}\text{Fe-LDHs}$ electrode with Co^{3+} grafted on nitrogen-doped graphene oxide (N-GO) was fabricated by an in situ growth route, and used as a bifunctional catalyst for ORR and OER (Figure 14G,H) [218]. The $\text{NiCo}^{\text{III}}\text{Fe-LDHs/N-GO}$ had a low overvoltage difference of 0.77 V between ORR and OER, which can be attributed to the following key factors: (i) the high valence state Co, i.e., Co^{3+} , possessed a positive effect on the electrocatalytic performance of ORR and OER; (ii) the pyridinic-N and graphitic-N in N-GO could alter the electron density of carbon atoms so as to facilitate the adsorption of O_2 and break of O–O bonds in the ORR process; (iii) the enlarged surface area (SA) led to a highly exposure of Ni and Fe active sites; and (iv) the intimate contact between N-GO and LDHs brought out a high conductivity. Hou's group [224] prepared NiFe-LDHs supported in reduced graphene oxides (NiFe-LDHs/rGO) nanohybrid as an efficient bifunctional electrocatalyst towards ORR and OER in alkaline medium. The NiFe-LDHs/rGO nanohybrid exhibited a better bifunctional performance than NiFe-LDHs and NiFe-LDH/GO counterparts, which can be credited to the fast electron/charge transfer and the synergistic effect of NiFe-LDHs and rGO in NiFe-LDHs/rGO system.

Recently, the zeolitic imidazolate frameworks (ZIFs), a subclass of metal-organic frameworks, consisted of metal cations (e.g., Zn^{2+} , Co^{2+} , etc.) and N-containing organic linkers (e.g., 2-methyl imidazole), are used as a precursor to controllably synthesize metal, N-codoped carbon nanoframes (metal, N-CNFs), which possesses a high surface area, excellent conductivity, and metal, N-codoped active sites. In addition, the metal, N-CNFs show excellent electrocatalytic performance for ORR [227–229]. Consequently, combining LDHs with metal, N-CNFs becomes an up-to-date strategy for the development of efficient bifunctional catalysts. Zhang et al. [220] reported a NiFe-LDHs/ Co,N-CNF hybrid electrocatalyst, in which NiFe-LDH nanoparticles with the particle sizes of 3–5 nm were anchored on the Co,N-co-doped carbon supports. The high conductivity and homogeneously distribution of N-doped defects for Co,N-CNF support endowed the NiFe-LDHs/ Co,N-CNF with an excellent bifunctional activity, demonstrating an OER overpotential of 0.31 V at 10 mA cm^{-2} and an ORR half-wave potential of 0.79 V. Moreover, the self-assembly rechargeable zinc-air battery with NiFe-LDHs/ Co,N-CNF electrocatalyst delivered a narrow discharge-charge voltage gap (1.0 V at 25 mA cm^{-2}) over 80 h operation, which outperformed the rechargeable zinc-air batteries constructed using Co, N-CNF, NiFe-LDHs, and Pt/C + IrO_2 catalysts, respectively, cf. Figure 14I,J.

In order to alleviate the competition of the active sites for occupying the efficient positions, it is necessary to rationally design and arrange the active sites on the specific positions and ensure fully exposure to the dual-pathway of electron conduction and ion transportation in the multiphase electrocatalysis. As an example, Zhang et al. [230] proposed a multi-scale construction strategy to rationally integrate various active sites into a composite electrocatalyst (LDH-POF) to achieve superb bifunctional electrocatalytic performances for long-lifespan rechargeable zinc-air batteries. Here, the carbon nanotubes (CNTs) were employed as the scaffolds to anchor the active sites thanks to their high conductivity to construct electron conduction path-ways and the wearability to form porous

structures to strengthen ion transportation. Second, cobalt coordinated porphyrin and NiFe-LDHs were selected as ORR and OER active sites, respectively. In Figure 15A–C, the resulting LDH-POF composite exhibited remarkable bifunctional performances with a small voltage gap of 0.68 V and enabled the rechargeable zinc-air batteries with a low discharge/charge voltage gap, a power density of 185.0 mW cm^{-2} , and an ultralong lifespan of more than 2400 cycles at the current density of 5.0 mA cm^{-2} . Later, this group further fabricated CoNC@LDHs composite for both ORR and OER through a two-step synthesis route. Specifically, the cobalt coordinated framework porphyrin was in situ coaxially coated on the CNT network surface to introduce atomic-level Co-N-C ORR sites, followed by the coprecipitation of hydrophilic NiFe-LDHs nano particles as OER active sites (Figure 15D) [231]. Owing to the increased hydrophilicity and strengthened ion/electron pathway, the CoNC@LDHs composite electrocatalyst delivered a ΔE of 0.63 V, significantly outperforming the noble-metal-based electrocatalyst ($\Delta E = 0.77 \text{ V}$), cf. Figure 15E. Additionally, the constructed rechargeable zinc-air battery achieved a power density of 173 mW cm^{-2} , and an ultralong lifespan (over 3600 cycles @ 10 mA cm^{-2}) with a stable charge/discharge voltage difference of 0.76 V. It also exhibited excellent cycling current density (100 mA cm^{-2}), surpassing that of the noble-metal catalysts (Figure 15F). This work highlights the integration of hydrophilic and conductive synergy in the search of efficient, durable, and bifunctional catalysts for ORR and OER processes. Yang et al. [232] developed a novel CoFe-LDHs coupled with NiFe-LDHs nanosheet array supported on nickel foam (denoted as CoFe@NiFe/NF) through a facile hydrothermal and electrodeposition method. Benefiting from strong synergistic effect between CoFe-LDHs and NiFe-LDHs and the 3D interconnected architectures, the resulting CoFe@NiFe/NF catalyst exhibited excellent activities and stabilities for both OER and HER. Furthermore, an efficient and stable alkali-electrolyzer using CoFe@NiFe/NF, as cathode and anode, achieved a voltage of 1.59 V at the current density of 10 mA cm^{-2} .

Apart from the combination of LDHs with other ORR-active nanomaterials, a variety of LDHs-derived catalysts are also employed as bifunctional electrocatalysts to catalyze oxygen electrode reactions (ORR/OER). Compared with traditional transition-metals catalysts, multifunctional catalysts derived from LDHs precursors via the topological structure transformation, show unique nano-size effect, high dispersion, and synergistic interaction, which are conducive to the improvement of electrocatalytic performances. The abundant interfaces are obtained simultaneously that may be beneficial for the electrocatalysis. Moreover, the in situ preparation of heterogeneous catalysts from LDHs is considered to be more chemically stable in comparison with the LDHs. The LDHs' derivatives are usually prepared by a simple heat-treatment, viz. confinement synthesis strategy based on transformation. Zhong and Feng [233] fabricated a $\text{CoN}_y/\text{NiFeO}_x/\text{C}$ electrocatalyst by annealing the phthalocyanine cobalt tetrasulfonate (CoPcTs) intercalated Ni_2Fe -LDHs precursor under N_2 atmosphere. The key aspects of this bifunctional electrocatalyst, for the reversible oxygen electrodes, was the mutual incorporation of the ORR-active sites (CoN_y), and OER-active ones (spinel NiFeO_x), respectively, derived from the interlayer CoPcTs^{2-} anions and the nickel-iron host sheet in the same LDHs system. The $\text{CoN}_y/\text{NiFeO}_x/\text{C}$ composite afforded an excellent bifunctional activity with a ΔE of 0.84 V in alkaline media, and a remarkable stability in alternating modes (fuel cell mode/electrolyzer mode) in a $\text{H}_2\text{-O}_2$ laminar flow unitized regenerative micro-cell (LFURMC). Similarly, based on the host-guest transformation of LDHs, the organic molecule-intercalated CoAl-LDHs as precursors were subjected to the calcination and acid etching treatment, producing cobalt (Co) single atoms catalysts (denoted as IE-SACs), as demonstrated in Figure 16A [234]. The metanilic acid (MA) was selected as intercalation molecules to provide highly N species to form Co-N active sites, whereas the p-toluenesulfonic acid (PA) served as the other co-intercalation molecules and can promote the exposure of Co single atoms. As a result, the IE-SACs(PA+MA) catalyst had a small potential gap (ΔE) of 0.72 V for ORR/OER processes. Moreover, the self-assembled liquid ZAB with the IE-SACs(PA+MA) displayed an open circuit voltage of 1.42 V and a peak power density of 65 mW cm^{-2} , which were

higher than those of IE-SACs(PA)- and IE-SACs(MA)-assembled liquid ZABs (Figure 16B). At a discharge density of 5 mA cm^{-2} , in Figure 16C, the IE-SAC(PA+MA)-assembled liquid ZAB delivered a high discharge voltage of 1.2 V with a specific capacity of 690.3 mAh g^{-1} and an energy density of 963.3 Wh kg^{-1} .

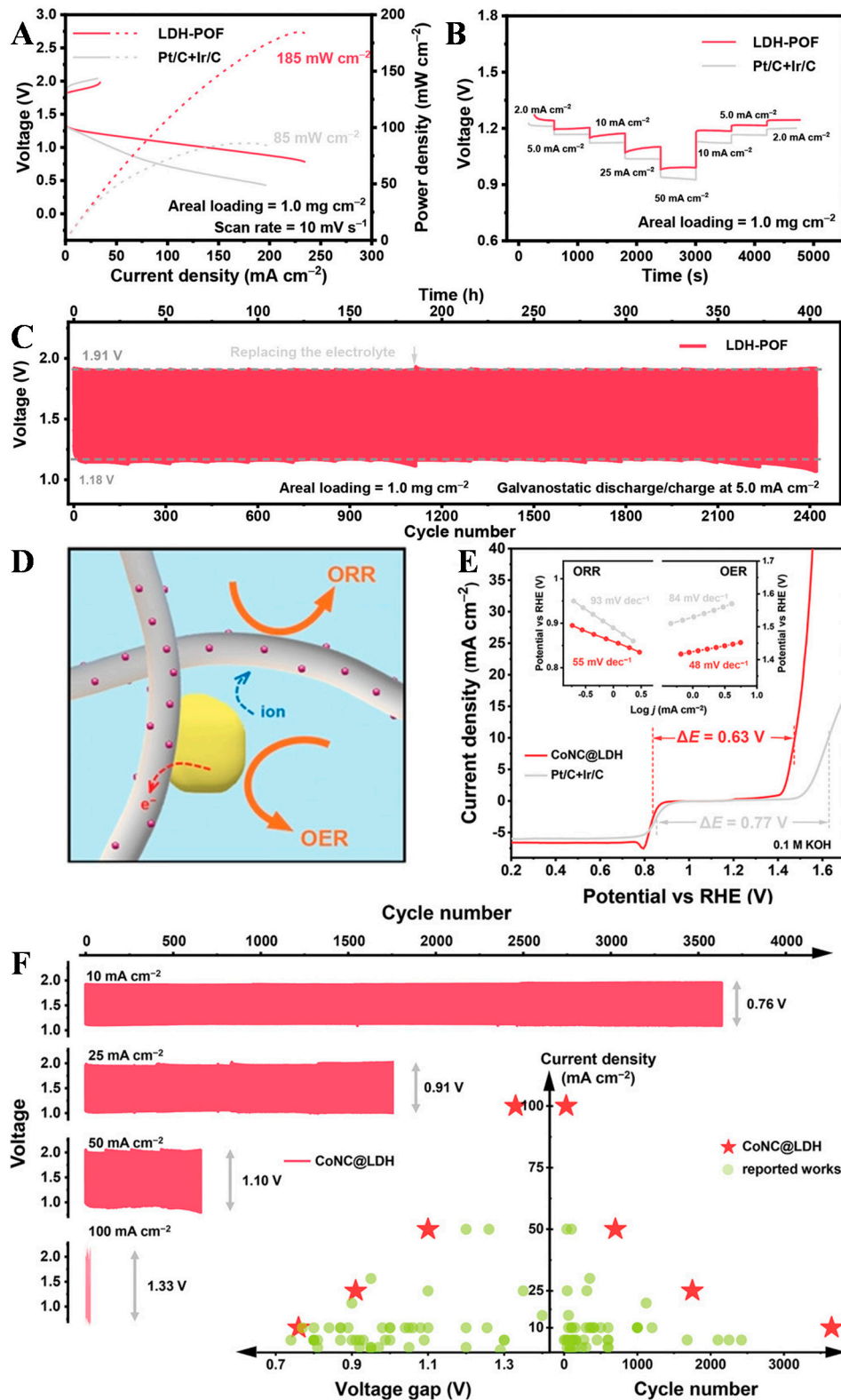


Figure 15. (A) Charge and discharge polarization profiles and discharge power density, the electrolyte was 6.0 M KOH aqueous solution containing $0.20 \text{ M Zn(CH}_3\text{COO)}_2$; (B) Rate performances of the LDH-POF and Pt/C+Ir/C cathodes; (C)

Galvanostatic cycling curves at 5.0 mA cm^{-2} of the LDH-POF and Pt/C+Ir/C cathodes [230]. Copyright © 2020 WILEY-VCH Verlag GmbH & Co. KGaA, Weinheim. (D) Schematic diagram of the synergy between each component in the CoNC@LDH electrocatalyst; (E) Bifunctional performance evaluation and comparison, the inset is the corresponding Tafel plots for ORR and OER, respectively at 1600 rpm in 0.1 M KOH alkaline electrolyte; (F) Long-term durability evaluations on rechargeable ZABs [231]. Copyright © 2021 Wiley-VCH GmbH.

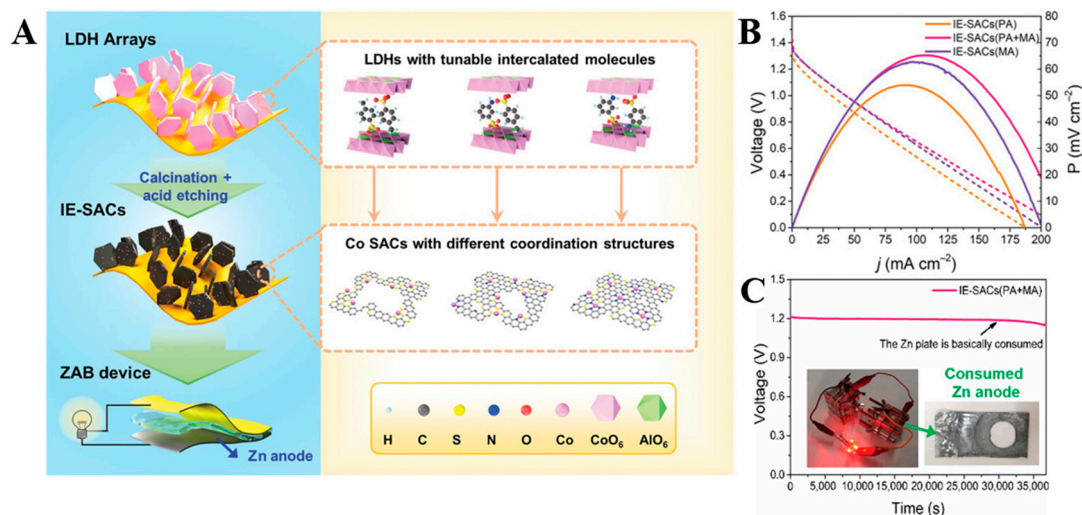


Figure 16. (A) Schematic representation of IE-SACs obtained via confinement synthesis strategy. (B) Polarization curves and corresponding power density plots of the liquid ZABs, 6 M KOH + 0.2 M zinc acetate as the electrolyte. (C) Galvanostatic discharge curves of the IE-SAC(PA+MA)-assembled liquid ZAB at 5 mA cm^{-2} [234]. Copyright © 2020 Wiley-VCH GmbH.

Moreover, on account of the unique electronic property and high intrinsic reactivity, the transition-metals nitrides (TMNs) and chalcogenides (TMCs) derived from LDHs precursor have also been investigated as bifunctional catalysts capable of driving both OER and ORR. For example, Fu et al. [235] reported a highly efficient bifunctional ORR/OER electrocatalyst: Ni₃FeN microspheres with porous structure, synthesized by the thermal ammonolysis of NiFe-LDHs microspheres. As compared with the Ni₃Fe alloy and NiFeO_x catalysts prepared by calcination of the NiFe-LDHs precursor under H₂ and N₂ atmospheres, respectively, the Ni₃FeN catalyst exhibited better bifunctional electrocatalytic activity and stability, which was mainly attributed to the high electrical conductivity rooted in its typical metallic characteristic. In addition, Ni₃N electrocatalysts have also shown remarkable HER activity because of its small ΔG_{H^+} due to the Ni–N co-effect [236], but the HER activity of nickel nitrides in alkaline media is still unsatisfactory for practical applications due to their sluggish water dissociation kinetics. Recently, metal hydroxides or oxides are selected as water cleavage “promoters” for cleaving HO–H bonds to produce hydrogen species to increase the alkaline HER activity [237]. As an example, Wang et al. designed and fabricated a bifunctional electrocatalyst, 3D hierarchical heterostructure NiFe-LDHs@Ni₃N nano/microsheet arrays on Ni foam (NiFe-LDHs@Ni₃N/NF), showing a low cell voltage of 1.80 V at a current density of 500 mA cm^{-2} with a remarkable durability of 100 h in an alkaline aqueous electrolyzer [238]. Such bifunctional OER/HER performance was ascribed to the strong coupling and synergistic effects between the NiFe-LDHs nanosheets and the Ni₃N micro-sheet arrays, which provides a robust integrated structure and fast electron transfer.

Considering the high ORR-active activity of Co,N-CNF derived from Zn,Co-ZIFs, a novel Ni₃FeN/Co,N-CNF hybrid was fabricated by Wang et al. [239], which delivered an improved bifunctional activity with a ΔE of 0.69 V, lower than those of Ni₃FeN (1.00 V) and Co,N-CNF (0.86 V). The constructed rechargeable zinc–air battery using the Ni₃FeN/Co,N-CNF hybrid displayed a steady operation over 540 h at 6 mA cm^{-2} with a small initial

discharge-charge voltage gap of 0.79 V. In another case, cobalt-based hydroxysulfides ($\text{CoMS}_x(\text{OH})_y$, $M = \text{Fe, Al}$) with high intrinsic activity and electrical conductivity were presented as bifunctional ORR/OER electrocatalysts for ZABs device [240]. In a typical procedure, the CoAl-LDHs were immersed in a high-concentration S^{2-} solution at room temperature, and then the S^{2-} ions continuously replaced the OH^- in the solid phase according to the solubility equilibrium ($K_{\text{sp}}[\text{Co}(\text{OH})_2] = 1.6 \times 10^{-15}$, $K_{\text{sp}}[\text{CoS}] = 4 \times 10^{-21}$ at 25 °C). The electron structure of the active transition-metals sites was adjusted by S^{2-} anions modulation. The $\text{Co}_3\text{FeS}_{1.5}(\text{OH})_6$ hydroxysulfides were assembled in the air electrode for a rechargeable ZAB with a small overpotential of 0.86 V at 20.0 mA cm^{-2} , a high specific capacity of 898 mAh g^{-1} , and a long cycling life, which was much better than Pt and Ir-based electrocatalysts in the same systems. Dai's group designed 2D rhenium disulfide (ReS_2)/NiFe-LDHs materials grown on the carbon fiber paper (CFP) for a "one device-two functions" system by integrated cascade Zn-air battery/electrolyzer, which can be efficiently switched between electricity storage (of Zn-air battery) and power-to-gas conversion (of electrolyzer) modes [241]. It was pointed out that the edge and surface sites of NiFe-LDHs were responsible for both OER and ORR activities, while the unprecedented activity of the ReS_2 /NiFe-LDHs for HER emerged from the S–O bonds at the heterointerfaces, together with the strong coupling effect of NiFe-LDHs and ReS_2 . As shown in Figure 17A, a voltage of 1.60 V was obtained at 10 mA cm^{-2} , indicating an overpotential of only 370 mV for the overall water electrolysis when ReS_2 /NiFe-LDHs hetero-nanosheets electrocatalyst served as both the anode and cathode. The ReS_2 /NiFe-LDHs hybrids exhibited a robust durability for water electrolysis upon a long-term operation at different current densities of 10, 20, 50, 100, and 200 mA cm^{-2} , respectively, Figure 17B. The total Faraday efficiency (FE) for the self-powered system was calculated to be $\sim 32\%$, Figure 17C. The integrated system, when used as cascade electrolyzers, can produce H_2 continuously with a high FE of $\sim 96\%$, while working as cascade Zn-air batteries, featuring a round-trip efficiency of $\sim 61\%$. In short, using the ReS_2 /NiFe-LDHs hetero-nanosheets electrocatalyst as shared electrodes, the newly developed integrated cascade system can be readily and efficiently switched between the battery and electrolyzer modes, realizing "one device-two functions", Figure 17D. Additionally, some typical bifunctional LDHs-based ORR/OER electrocatalysts are summarized in Table 2.

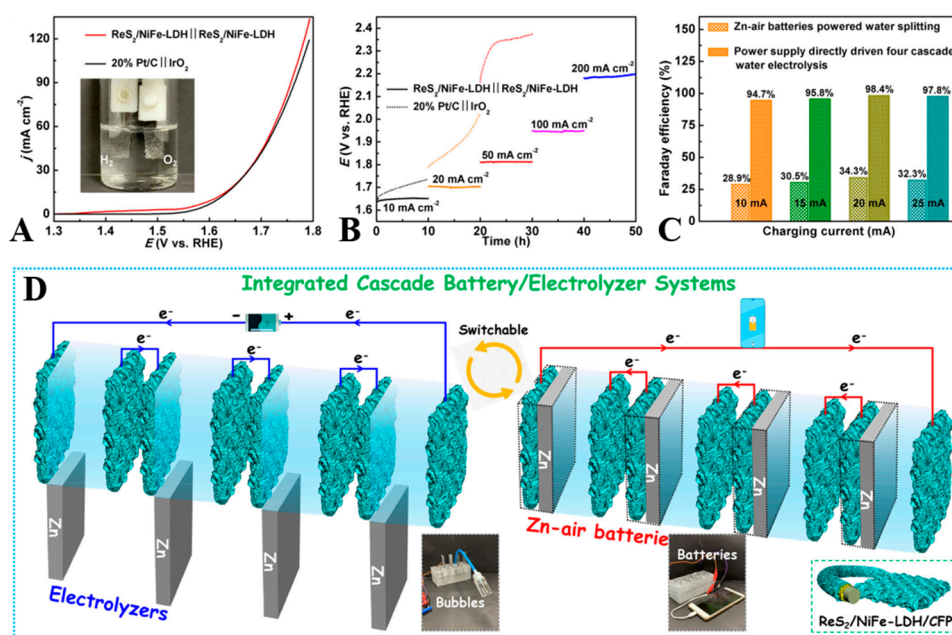


Figure 17. (A) Overall water electrolysis LSV curves of the ReS_2 /NiFe-LDH|| ReS_2 /NiFe-LDHs and 20% Pt/C|| IrO_2 in 1 M KOH solution. Insets show the digital photograph of the two-electrode configuration. (B) Chronopotentiometry curves at various current densities. (C) Faraday efficiencies of the Zn-air batteries-powered water electrolysis and the power supply

directly driven four-cascade water electrolysis at different charging current. (D) Schematic illustration and digital photographs of the integrated cascade battery/electrolyzer systems for electrolyzer (H₂ production) and batteries (mobile charging) operations [241]. Copyright © 2021 American Chemical Society.

Table 2. The bifunctional performances of LDHs-based materials in alkaline medium.

Catalysts	$E_{1/2}/V$ @ORR	$E_{j=10}/V$ @OER	Specific Capacity/mAh g^{-1}	Power Density	Open Circuit Potential	Charge/Discharge Voltage Gap	Cycling Time	Ref.
O-NiCoFe-LDHs	0.63	260	-	-	-	-	40 h	[242]
Ag NW@NiMn-LDHs	0.75	270	-	-	-	0.77 V @ 10 mA cm ⁻²	-	[215]
Ag NP/NiRu-LDHs	0.8	210	-	-	-	-	25 h	[216]
NiFe-LDHs/NrGO	0.75	250	-	-	-	-	9.5 h	[225]
CoNi-NS/rGO	0.85	330	746	300 mW cm ⁻²	1.37 V	0.8 V @ 10 mA cm ⁻²	6 h	[221]
NiFe-LDHs/Fe-N-C	0.8	300	-	-	-	-	24 h	[243]
CoNiMn-LDHs/PPy/RGO	0.77	369	-	-	-	-	5 h	[244]
NiCo ^{III} Fe-LDHs/N-GO	0.82	320	-	-	-	-	-	[218]
LDHs-POF	0.8	250	807	185 mW cm ⁻²	-	0.74 V @ 5 mA cm ⁻²	2400 cycles	[230]
NiFe-LDHs/Co,N-CNF	0.79	312	-	-	-	1 V @ 25 mA cm ⁻²	80 h	[220]
CoNC@LDHs	0.84	240	743	173 mW cm ⁻²	1.22 V	0.67 V @ 10 mA cm ⁻²	3600 cycles	[231]
Co ₃ O ₄ @NiFe-LDHs	-	226	667.5	798 Wh kg ⁻¹	1.38 V	0.8 V @ 15 mA cm ⁻²	2000 h	[245]
MnO ₂ -NiFe/Ni	0.81	226	-	94 mW cm ⁻²	-	0.98 V @ 50 mA cm ⁻²	25 h	[217]
CoFe@NC/CC	0.75	254	-	154 mW cm ⁻²	1.469 V	0.77 V @ 10 mA cm ⁻²	42 h	[246]
IE-SAC(PA+MA)	0.851	349	690.3	963 Wh kg ⁻¹	1.38 V	0.57 V @ 1 mA cm ⁻²	12 h	[234]
Ni ₃ FeN	0.78	355	-	-	1.547 V	0.7 V @ 10 mA cm ⁻²	100 h	[235]
Ni ₃ FeN/Co,N-CNF	0.81	270	-	200 mW cm ⁻²	1.43 V	0.79 V @ 6 mA cm ⁻²	540 h	[239]
Co ₃ FeS _{1.5} (OH) ₆	0.721	358	898	113 mW cm ⁻²	-	0.86 V @ 20 mA cm ⁻²	36 h	[240]
Co ₃ O ₄ -doped Co/CoFe	0.82	370	757	942 Wh kg ⁻¹	1.43 V	0.65 V @ 5 mA cm ⁻²	65 h	[90]
Co-CoO _x /N-C	0.75	278	-	21 mW cm ⁻²	1.32 V	-	11 h	[247]

5. Conclusions and Perspectives

LDHs-based materials have shown great potential in the alkaline electrocatalytic ORR and OER. This review summarizes the latest developments in transition metal-based LDHs electrocatalysts, focusing on NiFe-, CoFe-, CoNiFe-, and other transition metals-based electrocatalysts. The design and synthesis of electrocatalysts, activity origin analysis, functionalization strategies for boosting OER performance, catalytic mechanism as well as structure-performance and chemical-composition-performance relationships are discussed from the experimental and theoretical perspectives. The key issues for developing highly

efficient LDHs-based electrocatalysts are (i) the regulation of layer composition, to modify the coordination environment and electronic structure of active sites, improving the intrinsic activity; (ii) the interlayer–guest intercalation to enlarge basal spacing and expose more inner active sites, facilitating the electron/charge transfer and the mass diffusion; (iii) vacancy engineering (e.g., oxygen vacancy and metal vacancy) to facilitate the adsorption of reaction intermediates and improve the reaction kinetics; (iv) ultrathin nanostructure to increase the exposed numbers of active edge-sites; (v) structural/morphologic design, to achieve a desirable stability and durability; and (vi) the hybridization to enhance the electronic conductivity and provide multifunctional properties. The remarkable performances endow functionalized LDHs and their derivatives with great potential application as bifunctional ORR/OER electrocatalysts in the rechargeable zinc-air batteries, and unitized regenerative fuel cells.

Although some achievements have been made on electrocatalysts based on functionalized LDHs in oxygen electrode reactions, there are still some critical challenges to overcome, and there is much room for improving the catalytic performance, precise regulation of catalyst structure, as well as revealing the structure–performance correlation. The first challenge is to develop a scalable synthetic method. Although there are plenty of well-established synthetic methods developed in the laboratory, a facile and controllable synthesis route of LDHs-based electrocatalysts with satisfactory activity/structure–stability and performance is still limited. This is a restriction to achieve their mass-production and large-scale application. Secondly, it is difficult to identify the real active sites and explore the reaction mechanism due to the complexity of reaction intermediates and paths, as well as the evolution of active sites under real reaction conditions. The atomically resolved electron microscopy (4D-EM, STM, and HAADF-STEM) can allow the direct observation of transient morphology and structure of active sites during the reaction process. The combination of *in situ/operando* techniques, such as *operando* Raman, XRD, XPS, XAS, XANES, as well as theoretical study, e.g., DFT and DFT+U, can help deeply study the real catalytic process, the structural evolution, and the structure–performance relationship of the LDHs. The third key challenge is how to maintain the chemical and mechanical stability of LDHs-based electrodes under the industrial conditions, such as strong alkali electrolyte, high operating-temperature, and high current density. The *in situ* grown nanoarray electrode based on LDHs materials or their derivatives is significantly superior over the corresponding electrode prepared by the traditional spraying or dip-coating method. The nanoarray electrode, without the addition of the binder, shows a strong interaction between the conductive substrate (current collector) and active species, which can protect the active materials from falling off from the current collector. Moreover, the electro-deposition method would be feasible for preparing large scale nanoarray electrodes. Finally, integrating the ORR-active materials and OER-active LDHs, or designing the derivatives from LDHs precursors for bifunctional ORR/OER catalysts, is essential to the development of the URFCs and ZABs in the future. How to precisely control the composition and hierarchical structure of the bifunctional electrocatalysts? The key aspects are to rationally design and arrange the different active sites on the specific positions to avoid the competition of the ORR/OER active sites; and the occupation of the efficient positions, in a bifunctional electrocatalyst, might ensure fully the exposure to the dual-pathway of electron conduction and ion transportation in the ORR/OER multiphase electrocatalysis.

Author Contributions: J.W. searched the literature and wrote the manuscript; H.K. contributed with the data analysis; Y.J. wrote part of this work; F.G. redacted and corrected the references; N.A.-V. reviewed the work; H.Z. and Y.F. organized, supervised, and reviewed the work. All authors have read and agreed to the published version of the manuscript.

Funding: This research received no external funding.

Acknowledgments: This work is supported by National Key R&D Program of China (No. 2016YFB0301600), the National Natural Science Foundation of China (No. 21571015, 21627813), Program for Changjiang Scholars

and Innovative Research Team in University (No. IRT1205), Fundamental Research Funds for the Central Universities (No. ZY2117).

Conflicts of Interest: The authors declare no conflict of interest.

References

1. Chu, S.; Majumdar, A. Opportunities and Challenges for a Sustainable Energy Future. *Nature* **2012**, *488*, 294–303. [[CrossRef](#)] [[PubMed](#)]
2. Zhong, M.; Liu, M.; Li, N.; Bu, X.H. Recent Advances and Perspectives of Metal/Covalent-Organic Frameworks in Metal-air Batteries. *J. Energy Chem.* **2021**. [[CrossRef](#)]
3. She, L.N.; Zhao, G.Q.; Ma, T.Y.; Chen, J.; Sun, W.P.; Pan, H.G. On the Durability of Iridium-based Electrocatalysts toward the Oxygen Evolution Reaction under Acid Environment. *Adv. Funct. Mater.* **2021**. [[CrossRef](#)]
4. Jiang, N.; Zhu, Z.W.; Xue, W.J.; Xia, B.Y.; You, B. Emerging Electrocatalysts for Water Oxidation under Near-neutral CO₂ Reduction Conditions. *Adv. Mater.* **2021**. [[CrossRef](#)] [[PubMed](#)]
5. Abdul Nasir, J.; Munir, A.; Ahmad, N.; Haq, T.u.; Khan, Z.; Rehman, Z. Photocatalytic Z-scheme Overall Water Splitting: Recent Advances in Theory and Experiments. *Adv. Mater.* **2021**. [[CrossRef](#)] [[PubMed](#)]
6. Lyons, M.E.G.; Doyle, R.L.; Fernandez, D.; Godwin, I.J.; Browne, M.P.; Rovetta, A. The Mechanism and Kinetics of Electrochemical Water Oxidation at Oxidized Metal and Metal Oxide Electrodes. Part 1. General Considerations: A Mini Review. *Electrochem. Commun.* **2014**, *45*, 60–62. [[CrossRef](#)]
7. Tributsch, H. Photovoltaic Hydrogen Generation. *Int. J. Hydrogen Energy* **2008**, *33*, 5911–5930. [[CrossRef](#)]
8. Zeng, K.; Zhang, D.K. Recent Progress in Alkaline Water Electrolysis for Hydrogen Production and Applications. *Prog. Energy Combust. Sci.* **2010**, *36*, 307–326. [[CrossRef](#)]
9. Debe, M.K. Electrocatalyst Approaches and Challenges for Automotive Fuel Cells. *Nature* **2012**, *486*, 43–51. [[CrossRef](#)]
10. Jiao, Y.; Zheng, Y.; Jaroniec, M.; Qiao, S.Z. Design of Electrocatalysts for Oxygen- and Hydrogen-involving Energy Conversion Reactions. *Chem. Soc. Rev.* **2015**, *44*, 2060–2086. [[CrossRef](#)]
11. Peng, P.; Zhou, Z.H.; Guo, J.N.; Xiang, Z.H. Well-defined 2D Covalent Organic Polymers for Energy Electrocatalysis. *ACS Energy Lett.* **2017**, *2*, 1308–1314. [[CrossRef](#)]
12. Stamenkovic, V.R.; Strmcnik, D.; Lopes, P.P.; Markovic, N.M. Energy and Fuels from Electrochemical Interfaces. *Nat. Mater.* **2016**, *16*, 57–69. [[CrossRef](#)]
13. Zhao, X.Y.; Yang, Y.; Li, Y.H.; Cui, X.; Zhang, Y.H.; Xiao, P. NiCo-selenide as a Novel Catalyst for Water Oxidation. *J. Mater. Sci.* **2016**, *51*, 3724–3734. [[CrossRef](#)]
14. Song, J.J.; Wei, C.; Huang, Z.F.; Liu, C.T.; Zeng, L.; Wang, X.; Xu, Z.C. A Review on Fundamentals for Designing Oxygen Evolution Electrocatalysts. *Chem. Soc. Rev.* **2020**, *49*, 2196–2214. [[CrossRef](#)]
15. Tang, C.; Wang, H.F.; Zhang, Q. Multiscale Principles to Boost Reactivity in Gas-involving Energy Electrocatalysis. *Acc. Chem. Res.* **2018**, *51*, 881–889. [[CrossRef](#)] [[PubMed](#)]
16. Lee, Y.M.; Suntivich, J.; May, K.J.; Perry, E.E.; Shao-Horn, Y. Synthesis and Activities of Rutile IrO₂ and RuO₂ Nanoparticles for Oxygen Evolution in Acid and Alkaline Solutions. *J. Phys. Chem. Lett.* **2012**, *3*, 399–404. [[CrossRef](#)] [[PubMed](#)]
17. Audichon, T.; Napporn, T.W.; Canaff, C.; Morais, C.; Comminges, C.; Kokoh, K.B. IrO₂ Coated on RuO₂ as Efficient and Stable Electroactive Nanocatalysts for Electrochemical Water Splitting. *J. Phys. Chem. C* **2016**, *120*, 2562–2573. [[CrossRef](#)]
18. DeSario, P.A.; Chervin, C.N.; Nelson, E.S.; Sassin, M.B.; Rolison, D.R. Competitive Oxygen Evolution in Acid Electrolyte Catalyzed at Technologically Relevant Electrodes Painted with Nanoscale RuO₂. *ACS Appl. Mater. Interfaces* **2017**, *9*, 2387–2395. [[CrossRef](#)] [[PubMed](#)]
19. Cherevko, S.; Geiger, S.; Kasian, O.; Kulyk, N.; Grote, J.P.; Sava, A.; Shrestha, B.R.; Merzlikin, S.; Breitbach, B.; Ludwig, A.; et al. Oxygen and Hydrogen Evolution Reactions on Ru, RuO₂, Ir, and IrO₂ Thin Film Electrodes in Acidic and Alkaline Electrolytes: A Comparative Study on Activity and Stability. *Catal. Today* **2016**, *262*, 170–180. [[CrossRef](#)]
20. Antolini, E. Iridium as Catalyst and Cocatalyst for Oxygen Evolution/Reduction in Acidic Polymer Electrolyte Membrane Electrolyzers and Fuel Cells. *ACS Catal.* **2014**, *4*, 1426–1440. [[CrossRef](#)]
21. Tahir, M.; Pan, L.; Idrees, F.; Zhang, X.W.; Wang, L.; Zou, J.J.; Wang, Z.L. Electrocatalytic Oxygen Evolution Reaction for Energy Conversion and Storage: A Comprehensive Review. *Nano Energy* **2017**, *37*, 136–157. [[CrossRef](#)]
22. Jung, S.H.; McCrory, C.C.L.; Ferrer, I.M.; Peters, J.C.; Jaramillo, T.F. Benchmarking Nanoparticulate Metal Oxide Electrocatalysts for the Alkaline Water Oxidation Reaction. *J. Mater. Chem. A* **2016**, *4*, 3068–3076. [[CrossRef](#)]
23. Kuai, L.; Geng, J.; Chen, C.Y.; Kan, E.J.; Liu, Y.D.; Wang, Q.; Geng, B.Y. A Reliable Aerosol-spray-assisted Approach to Produce and Optimize Amorphous Metal Oxide Catalysts for Electrochemical Water Splitting. *Angew. Chem. Int. Ed. Engl.* **2014**, *126*, 7677–7681. [[CrossRef](#)]
24. Gao, R.q.; Deng, M.; Yan, Q.; Fang, Z.X.; Li, L.C.; Shen, H.Y.; Chen, Z.F. Structural Variations of Metal Oxide-based Electrocatalysts for Oxygen Evolution Reaction. *Small Methods* **2021**. [[CrossRef](#)]
25. Abrham Gebreslase, G.; Victoria Martínez-Huerta, M.; Jesus Lázaro, M. Recent Progress on Bimetallic NiCo and CoFe based Electrocatalysts for Alkaline Oxygen Evolution Reaction: A Review. *J. Energy Chem.* **2021**. [[CrossRef](#)]
26. Wang, H.X.; Zhang, K.H.L.; Hofmann, J.P.; de la Peña O’Shea, V.A.; Oropeza, F.E. The Electronic Structure of Transition Metal Oxides for Oxygen Evolution Reaction. *J. Mater. Chem. A* **2021**, *9*, 19465–19488. [[CrossRef](#)]

27. Yu, M.Q.; Budiayanto, E.; Tüysüz, H.R. Principles of Water Electrolysis and Recent Progress in Cobalt-, Nickel-, and Iron-based Oxides for the Oxygen Evolution Reaction. *Angew. Chem. Int. Ed.* **2021**. [[CrossRef](#)]
28. Tang, Y.J.; Zheng, S.S.; Cao, S.; Xue, H.G.; Pang, H. Advances in the Application of Manganese Dioxide and its Composites as Electrocatalysts for the Oxygen Evolution Reaction. *J. Mater. Chem. A* **2020**, *8*, 18492–18514. [[CrossRef](#)]
29. Tian, L.; Zhai, X.H.; Wang, X.; Li, J.; Li, Z. Advances in Manganese-based Oxides for Oxygen Evolution Reaction. *J. Mater. Chem. A* **2020**, *8*, 14400–14414. [[CrossRef](#)]
30. Burke, M.S.; Enman, L.J.; Batchellor, A.S.; Zou, S.H.; Boettcher, S.W. Oxygen Evolution Reaction Electrocatalysis on Transition Metal Oxides and (Oxy)Hydroxides: Activity Trends and Design Principles. *Chem. Mater.* **2015**, *27*, 7549–7558. [[CrossRef](#)]
31. Tang, C.; Wang, H.F.; Wang, H.S.; Wei, F.; Zhang, Q. Guest-host Modulation of Multi-metallic (Oxy) Hydroxides for Superb Water Oxidation. *J. Mater. Chem. A* **2016**, *4*, 3210–3216. [[CrossRef](#)]
32. Zhang, X.; Yi, H.; An, Q.; Song, S.X. Recent Advances in Engineering Cobalt Carbonate Hydroxide for Enhanced Alkaline Water Splitting. *J. Alloys Compd.* **2021**, *887*, 161405. [[CrossRef](#)]
33. Zhang, S.Q.; Yu, T.; Wen, H.; Ni, Z.Y.; He, Y.; Guo, R.; You, J.H.; Liu, X.W. The Latest Development of CoOOH Two-dimensional Materials used as OER Catalysts. *Chem. Commun.* **2020**, *56*, 15387–15405. [[CrossRef](#)]
34. Zhang, J.; Si, C.H.; Kou, T.Y.; Wang, J.F.; Zhang, Z.H. Recent Progress in Self-supported Two-dimensional Transition Metal Oxides and (Oxy)Hydroxides as Oxygen Evolution Reaction Catalysts. *Sustain. Energy Fuels* **2020**, *4*, 2625–2637. [[CrossRef](#)]
35. Lei, L.; Huang, D.L.; Zhou, C.Y.; Chen, S.; Yan, X.L.; Li, Z.H.; Wang, W.J. Demystifying the Active Roles of NiFe-based Oxides/(Oxy)Hydroxides for Electrochemical Water Splitting under Alkaline Conditions. *Coord. Chem. Rev.* **2020**, *408*, 213177. [[CrossRef](#)]
36. He, P.L.; Yu, X.Y.; Lou, X.W. Carbon-incorporated Nickel-Cobalt Mixed Metal Phosphide Nanoboxes with Enhanced Electrocatalytic Activity for Oxygen Evolution. *Angew. Chem. Int. Ed. Engl.* **2017**, *56*, 3897–3900. [[CrossRef](#)] [[PubMed](#)]
37. Hu, E.L.; Feng, Y.F.; Nai, J.W.; Zhao, D.; Hu, Y.; Lou, X.W. Construction of Hierarchical Ni-Co-P Hollow Nanobricks with Oriented Nanosheets for Efficient Overall Water Splitting. *Energy Environ. Sci.* **2018**, *11*, 872–880. [[CrossRef](#)]
38. Zhao, H.; Yuan, Z.Y. Transition Metal-phosphorus-based Materials for Electrocatalytic Energy Conversion Reactions. *Catal. Sci. Technol.* **2017**, *7*, 330–347. [[CrossRef](#)]
39. Zhao, X.D.; Kong, X.L.; Liu, Z.L.; Li, Z.; Xie, Z.W.; Wu, Z.Y.; He, F.; Chang, X.H.; Yang, P.P.; Zheng, J.; et al. The Cutting-edge Phosphorus-rich Metal Phosphides for Energy Storage and Conversion. *Nano Today* **2021**, *40*, 101245. [[CrossRef](#)]
40. Li, Z.; Feng, H.; Song, M.; He, C.; Zhuang, W.; Tian, L. Advances in CoP Electrocatalysts for Water Splitting. *Mater. Today Energy* **2021**, *20*, 100698. [[CrossRef](#)]
41. Ray, A.; Sultana, S.; Paramanik, L.; Parida, K.M. Recent Advances in Phase, Size, and Morphology-oriented Nanostructured Nickel Phosphide for Overall Water Splitting. *J. Mater. Chem. A* **2020**, *8*, 19196–19245. [[CrossRef](#)]
42. Pu, Z.H.; Liu, T.T.; Amiin, I.S.; Cheng, R.L.; Wang, P.Y.; Zhang, C.T.; Ji, P.X.; Hu, W.H.; Liu, J.; Mu, S.C. Transition-metal Phosphides: Activity Origin, Energy-related Electrocatalysis Applications, and Synthetic Strategies. *Adv. Funct. Mater.* **2020**, *30*, 2004009. [[CrossRef](#)]
43. Liu, Y.W.; Xiao, C.; Lyu, M.J.; Lin, Y.; Cai, W.Z.; Huang, P.C.; Tong, W.; Zou, Y.M.; Xie, Y. Ultrathin Co₃S₄ Nanosheets that Synergistically Engineer Spin States and Exposed Polyhedra that Promote Water Oxidation under Neutral Conditions. *Angew. Chem. Int. Ed. Engl.* **2015**, *54*, 11231–11235. [[CrossRef](#)] [[PubMed](#)]
44. Liu, H.J.; He, Q.; Jiang, H.L.; Lin, Y.X.; Zhang, Y.K.; Habib, M.; Chen, S.M.; Song, L. Electronic Structure Reconfiguration toward Pyrite NiS₂ via Engineered Heteroatom Defect Boosting Overall Water Splitting. *ACS Nano* **2017**, *11*, 11574–11583. [[CrossRef](#)]
45. Wang, X.; Zhuang, L.Z.; Jia, Y.; Liu, H.L.; Yan, X.C.; Zhang, L.Z.; Yang, D.J.; Zhu, Z.H.; Yao, X.D. Plasma-triggered Synergy of Exfoliation, Phase Transformation, and Surface Engineering in Cobalt Diselenide for Enhanced Water Oxidation. *Angew. Chem. Int. Ed. Engl.* **2018**, *57*, 16421–16425. [[CrossRef](#)]
46. Zhao, Y.; You, J.H.; Wang, L.; Bao, W.T.; Yao, R.Y. Recent Advances in Ni₃S₂-based Electrocatalysts for Oxygen Evolution Reaction. *Int. J. Hydrogen Energy* **2021**, *46*, 39146–39182. [[CrossRef](#)]
47. Li, Y.Q.; Yin, Z.H.; Cui, M.; Liu, X.; Xiong, J.B.; Chen, S.R.; Ma, T.L. Interface Engineering of Transitional Metal Sulfide-MoS₂ Heterostructure Composites as Effective Electrocatalysts for Water-splitting. *J. Mater. Chem. A* **2021**, *9*, 2070–2092. [[CrossRef](#)]
48. Ni, Z.Y.; Wen, H.; Zhang, S.Q.; Guo, R.; Su, N.; Liu, X.W.; Liu, C.M. Recent Advances in Layered Tungsten Disulfide as Electrocatalyst for Water Splitting. *ChemCatChem* **2020**, *12*, 4962–4999. [[CrossRef](#)]
49. Wang, Y.Y.; Qiao, M.; Li, Y.F.; Wang, S.Y. Tuning Surface Electronic Configuration of NiFe LDHs Nanosheets by Introducing Cation Vacancies (Fe or Ni) as Highly Efficient Electrocatalysts for Oxygen Evolution Reaction. *Small* **2018**, *14*, 1800136. [[CrossRef](#)]
50. Zhou, D.J.; Li, P.S.; Lin, X.; McKinley, A.; Kuang, Y.; Liu, W.; Lin, W.F.; Sun, X.M.; Duan, X. Layered Double Hydroxide-based Electrocatalysts for the Oxygen Evolution Reaction: Identification and Tailoring of Active Sites, and Superaerophobic Nanoarray Electrode assembly. *Chem. Soc. Rev.* **2021**, *50*, 8790–8817. [[CrossRef](#)]
51. Gicha, B.B.; Tufa, L.T.; Kang, S.; Goddati, M.; Bekele, E.T.; Lee, J. Transition Metal-based 2D Layered Double Hydroxide Nanosheets: Design Strategies and Applications in Oxygen Evolution Reaction. *Nanomaterials* **2021**, *11*, 1388. [[CrossRef](#)]
52. Yu, J.; Yu, F.; Yuen, M.F.; Wang, C.D. Two-dimensional Layered Double Hydroxides as a Platform for Electrocatalytic Oxygen Evolution. *J. Mater. Chem. A* **2021**, *9*, 9389–9430. [[CrossRef](#)]
53. Yang, L.; Liu, Z.; Zhu, S.; Feng, L.; Xing, W. Ni-based Layered Double Hydroxide Catalysts for Oxygen Evolution Reaction. *Mater. Today Phys.* **2021**, *16*, 100292. [[CrossRef](#)]

54. Bodhankar, P.M.; Sarawade, P.B.; Singh, G.; Vinu, A.; Dhawale, D.S. Recent Advances in Highly Active Nanostructured NiFe LDH Catalyst for Electrochemical Water Splitting. *J. Mater. Chem. A* **2020**, *9*, 3180–3208. [[CrossRef](#)]
55. Karmakar, A.; Karthick, K.; Sankar, S.S.; Kumaravel, S.; Madhu, R.; Kundu, S. A Vast Exploration of Improvising Synthetic Strategies for Enhancing the OER Kinetics of LDH Structures: A Review. *J. Mater. Chem. A* **2020**, *9*, 1314–1352. [[CrossRef](#)]
56. Goncalves, J.M.; Martins, P.R.; Angnes, L.; Araki, K. Recent Advances in Ternary Layered Double Hydroxide Electrocatalysts for the Oxygen Evolution Reaction. *New J. Chem.* **2020**, *44*, 9981–9997. [[CrossRef](#)]
57. Hall, D.E. Ni(OH)₂-impregnated Anodes for Alkaline Water Electrolysis. *J. Electrochem. Soc.* **1983**, *130*, 317–321. [[CrossRef](#)]
58. Klaus, S.; Cai, Y.; Louie, M.W.; Trotochaud, L.; Bell, A.T. Effects of Fe Electrolyte Impurities on Ni(OH)₂/NiOOH Structure and Oxygen Evolution Activity. *J. Phys. Chem. C* **2015**, *119*, 7243–7254. [[CrossRef](#)]
59. Song, Y.H.; Song, M.X.; Liu, P.Z.; Liu, W.W.; Yuan, L.J.; Hao, X.D.; Pei, L.Y.; Xu, B.S.; Guo, J.J.; Sun, Z.Q. Fe-doping Induced Localized Amorphization in Ultrathin α -Ni(OH)₂ Nanomesh for Superior Oxygen Evolution Reaction Catalysis. *J. Mater. Chem. A* **2021**, *9*, 14372–14380. [[CrossRef](#)]
60. Zhong, H.H.; Cheng, X.K.; Xu, H.T.; Li, L.; Li, D.Q.; Tang, P.G.; Alonso-Vante, N.; Feng, Y.J. Carbon Fiber Paper Supported Interlayer Space Enlarged Ni₂Fe-LDHs Improved OER Electrocatalytic Activity. *Electrochim. Acta* **2017**, *258*, 554–560. [[CrossRef](#)]
61. Ye, Q.L.; Li, L.F.; Li, H.Y.; Gu, X.Y.; Han, B.M.; Xu, X.T.; Wang, F.; Li, B. Quasi-parallel NiFe Layered Double Hydroxide Nanosheet Arrays for Large-current-density Oxygen Evolution Electrocatalysis. *ChemSusChem* **2021**. [[CrossRef](#)]
62. Wilhelm, M.; Bastos, A.; Neves, C.; Martins, R.; Tedim, J. Ni-Fe Layered Double Hydroxides for Oxygen Evolution Reaction: Impact of Ni/Fe Ratio and Crystallinity. *Mater. Des.* **2021**, *212*, 110188. [[CrossRef](#)]
63. Dong, G.F.; Xie, F.Y.; Kou, F.X.; Chen, T.T.; Wang, F.Y.; Zhou, Y.W.; Wu, K.C.; Du, S.W.; Fang, M.; Ho, J.C. NiFe-Layered Double Hydroxides Arrays for Oxygen Evolution Reaction in Fresh Water and Seawater. *Mater. Today Energy* **2021**. [[CrossRef](#)]
64. Chen, W.; Wu, B.B.; Wang, Y.Y.; Zhou, W.; Li, Y.Y.; Liu, T.Y.; Xie, C.; Xu, L.T.; Du, S.Q.; Song, M.L.; et al. Deciphering the Alternating Synergy Between Interlayer Pt Single-atom and NiFe Layered Double Hydroxide for Overall Water Splitting. *Energy Environ. Sci.* **2021**. [[CrossRef](#)]
65. Liu, B.Y.; Zhang, M.; Wang, Y.C.; Chen, Z.; Yan, K. Facile Synthesis of Defect-rich Ultrathin NiCo-LDHs, NiMn-LDHs and NiCoMn-LDHs Nanosheets on Ni Foam for Enhanced Oxygen Evolution Reaction Performance. *J. Alloys Compd.* **2021**, *852*, 156949. [[CrossRef](#)]
66. Chen, Z.D.; Zhang, Y.; Yang, P.G.; Xiong, W.; Ren, X.Z.; Li, Y.L.; Wang, L.L.; Ye, S.H.; Liu, J.H.; Zhang, Q.L. Improving Oxygen Evolution Reaction Activity by Constructing Core-shell Structure of Co/N-doped Carbon Polyhedron@NiCo Layered Double Hydroxides. *J. Alloys Compd.* **2022**, *890*, 161805. [[CrossRef](#)]
67. Shamloofard, M.; Shahrokhian, S.; Amini, M.K. Mesoporous Nanostructures of NiCo-LDH/ZnCo₂O₄ as an Efficient Electrocatalyst for Oxygen Evolution Reaction. *J. Colloid Interface Sci.* **2021**, *604*, 832–843. [[CrossRef](#)] [[PubMed](#)]
68. Chu, B.X.; Ma, Q.X.; Li, Z.S.; Li, B.L.; Huang, F.R.; Pang, Q.; Chen, Y.B.; Li, B.; Zhang, J.Z. Design and Preparation of Three-dimensional Hetero-electrocatalysts of NiCo-Layered Double Hydroxide Nanosheets Incorporated with Silver Nanoclusters for Enhanced Oxygen Evolution Reactions. *Nanoscale* **2021**, *13*, 11150–11160. [[CrossRef](#)]
69. Feng, Y.Q.; Wang, X.; Huang, J.F.; Dong, P.P.; Ji, J.; Li, J.; Cao, L.Y.; Feng, L.L.; Jin, P.; Wang, C.R. Decorating CoNi Layered Double Hydroxides Nanosheet Arrays with Fullerene Quantum Dot Anchored on Ni Foam for Efficient Electrocatalytic Water Splitting and Urea Electrolysis. *Chem. Eng. J.* **2020**, *390*, 124525. [[CrossRef](#)]
70. Shi, Y.L.; Li, J.Q.; Zhang, B.Y.; Lv, S.Y.; Wang, T.; Liu, X. Tuning Electronic Structure of CoNi LDHs via Surface Fe Doping for Achieving Effective Oxygen Evolution Reaction. *Appl. Surf. Sci.* **2021**, *565*, 150506. [[CrossRef](#)]
71. Hu, L.Y.; Li, M.Y.; Wei, X.Q.; Wang, H.J.; Wu, Y.; Wen, J.; Gu, W.L.; Zhu, C.Z. Modulating Interfacial Electronic Structure of CoNi LDH Nanosheets with Ti₃C₂T_x MXene for Enhancing Water Oxidation Catalysis. *Chem. Eng. J.* **2020**, *398*, 125605. [[CrossRef](#)]
72. Li, J.W.; Lian, R.Q.; Wang, J.Y.; He, S.; Jiang, S.P.; Rui, Z.B. Oxygen Vacancy Defects Modulated Electrocatalytic Activity of Iron-Nickel Layered Double Hydroxide on Ni Foam as Highly Active Electrodes for Oxygen Evolution Reaction. *Electrochim. Acta* **2020**, *331*, 135395. [[CrossRef](#)]
73. Wang, M.; Wei, Y.S.; Zou, L.L.; Wang, H.F.; Shen, S.H.; Xu, Q. Revealing Active Function of Multicomponent Electrocatalysts from In Situ Nickel Redox for Oxygen Evolution. *J. Phys. Chem. Lett.* **2021**, *125*, 16420–16427. [[CrossRef](#)]
74. Zheng, F.Q.; Zhang, W.F.; Zhang, X.X.; Zhang, Y.L.; Chen, W. Sub-2 nm Ultrathin and Robust 2D FeNi Layered Double Hydroxide Nanosheets Packed with 1D FeNi-MOFs for Enhanced Oxygen Evolution Electrocatalysis. *Adv. Funct. Mater.* **2021**, *31*, 2103318. [[CrossRef](#)]
75. Han, X.Q.; Lin, Z.H.; He, X.Q.; Cui, L.L.; Lu, D.X. The Construction of Defective FeCo-LDHs by In-situ Polyaniline Curved Strategy as a Desirable Bifunctional Electrocatalyst for OER and HER. *Int. J. Hydrogen Energy* **2020**, *45*, 26989–26999. [[CrossRef](#)]
76. Deng, L.Q.; Zhang, K.; Shi, D.; Liu, S.F.; Xu, D.Q.; Shao, Y.L.; Shen, J.X.; Wu, Y.Z.; Hao, X.P. Rational Design of Schottky Heterojunction with Modulating Surface Electron Density for High-performance Overall Water Splitting. *Appl. Catal. B Environ.* **2021**, *299*, 120660. [[CrossRef](#)]
77. Hu, L.Y.; Xiao, R.S.; Wang, X.; Wang, X.S.; Wang, C.L.; Wen, J.; Gu, W.L.; Zhu, C.Z. MXene-induced Electronic Optimization of Metal-Organic Framework-derived CoFe LDH Nanosheet Arrays for Efficient Oxygen Evolution. *Appl. Catal. B Environ.* **2021**, *298*, 120599. [[CrossRef](#)]
78. Wu, L.B.; Yu, L.; Zhu, Q.C.; McElhenny, B.; Zhang, F.H.; Wu, C.Z.; Xing, X.X.; Bao, J.M.; Chen, S.; Ren, Z.F. Boron-modified Cobalt Iron Layered Double Hydroxides for High Efficiency Seawater Oxidation. *Nano Energy* **2021**, *83*, 105838. [[CrossRef](#)]

79. Chen, L.Y.; Guo, Y.T.; Wang, H.F.; Gu, Z.Z.; Zhang, Y.Y.; Li, X.Z.; Wang, H.; Duan, C.Y. Imidazolate-mediated Assembled Structures of Co-LDH Sheets for Efficient Electrocatalytic Oxygen Evolution. *J. Mater. Chem. A* **2018**, *6*, 4636–4641. [[CrossRef](#)]
80. Xu, X.; Cao, A.H.; You, W.F.; Tao, Z.J.; Kang, L.T.; Liu, J.J. Assembly of Cobalt Layered Double Hydroxide on Cuprous Phosphide Nanowire with Strong Built-in Potential for Accelerated Overall Water Splitting. *Small* **2021**, *17*, 2101725. [[CrossRef](#)]
81. Zhang, M.L.; Zhang, Y.Q.; Ye, L.; Guo, B.W.; Gong, Y.Q. Hierarchically Constructed Ag Nanowires Shelled with Ultrathin Co-LDH Nanosheets for Advanced Oxygen Evolution Reaction. *Appl. Catal. B Environ.* **2021**, *298*, 120601. [[CrossRef](#)]
82. Chen, Q.; Ding, R.; Liu, H.; Zhou, L.X.; Wang, Y.; Zhang, Y.; Fan, G.Y. Flexible Active-site Engineering of Monometallic Co-Layered Double Hydroxides for Achieving High-performance Bifunctional Electrocatalyst toward Oxygen Evolution and H₂O₂ Reduction. *ACS Appl. Mater. Interfaces* **2020**, *12*, 12919–12929. [[CrossRef](#)]
83. Zhang, G.Q.; Li, Y.F.; Zhou, Y.F.; Yang, F.L. NiFe Layered-double-hydroxide-derived NiO-NiFe₂O₄/Reduced Graphene Oxide Architectures for Enhanced Electrocatalysis of Alkaline Water Splitting. *ChemElectroChem* **2016**, *3*, 1927–1936. [[CrossRef](#)]
84. Zhong, H.Z.; Gao, G.P.; Wang, X.N.; Wu, H.Y.; Shen, S.H.; Zuo, W.B.; Cai, G.X.; Wei, G.; Shi, Y.; Fu, D.J.; et al. Ion Irradiation Inducing Oxygen Vacancy-rich NiO/NiFe₂O₄ Heterostructure for Enhanced Electrocatalytic Water Splitting. *Small* **2021**, *17*, 2103501. [[CrossRef](#)]
85. Fan, X.M.; Ma, Y.X.; Sun, A.K.; Zhang, X.; Tang, L.; Guo, J.X. Engineering Heterogeneous Nickel-Iron Oxide/Iron Phosphate on P, N co-doped Carbon Fibers for Efficient Oxygen Evolution Reaction in Neutral and Alkaline Solutions. *Surf. Interfaces* **2021**, *25*, 101193. [[CrossRef](#)]
86. Zhong, H.H.; Tian, R.; Li, D.Q.; Tang, P.G.; Alonso-Vante, N.; Feng, Y.J. Tuning the Adsorption Properties of Layered Double Hydroxides to Tailor Highly Active Oxygen Bifunctional Electrocatalysts. *J. Electrochem. Soc.* **2017**, *164*, F491–F498. [[CrossRef](#)]
87. Ortega, K.F.; Anke, S.; Salamon, S.; Ozcan, F.; Heese, J.; Andronescu, C.; Landers, J.; Wende, H.; Schuhmann, W.; Muhler, M.; et al. Topotactic Synthesis of Porous Cobalt Ferrite Platelets from a Layered Double Hydroxide Precursor and Their Application in Oxidation Catalysis. *Chem. Eur. J.* **2017**, *23*, 12443–12449. [[CrossRef](#)] [[PubMed](#)]
88. Li, J.; Lu, S.Q.; Huang, H.L.; Liu, D.H.; Zhuang, Z.B.; Zhong, C.L. ZIF-67 as Continuous Self-sacrifice Template Derived NiCo₂O₄/Co,N-CNTs Nanocages as Efficient Bifunctional Electrocatalysts for Rechargeable Zn-air Batteries. *ACS Sustain. Chem. Eng.* **2018**, *6*, 10021–10029. [[CrossRef](#)]
89. Yang, M.; Lu, W.; Jin, R.X.; Liu, X.C.; Song, S.Y.; Xing, Y. Superior Oxygen Evolution Reaction Performance of Co₃O₄/NiCo₂O₄/Ni Foam Composite with Hierarchical Structure. *ACS Sustain. Chem. Eng.* **2019**, *7*, 12214–12221. [[CrossRef](#)]
90. Li, T.T.; Lu, Y.X.; Zhao, S.S.; Gao, Z.D.; Song, Y.Y. Co₃O₄-doped Co/CoFe Nanoparticles Encapsulated in Carbon Shells as Bifunctional Electrocatalysts for Rechargeable Zn-air Batteries. *J. Mater. Chem. A* **2018**, *6*, 3730–3737. [[CrossRef](#)]
91. Peng, D.D.; Zhang, B.W.; Wu, J.S.; Huang, K.; Cao, X.; Lu, Y.; Zhang, Y.; Li, C.J.; Huang, Y.Z. Growth of Lattice Coherent Co₉S₈/Co₃O₄ Nano-heterostructure for Maximizing the Catalysis of Co-based Composites. *ChemCatChem* **2020**, *12*, 2431–2435. [[CrossRef](#)]
92. He, C.Y.; Han, X.Z.; Kong, X.G.; Jiang, M.H.; Lei, D.Q.; Lei, X.D. Fe-doped Co₃O₄@C Nanoparticles Derived from Layered Double Hydroxide used as Efficient Electrocatalyst for Oxygen Evolution Reaction. *J. Energy Chem.* **2019**, *32*, 63–70. [[CrossRef](#)]
93. Anantharaj, S.; Karthick, K.; Kundu, S. Evolution of Layered Double Hydroxides (LDH) as High Performance Water Oxidation Electrocatalysts: A Review with Insights on Structure, Activity and Mechanism. *Mater. Today Energy* **2017**, *6*, 1–26. [[CrossRef](#)]
94. Varadwaj, G.B.B.; Nyamori, V.O. Layered Double Hydroxide- and Graphene-based Hierarchical Nanocomposites: Synthetic Strategies and Promising Applications in Energy Conversion and Conservation. *Nano Res.* **2016**, *9*, 3598–3621. [[CrossRef](#)]
95. Gong, M.; Dai, H.J. A Mini Review of NiFe-based Materials as Highly Active Oxygen Evolution Reaction Electrocatalysts. *Nano Res.* **2015**, *8*, 23–39. [[CrossRef](#)]
96. Patel, R.; Park, J.T.; Patel, M.; Dash, J.K.; Gowd, E.B.; Karpoomath, R.; Mishra, A.; Kwak, J.; Kim, J.H. Transition-metal-based Layered Double Hydroxides Tailored for Energy Conversion and Storage. *J. Mater. Chem. A* **2018**, *6*, 12–29. [[CrossRef](#)]
97. Laipan, M.W.; Yu, J.F.; Zhu, R.L.; Zhu, J.X.; Smith, A.T.; He, H.P.; O'Hare, D.; Sun, L.Y. Functionalized Layered Double Hydroxides for Innovative Applications. *Mater. Horiz.* **2020**, *7*, 715–745. [[CrossRef](#)]
98. Yu, J.F.; Wang, Q.; O'Hare, D.; Sun, L.Y. Preparation of Two Dimensional Layered Double Hydroxide Nanosheets and Their Applications. *Chem. Soc. Rev.* **2017**, *46*, 5950–5974. [[CrossRef](#)]
99. Li, C.M.; Wei, M.; Evans, D.G.; Duan, X. Recent Advances for Layered Double Hydroxides (LDHs) Materials as Catalysts Applied in Green Aqueous Media. *Catal. Today* **2015**, *247*, 163–169. [[CrossRef](#)]
100. Li, T.F.; Miras, H.N.; Song, Y.F. Polyoxometalate (POM)-Layered Double Hydroxides (LDH) Composite Materials: Design and Catalytic Applications. *Catalysts* **2017**, *7*, 260. [[CrossRef](#)]
101. Liu, Y.; Gao, Y.S.; Wang, Q.; Lin, W.R. The Synergistic Effect of Layered Double Hydroxides with Other Flame Retardant Additives for Polymer Nanocomposites: A Critical Review. *Dalton Trans.* **2018**, *47*, 14827–14840. [[CrossRef](#)]
102. Guo, L.; Wu, W.; Zhou, Y.F.; Zhang, F.; Zeng, R.C.; Zeng, J.M. Layered Double Hydroxide Coatings on Magnesium Alloys: A Review. *J. Mater. Sci. Technol.* **2018**, *34*, 1455–1466. [[CrossRef](#)]
103. Bouali, A.C.; Serdechnova, M.; Blawert, C.; Tedim, J.; Ferreira, M.G.S.; Zheludkevich, M.L. Layered Double Hydroxides (LDHs) as Functional Materials for the Corrosion Protection of Aluminum Alloys: A Review. *Appl. Mater. Today* **2020**, *21*, 100857. [[CrossRef](#)]
104. Dewangan, N.; Hui, W.M.; Jayaprakash, S.; Bawah, A.R.; Poerjoto, A.J.; Jie, T.; Jangam, A.; Hidajat, K.; Kawi, S. Recent Progress on Layered Double Hydroxide (LDH) Derived Metal-based Catalysts for CO₂ Conversion to Valuable Chemicals. *Catal. Today* **2020**, *356*, 490–513. [[CrossRef](#)]

105. Boumeriame, H.; Da Silva, E.S.; Cherevan, A.S.; Chafik, T.; Faria, J.L.; Eder, D. Layered Double Hydroxide (LDH)-based Materials: A Mini-review on Strategies to Improve the Performance for Photocatalytic Water Splitting. *J. Energy Chem.* **2022**, *64*, 406–431. [[CrossRef](#)]
106. Li, S.D.; Wang, D.D.; Wu, X.F.; Chen, Y.F. Recent Advance on VOCs Oxidation Over Layered Double Hydroxides Derived Mixed Metal Oxides. *Chin. J. Catal.* **2020**, *41*, 550–560. [[CrossRef](#)]
107. Pan, J.; Xu, Y.Y.; Yang, H.; Dong, Z.H.; Liu, H.F.; Xia, B.Y. Advanced Architectures and Relatives of Air Electrodes in Zn-air Batteries. *Adv. Sci.* **2018**, *5*, 1700691. [[CrossRef](#)]
108. Cui, J.Y.; Li, Z.H.; Wang, G.R.; Guo, J.; Shao, M.F. Layered Double Hydroxides and Their Derivatives for Lithium-sulfur Batteries. *J. Mater. Chem. A* **2020**, *8*, 23738–23755. [[CrossRef](#)]
109. Jing, C.; Dong, B.Q.; Zhang, Y.X. Chemical Modifications of Layered Double Hydroxides in the Supercapacitor. *Energy Environ. Mater.* **2020**, *3*, 346–379. [[CrossRef](#)]
110. Subbaraman, R.; Tripkovic, D.; Chang, K.C.; Strmcnik, D.; Paulikas, A.P.; Hirunsit, P.; Chan, M.; Greeley, J.; Stamenkovic, V.; Markovic, N.M. Trends in Activity for the Water Electrolyser Reactions on 3d M(Ni,Co,Fe,Mn) Hydr(oxy)oxide Catalysts. *Nat. Mater.* **2012**, *11*, 550–557. [[CrossRef](#)]
111. Jiang, J.; Sun, F.F.; Zhou, S.; Hu, W.; Zhang, H.; Dong, J.C.; Jiang, Z.; Zhao, J.J.; Li, J.F.; Yan, W.S.; et al. Atomic-level Insight into Super-efficient Electrocatalytic Oxygen Evolution on Iron and Vanadium Co-doped Nickel (Oxy)hydroxide. *Nat. Commun.* **2018**, *9*, 2885. [[CrossRef](#)]
112. Chen, L.S.; Zhang, H.L.; Chen, L.; Wei, X.F.; Shi, J.L.; He, M.Y. Facile Synthesis of Cu Doped Cobalt Hydroxide (Cu-Co(OH)₂) Nano-sheets for Efficient Electrocatalytic Oxygen Evolution. *J. Mater. Chem. A* **2017**, *5*, 22568–22575. [[CrossRef](#)]
113. Zou, X.X.; Goswami, A.; Asefa, T. Efficient Noble Metal-Free (Electro)Catalysis of Water and Alcohol Oxidations by Zinc-Cobalt Layered Double Hydroxide. *J. Am. Chem. Soc.* **2013**, *135*, 17242–17245. [[CrossRef](#)] [[PubMed](#)]
114. Liu, J.Z.; Ji, Y.F.; Nai, J.W.; Niu, X.G.; Luo, Y.; Guo, L.; Yang, S.H. Ultrathin Amorphous Cobalt-Vanadium Hydr(oxy)oxide Catalysts for the Oxygen Evolution Reaction. *Energy Environ. Sci.* **2018**, *11*, 1736–1741. [[CrossRef](#)]
115. Xue, Z.; Zhang, X.Y.; Qin, J.Q.; Liu, R.P. Revealing Ni-based Layered Double Hydroxides as High-efficiency Electrocatalysts for the Oxygen Evolution Reaction: A DFT Study. *J. Mater. Chem. A* **2019**, *7*, 23091–23097. [[CrossRef](#)]
116. Gong, M.; Li, Y.G.; Wang, H.L.; Liang, Y.Y.; Wu, J.Z.; Zhou, J.G.; Wang, J.; Regier, T.; Wei, F.; Dai, H.J. An Advanced Ni-Fe Layered Double Hydroxide Electrocatalyst for Water Oxidation. *J. Am. Chem. Soc.* **2013**, *135*, 8452–8455. [[CrossRef](#)]
117. Louie, M.W.; Bell, A.T. An Investigation of Thin-film Ni-Fe Oxide Catalysts for the Electrochemical Evolution of Oxygen. *J. Am. Chem. Soc.* **2013**, *135*, 12329–12337. [[CrossRef](#)] [[PubMed](#)]
118. Trotochaud, L.; Young, S.L.; Ranney, J.K.; Boettcher, S.W. Nickel-Iron Oxyhydroxide Oxygen-evolution Electrocatalysts: The Role of Intentional and Incidental Iron Incorporation. *J. Am. Chem. Soc.* **2014**, *136*, 6744–6753. [[CrossRef](#)] [[PubMed](#)]
119. Diaz-Morales, O.; Ledezma-Yanez, I.; Koper, M.T.M.; Calle-Vallejo, F. Guidelines for the Rational Design of Ni-based Double Hydroxide Electrocatalysts for the Oxygen Evolution Reaction. *ACS Catal.* **2015**, *5*, 5380–5387. [[CrossRef](#)]
120. Friebel, D.; Louie, M.W.; Bajdich, M.; Sanwald, K.E.; Cai, Y.; Wise, A.M.; Cheng, M.J.; Sokaras, D.; Weng, T.C.; Alonso-Mori, R.; et al. Identification of Highly Active Fe Sites in (Ni,Fe)OOH for Electrocatalytic Water Splitting. *J. Am. Chem. Soc.* **2015**, *137*, 1305–1313. [[CrossRef](#)]
121. Chen, J.Y.C.; Dang, L.N.; Liang, H.F.; Bi, W.L.; Gerken, J.B.; Jin, S.; Alp, E.E.; Stahl, S.S. Operando Analysis of NiFe and Fe Oxyhydroxide Electrocatalysts for Water Oxidation: Detection of Fe⁴⁺ by Mössbauer Spectroscopy. *J. Am. Chem. Soc.* **2015**, *137*, 15090–15093. [[CrossRef](#)]
122. Ahn, H.S.; Bard, A.J. Surface Interrogation Scanning Electrochemical Microscopy of Ni_{1-x}Fe_xOOH (0 < x < 0.27) Oxygen Evolving Catalyst: Kinetics of the “Fast” Iron Sites. *J. Am. Chem. Soc.* **2016**, *138*, 313–318.
123. Gorlin, M.; Chernev, P.; Ferreira de Araujo, J.; Reier, T.; Dresp, S.; Paul, B.; Krahnert, R.; Dau, H.; Strasser, P. Oxygen Evolution Reaction Dynamics, Faradaic Charge Efficiency, and the Active Metal Redox States of Ni-Fe Oxide Water Splitting Electrocatalysts. *J. Am. Chem. Soc.* **2016**, *138*, 5603–5614. [[CrossRef](#)] [[PubMed](#)]
124. Li, N.; Bediako, D.K.; Hadt, R.G.; Hayes, D.; Kempa, T.J.; von Cube, F.; Bell, D.C.; Chen, L.X.; Nocera, D.G. Influence of Iron Doping on Tetravalent Nickel Content in Catalytic Oxygen Evolving Films. *Proc. Natl. Acad. Sci. USA* **2017**, *114*, 1486–1491. [[CrossRef](#)]
125. Hung, S.F.; Hsu, Y.Y.; Chang, C.J.; Hsu, C.S.; Suen, N.T.; Chan, T.S.; Chen, H.M. Unraveling Geometrical Site Confinement in Highly Efficient Iron-doped Electrocatalysts toward Oxygen Evolution Reaction. *Adv. Energy Mater.* **2018**, *8*, 1701686. [[CrossRef](#)]
126. Smith, R.D.; Prevot, M.S.; Fagan, R.D.; Trudel, S.; Berlinguette, C.P. Water Oxidation Catalysis: Electrocatalytic Response to Metal Stoichiometry in Amorphous Metal Oxide Films Containing Iron, Cobalt, and Nickel. *J. Am. Chem. Soc.* **2013**, *135*, 11580–11586. [[CrossRef](#)] [[PubMed](#)]
127. Qiu, Z.; Tai, C.W.; Niklasson, G.A.; Edvinsson, T. Direct Observation of Active Catalyst Surface Phases and the Effect of Dynamic Self-optimization in NiFe-Layered Double Hydroxides for Alkaline Water Splitting. *Energy Environ. Sci.* **2019**, *12*, 572–581. [[CrossRef](#)]
128. Zhou, D.J.; Cai, Z.; Jia, Y.; Xiong, X.Y.; Xie, Q.X.; Wang, S.Y.; Zhang, Y.; Liu, W.; Duan, H.H.; Sun, X. Activating Basal Plane in NiFe Layered Double Hydroxide by Mn²⁺ Doping for Efficient and Durable Oxygen Evolution Reaction. *Nanoscale Horiz.* **2018**, *3*, 532–537. [[CrossRef](#)] [[PubMed](#)]

129. Lu, Z.Y.; Qian, L.; Tian, Y.; Li, Y.P.; Sun, X.M.; Duan, X. Ternary NiFeMn Layered Double Hydroxides as Highly-efficient Oxygen Evolution Catalysts. *Chem. Commun.* **2016**, *52*, 908–911. [[CrossRef](#)]
130. Cai, Z.; Zhou, D.J.; Wang, M.Y.; Bak, S.M.; Wu, Y.S.; Wu, Z.S.; Tian, Y.; Xiong, X.Y.; Li, Y.P.; Liu, W.; et al. Introducing Fe²⁺ into Nickel-Iron Layered Double Hydroxide: Local Structure Modulated Water Oxidation Activity. *Angew. Chem. Int. Ed. Engl.* **2018**, *57*, 9392–9396. [[CrossRef](#)]
131. Thenuwara, A.C.; Attanayake, N.H.; Yu, J.; Perdew, J.P.; Elzinga, E.J.; Yan, Q.M.; Strongin, D.R. Cobalt Intercalated Layered NiFe Double Hydroxides for the Oxygen Evolution Reaction. *J. Phys. Chem. B* **2018**, *122*, 847–854. [[CrossRef](#)] [[PubMed](#)]
132. Bi, Y.M.; Cai, Z.; Zhou, D.J.; Tian, Y.; Zhang, Q.; Zhang, Q.; Kuang, Y.; Li, Y.P.; Sun, X.M.; Duan, X. Understanding the Incorporating Effect of Co²⁺/Co³⁺ in NiFe-Layered Double Hydroxide for Electrocatalytic Oxygen Evolution Reaction. *J. Catal.* **2018**, *358*, 100–107. [[CrossRef](#)]
133. Zhou, L.; Zhang, C.; Zhang, Y.Q.; Li, Z.H.; Shao, M.F. Host Modification of Layered Double Hydroxide Electrocatalyst to Boost the Thermodynamic and Kinetic Activity of Oxygen Evolution Reaction. *Adv. Funct. Mater.* **2021**, *31*, 2009743. [[CrossRef](#)]
134. Li, P.S.; Duan, X.X.; Kuang, Y.; Li, Y.P.; Zhang, G.X.; Liu, W.; Sun, X.M. Tuning Electronic Structure of NiFe Layered Double Hydroxides with Vanadium Doping toward High Efficient Electrocatalytic Water Oxidation. *Adv. Energy Mater.* **2018**, *8*, 1703341. [[CrossRef](#)]
135. Wen, L.L.; Zhang, X.L.; Liu, J.Y.; Li, X.Y.; Xing, C.C.; Lyu, X.J.; Cai, W.P.; Wang, W.C.; Li, Y. Cr-dopant Induced Breaking of Scaling Relations in CoFe Layered Double Hydroxides for Improvement of Oxygen Evolution Reaction. *Small* **2019**, *15*, 1902373. [[CrossRef](#)]
136. Wang, Z.L.; Liu, W.J.; Hu, Y.M.; Guan, M.L.; Xu, L.; Li, H.P.; Bao, J.; Li, H.M. Cr-doped CoFe Layered Double Hydroxides: Highly Efficient and Robust Bifunctional Electrocatalyst for the Oxidation of Water and Urea. *Appl. Catal. B Environ.* **2020**, *272*, 118959. [[CrossRef](#)]
137. Li, S.Z.; Liu, J.Y.; Duan, S.; Wang, T.Y.; Li, Q. Tuning the Oxygen Evolution Electrocatalysis on NiFe-Layered Double Hydroxides via Sulfur Doping. *Chin. J. Catal.* **2020**, *41*, 847–852. [[CrossRef](#)]
138. Zhang, B.W.; Jiang, K.; Wang, H.T.; Hu, S. Fluoride-induced Dynamic Surface Self-reconstruction Produces Unexpectedly Efficient Oxygen-evolution Catalyst. *Nano Lett.* **2019**, *19*, 530–537. [[CrossRef](#)]
139. Zheng, Y.; Gao, R.; Qiu, Y.S.; Zheng, L.R.; Hu, Z.B.; Liu, X.F. Tuning Co²⁺ Coordination in Cobalt Layered Double Hydroxide Nanosheets via Fe³⁺ Doping for Efficient Oxygen Evolution. *Inorg. Chem.* **2021**, *60*, 5252–5263. [[CrossRef](#)]
140. Jeghan, S.M.N.; Kim, J.; Lee, G. Hierarchically Designed CoMo Marigold Flower-like 3D Nano-heterostructure as an Efficient Electrocatalyst for Oxygen and Hydrogen Evolution Reactions. *Appl. Surf. Sci.* **2021**, *546*, 149072. [[CrossRef](#)]
141. Miyata, S. Anion Exchange Properties of Hydrotalcite-like Compounds. *Clays Clay Miner.* **1983**, *31*, 305–311. [[CrossRef](#)]
142. Hunter, B.M.; Hieringer, W.; Winkler, J.R.; Gray, H.B.; Müller, A.M. Effect of Interlayer Anions on [NiFe]-LDH Nanosheet Water Oxidation Activity. *Energy Environ. Sci.* **2016**, *9*, 1734–1743. [[CrossRef](#)]
143. Luo, M.; Cai, Z.; Wang, C.; Bi, Y.M.; Qian, L.; Hao, Y.C.; Li, L.; Kuang, Y.; Li, Y.P.; Lei, X.D.; et al. Phosphorus Oxoanion-intercalated Layered Double Hydroxides for High-performance Oxygen Evolution. *Nano Res.* **2017**, *10*, 1732–1739. [[CrossRef](#)]
144. Zhou, D.J.; Cai, Z.; Bi, Y.M.; Tian, W.L.; Luo, M.; Zhang, Q.; Zhang, Q.; Xie, Q.X.; Wang, J.D.; Li, Y.P.; et al. Effects of Redox-active Interlayer Anions on the Oxygen Evolution Reactivity of NiFe-Layered Double Hydroxide Nanosheets. *Nano Res.* **2018**, *11*, 1358–1368. [[CrossRef](#)]
145. Xu, Y.Q.; Hao, Y.C.; Zhang, G.X.; Lu, Z.Y.; Han, S.; Li, Y.P.; Sun, X.M. Room-temperature Synthetic NiFe Layered Double Hydroxide with Different Anions Intercalation as an Excellent Oxygen Evolution Catalyst. *RSC Adv.* **2015**, *5*, 55131–55135. [[CrossRef](#)]
146. Li, X.M.; Hao, X.G.; Wang, Z.D.; Abudula, A.; Guan, G.Q. In-situ Intercalation of NiFe LDH Materials: An Efficient Approach to Improve Electrocatalytic Activity and Stability for Water Splitting. *J. Power Sources* **2017**, *347*, 193–200. [[CrossRef](#)]
147. Dong, Y.; Komarneni, S.; Zhang, F.; Wang, N.; Terrones, M.; Hu, W.C.; Huang, W.Y. “Structural instability” Induced High-performance NiFe Layered Double Hydroxides as Oxygen Evolution Reaction Catalysts for pH-near-neutral Borate Electrolyte: The Role of Intercalates. *Appl. Catal. B Environ.* **2020**, *263*, 118343. [[CrossRef](#)]
148. Yang, M.Q.; Wang, J.; Wu, H.; Ho, G.W. Noble Metal-free Nanocatalysts with Vacancies for Electrochemical Water Splitting. *Small* **2018**, *14*, 1703323. [[CrossRef](#)]
149. Liu, Y.W.; Cheng, H.; Lyu, M.J.; Fan, S.J.; Liu, Q.H.; Zhang, W.S.; Zhi, Y.D.; Wang, C.M.; Xiao, C.; Wei, S.Q.; et al. Low Overpotential in Vacancy-rich Ultrathin CoSe₂ Nanosheets for Water Oxidation. *J. Am. Chem. Soc.* **2014**, *136*, 15670–15675. [[CrossRef](#)]
150. Yan, G.B.; Lian, Y.B.; Gu, Y.D.; Yang, C.; Sun, H.; Mu, Q.Q.; Li, Q.; Zhu, W.; Zheng, X.S.; Chen, M.Z.; et al. Phase and Morphology Transformation of MnO₂ Induced by Ionic Liquids toward Efficient Water Oxidation. *ACS Catal.* **2018**, *8*, 10137–10147. [[CrossRef](#)]
151. Zhou, D.J.; Xiong, X.Y.; Cai, Z.; Han, N.N.; Jia, Y.; Xie, Q.X.; Duan, X.X.; Xie, T.H.; Zheng, X.L.; Sun, X.M.; et al. Flame-engraved Nickel-Iron Layered Double Hydroxide Nanosheets for Boosting Oxygen Evolution Reactivity. *Small Methods* **2018**, *2*, 1800083. [[CrossRef](#)]
152. Zhou, Y.; Yan, D.F.; Gu, Q.F.; Zhu, S.H.; Wang, L.; Peng, H.G.; Zhao, Y. Implanting Cation Vacancies in Ni-Fe LDHs for Efficient Oxygen Evolution Reactions of Lithium-oxygen Batteries. *Appl. Catal. B Environ.* **2021**, *285*, 119792. [[CrossRef](#)]
153. Annenkov, M.; Blank, V.; Kulnitskiy, B.; Larionov, K.; Ovsyannikov, D.; Perezhogin, I.; Popov, M.; Sorokin, P. Boron Carbide Nanoparticles for High-hardness Ceramics: Crystal Lattice Defects after Treatment in a Planetary Ball Mill. *J. Eur. Ceram. Soc.* **2017**, *37*, 1349–1353. [[CrossRef](#)]

154. Wang, M.; Wang, J.Q.; Xi, C.; Cheng, C.Q.; Zou, C.Q.; Zhang, R.; Xie, Y.M.; Guo, Z.L.; Tang, C.C.; Dong, C.K.; et al. A Hydrogen-deficient Nickel-Cobalt Double Hydroxide for Photocatalytic Overall Water Splitting. *Angew. Chem. Int. Ed. Engl.* **2020**, *59*, 11510–11515. [[CrossRef](#)]
155. Xiong, X.Y.; Cai, Z.; Zhou, D.J.; Zhang, G.X.; Zhang, Q.; Jia, Y.; Duan, X.X.; Xie, Q.X.; Lai, S.B.; Xie, T.H.; et al. A Highly-efficient Oxygen Evolution Electrode Based on Defective Nickel-Iron Layered Double Hydroxide. *Sci. China Mater.* **2018**, *61*, 939–947. [[CrossRef](#)]
156. Xie, Y.S.; Wang, Z.; Ju, M.; Long, X.; Yang, S.H. Dispersing Transition Metal Vacancies in Layered Double Hydroxides by Ionic Reductive Complexation Extraction for Efficient Water Oxidation. *Chem. Sci.* **2019**, *10*, 8354–8359. [[CrossRef](#)]
157. Suntivich, J.; May, K.J.; Gasteiger, H.A.; Goodenough, J.B.; Shao-Horn, Y. A Perovskite Oxide Optimized for Oxygen Evolution Catalysis from Molecular Orbital Principles. *Science* **2011**, *334*, 1383–1385. [[CrossRef](#)] [[PubMed](#)]
158. Zhang, X.; Zhao, Y.F.; Zhao, Y.X.; Shi, R.; Waterhouse, G.I.N.; Zhang, T.R. A Simple Synthetic Strategy toward Defect-rich Porous Monolayer NiFe-Layered Double Hydroxide Nanosheets for Efficient Electrocatalytic Water Oxidation. *Adv. Energy Mater.* **2019**, *9*, 1900881. [[CrossRef](#)]
159. Zhou, P.; Wang, Y.Y.; Xie, C.; Chen, C.; Liu, H.W.; Chen, R.; Huo, J.; Wang, S.Y. Acid-etched Layered Double Hydroxides with Rich Defects for Enhancing the Oxygen Evolution Reaction. *Chem. Commun.* **2017**, *53*, 11778–11781. [[CrossRef](#)] [[PubMed](#)]
160. Song, F.; Hu, X. Exfoliation of Layered Double Hydroxides for Enhanced Oxygen Evolution Catalysis. *Nat. Commun.* **2014**, *5*, 4477. [[CrossRef](#)]
161. Nicolosi, V.; Chhowalla, M.; Kanatzidis, M.G.; Strano, M.S.; Coleman, J.N. Liquid Exfoliation of Layered Materials. *Science* **2013**, *340*, 1420–1439. [[CrossRef](#)]
162. Adachi-Pagano, M.; Forano, C.; Besse, J.P. Delamination of Layered Double Hydroxides by use of Surfactants. *Chem. Commun.* **2000**, 91–92. [[CrossRef](#)]
163. Jia, X.D.; Zhang, X.; Zhao, J.Q.; Zhao, Y.F.; Zhao, Y.X.; Waterhouse, G.I.N.; Shi, R.; Wu, L.Z.; Tung, C.H.; Zhang, T.R. Ultrafine Monolayer Co-containing Layered Double Hydroxide Nanosheets for Water Oxidation. *J. Energy Chem.* **2019**, *34*, 57–63. [[CrossRef](#)]
164. Chen, B.; Zhang, Z.; Kim, S.; Lee, S.; Lee, J.; Kim, W.; Yong, K. Ostwald Ripening Driven Exfoliation to Ultrathin Layered Double Hydroxides Nanosheets for Enhanced Oxygen Evolution Reaction. *ACS Appl. Mater. Interfaces* **2018**, *10*, 44518–44526. [[CrossRef](#)]
165. Wang, Y.Y.; Zhang, Y.Q.; Liu, Z.J.; Xie, C.; Feng, S.; Liu, D.D.; Shao, M.F.; Wang, S.Y. Layered Double Hydroxide Nanosheets with Multiple Vacancies Obtained by Dry Exfoliation as Highly Efficient Oxygen Evolution Electrocatalysts. *Angew. Chem. Int. Ed. Engl.* **2017**, *56*, 5867–5871. [[CrossRef](#)]
166. Liu, Z.J.; Dong, C.L.; Huang, Y.C.; Cen, J.J.; Yang, H.T.; Chen, X.B.; Tong, X.; Su, D.; Wang, Y.Y.; Wang, S.Y. Modulating the Electronic Structure of Ultrathin Layered Double Hydroxide Nanosheets with Fluorine: An Efficient Electrocatalyst for the Oxygen Evolution Reaction. *J. Mater. Chem. A* **2019**, *7*, 14483–14488. [[CrossRef](#)]
167. Hao, J.H.; Yang, W.S.; Peng, Z.; Zhang, C.; Huang, Z.P.; Shi, W.D. A Nitrogen Doping Method for CoS₂ Electrocatalysts with Enhanced Water Oxidation Performance. *ACS Catal.* **2017**, *7*, 4214–4220. [[CrossRef](#)]
168. Gao, R.; Yan, D.P. Fast Formation of Single-unit-cell-thick and Defect-rich Layered Double Hydroxide Nanosheets with Highly Enhanced Oxygen Evolution Reaction for Water Splitting. *Nano Res.* **2018**, *11*, 1883–1894. [[CrossRef](#)]
169. Zhou, P.; He, J.Y.; Zou, Y.Q.; Wang, Y.Y.; Xie, C.; Chen, R.; Zang, S.Q.; Wang, S.Y. Single-crystalline Layered Double Hydroxides with Rich Defects and Hierarchical Structure by Mild Reduction for Enhancing the Oxygen Evolution Reaction. *Sci. China Chem.* **2019**, *62*, 1365–1370. [[CrossRef](#)]
170. Zhao, Y.F.; Zhang, X.; Jia, X.D.; Waterhouse, G.I.N.; Shi, R.; Zhang, X.R.; Zhan, F.; Tao, Y.; Wu, L.Z.; Tung, C.H.; et al. Sub-3 nm Ultrafine Monolayer Layered Double Hydroxide Nanosheets for Electrochemical Water Oxidation. *Adv. Energy Mater.* **2018**, *8*, 1703585. [[CrossRef](#)]
171. Kuai, C.G.; Zhang, Y.; Wu, D.Y.; Sokaras, D.; Mu, L.Q.; Spence, S.; Nordlund, D.; Lin, F.; Du, X.W. Fully Oxidized Ni-Fe Layered Double Hydroxide with 100% Exposed Active Sites for Catalyzing Oxygen Evolution Reaction. *ACS Catal.* **2019**, *9*, 6027–6032. [[CrossRef](#)]
172. Zhong, H.H.; Liu, T.Y.; Zhang, S.W.; Li, D.Q.; Tang, P.G.; Alonso-Vante, N.; Feng, Y.J. Template-free Synthesis of Three-dimensional NiFe-LDH Hollow Microsphere with Enhanced OER Performance in Alkaline Media. *J. Energy Chem.* **2019**, *33*, 130–137. [[CrossRef](#)]
173. Zhang, C.; Shao, M.F.; Zhou, L.; Li, Z.H.; Xiao, K.M.; Wei, M. Hierarchical NiFe Layered Double Hydroxide Hollow Microspheres with Highly-efficient Behavior toward Oxygen Evolution Reaction. *ACS Appl. Mater. Interfaces* **2016**, *8*, 33697–33703. [[CrossRef](#)] [[PubMed](#)]
174. Yu, L.; Yang, J.F.; Guan, B.Y.; Lu, Y.; Lou, X.W. Hierarchical Hollow Nanoprisms Based on Ultrathin Ni-Fe Layered Double Hydroxide Nanosheets with Enhanced Electrocatalytic Activity towards Oxygen Evolution. *Angew. Chem. Int. Ed. Engl.* **2018**, *57*, 172–176. [[CrossRef](#)]
175. Xu, H.J.; Shan, C.F.; Wu, X.X.; Sun, M.Z.; Huang, B.L.; Tang, Y.; Yan, C.H. Fabrication of Layered Double Hydroxide Microcapsules Mediated by Cerium Doping in Metal-Organic Frameworks for Boosting Water Splitting. *Energy Environ. Sci.* **2020**, *13*, 2949–2956. [[CrossRef](#)]
176. Zhu, K.Y.; Chen, J.J.; Wang, W.J.; Liao, J.W.; Dong, J.C.; Chee, M.O.L.; Wang, N.; Dong, P.; Ajayan, P.M.; Gao, S.P.; et al. Etching-doping Sedimentation Equilibrium Strategy: Accelerating Kinetics on Hollow Rh-doped CoFe-Layered Double Hydroxides for Water Splitting. *Adv. Funct. Mater.* **2020**, *30*, 2003556. [[CrossRef](#)]

177. Tang, C.; Wang, H.F.; Zhu, X.L.; Li, B.Q.; Zhang, Q. Advances in Hybrid Electrocatalysts for Oxygen Evolution Reactions: Rational Integration of NiFe Layered Double Hydroxides and Nanocarbon. *Part. Part. Syst. Charact.* **2016**, *33*, 473–486. [[CrossRef](#)]
178. Guo, X.L.; Zheng, X.Q.; Hu, X.L.; Zhao, Q.N.; Li, L.; Yu, P.; Jing, C.; Zhang, Y.X.; Huang, G.S.; Jiang, B.; et al. Electrostatic Adsorbing Graphene Quantum Dot into Nickel-based Layered Double Hydroxides: Electron Absorption/donor Effects Enhanced Oxygen Electrocatalytic Activity. *Nano Energy* **2021**, *84*, 105932. [[CrossRef](#)]
179. Li, J.; Gao, X.; Li, Z.Z.; Wang, J.H.; Zhu, L.; Yin, C.; Wang, Y.; Li, X.B.; Liu, Z.F.; Zhang, J.; et al. Superhydrophilic Graphdiyne Accelerates Interfacial Mass/Electron Transportation to Boost Electrocatalytic and Photoelectrocatalytic Water Oxidation Activity. *Adv. Funct. Mater.* **2019**, *29*, 1808079. [[CrossRef](#)]
180. Zhang, J.F.; Liu, J.Y.; Xi, L.F.; Yu, Y.F.; Chen, N.; Sun, S.H.; Wang, W.C.; Lange, K.M.; Zhang, B. Single-atom Au/NiFe Layered Double Hydroxide Electrocatalyst: Probing the Origin of Activity for Oxygen Evolution Reaction. *J. Am. Chem. Soc.* **2018**, *140*, 3876–3879. [[CrossRef](#)] [[PubMed](#)]
181. Yu, L.; Zhou, H.Q.; Sun, J.Y.; Qin, F.; Yu, F.; Bao, J.M.; Yu, Y.; Chen, S.; Ren, Z.F. Cu Nanowires Shelled with NiFe Layered Double Hydroxide Nanosheets as Bifunctional Electrocatalysts for Overall Water Splitting. *Energy Environ. Sci.* **2017**, *10*, 1820–1827. [[CrossRef](#)]
182. Wan, L.; Zhao, Z.H.; Chen, X.X.; Liu, P.F.; Wang, P.C.; Xu, Z.; Lin, Y.Q.; Wang, B.G. Controlled Synthesis of Bifunctional NiCo₂O₄@FeNi LDH Core-shell Nanoarray Air Electrodes for Rechargeable Zinc-air Batteries. *ACS Sustain. Chem. Eng.* **2020**, *8*, 11079–11087. [[CrossRef](#)]
183. He, K.; Tadesse Tsega, T.; Liu, X.; Zai, J.T.; Li, X.H.; Liu, X.J.; Li, W.H.; Ali, N.; Qian, X.F. Utilizing the Space-charge Region of the FeNi-LDH/CoP *p-n* Junction to Promote Performance in Oxygen Evolution Electrocatalysis. *Angew. Chem. Int. Ed. Engl.* **2019**, *58*, 11903–11909. [[CrossRef](#)]
184. Gao, Z.W.; Liu, J.Y.; Chen, X.M.; Zheng, X.L.; Mao, J.; Liu, H.; Ma, T.; Li, L.; Wang, W.C.; Du, X.W. Engineering NiO/NiFe LDH Intersection to Bypass Scaling Relationship for Oxygen Evolution Reaction via Dynamic Tridimensional Adsorption of Intermediates. *Adv. Mater.* **2019**, *31*, 1804769. [[CrossRef](#)] [[PubMed](#)]
185. Liu, J.; Wang, J.S.; Zhang, B.; Ruan, Y.J.; Lv, L.; Ji, X.; Xu, K.; Miao, L.; Jiang, J.J. Hierarchical NiCo₂S₄@NiFe LDH Heterostructures Supported on Nickel Foam for Enhanced Overall-Water-Splitting Activity. *ACS Appl. Mater. Interfaces* **2017**, *9*, 15364–15372. [[CrossRef](#)]
186. Yu, M.Z.; Wang, Z.Y.; Liu, J.S.; Sun, F.; Yang, P.J.; Qiu, J.S. A Hierarchically Porous and Hydrophilic 3D Nickel-Iron/MXene Electrode for Accelerating Oxygen and Hydrogen Evolution at High Current Densities. *Nano Energy* **2019**, *63*, 103880. [[CrossRef](#)]
187. Yang, Y.; Dang, L.N.; Shearer, M.J.; Sheng, H.Y.; Li, W.J.; Chen, J.; Xiao, P.; Zhang, Y.H.; Hamers, R.J.; Jin, S. Highly Active Trimetallic NiFeCr Layered Double Hydroxide Electrocatalysts for Oxygen Evolution Reaction. *Adv. Energy Mater.* **2018**, *8*, 1703189. [[CrossRef](#)]
188. Li, R.S.; Wang, Y.H.; Li, W.; Zhou, S.Y.; Tian, P.F.; Gao, H.W.; Liu, X.Y.; Zang, J.B. Ternary NiFeZr Layered Double Hydroxides: A Highly Efficient Catalyst for the Oxygen Evolution Reaction. *Chem. Commun.* **2019**, *55*, 13370–13373. [[CrossRef](#)]
189. Wang, D.W.; Li, Q.; Han, C.; Lu, Q.Q.; Xing, Z.C.; Yang, X.R. Atomic and Electronic Modulation of Self-supported Nickel-Vanadium Layered Double Hydroxide to Accelerate Water Splitting Kinetics. *Nat. Commun.* **2019**, *10*, 3899. [[CrossRef](#)] [[PubMed](#)]
190. Li, S.; Xi, C.; Jin, Y.Z.; Wu, D.Y.; Wang, J.Q.; Liu, T.; Wang, H.B.; Dong, C.K.; Liu, H.; Kulinich, S.A.; et al. Ir-O-V Catalytic Group in Ir-doped NiV(OH)₂ for Overall Water Splitting. *ACS Energy Lett.* **2019**, *4*, 1823–1829. [[CrossRef](#)]
191. Hao, S.Y.; Zheng, G.K.; Gao, S.J.; Qiu, L.S.; Xu, N.; He, Y.; Lei, L.C.; Zhang, X.W. In Situ Synthesis of Ternary NiCoRu-based Layered Double Hydroxide by Chlorine Corrosion toward Electrocatalytic Water Oxidation. *ACS Sustain. Chem. Eng.* **2019**, *7*, 14361–14367. [[CrossRef](#)]
192. Hu, Y.M.; Wang, Z.L.; Liu, W.J.; Xu, L.; Guan, M.L.; Huang, Y.P.; Zhao, Y.; Bao, J.; Li, H.M. Novel Cobalt-Iron-Vanadium Layered Double Hydroxide Nanosheet Arrays for Superior Water Oxidation Performance. *ACS Sustain. Chem. Eng.* **2019**, *7*, 16828–16834. [[CrossRef](#)]
193. Bo, X.; Li, Y.B.; Chen, X.J.; Zhao, C. High Valence Chromium Regulated Cobalt-Iron-hydroxide for Enhanced Water Oxidation. *J. Power Sources* **2018**, *402*, 381–387. [[CrossRef](#)]
194. Pi, Y.C.; Shao, Q.; Wang, P.T.; Lv, F.; Guo, S.J.; Guo, J.; Huang, X.Q. Trimetallic Oxyhydroxide Coralloids for Efficient Oxygen Evolution Electrocatalysis. *Angew. Chem. Int. Ed. Engl.* **2017**, *56*, 4502–4506. [[CrossRef](#)]
195. Bao, J.; Wang, Z.L.; Xie, J.F.; Xu, L.; Lei, F.C.; Guan, M.L.; Zhao, Y.; Huang, Y.P.; Li, H.M. A Ternary Cobalt-Molybdenum-Vanadium Layered Double Hydroxide Nanosheet Array as an Efficient Bifunctional Electrocatalyst for Overall Water Splitting. *Chem. Commun.* **2019**, *55*, 3521–3524. [[CrossRef](#)] [[PubMed](#)]
196. Nejati, K.; Akbari, A.R.; Davari, S.; Asadpour-Zeynali, K.; Rezvani, Z. Zn-Fe-Layered Double Hydroxide Intercalated with Vanadate and Molybdate Anions for Electrocatalytic Water Oxidation. *New J. Chem.* **2018**, *42*, 2889–2895. [[CrossRef](#)]
197. Xue, X.Y.; Yu, F.; Peng, B.H.; Wang, G.; Lv, Y.; Chen, L.; Yao, Y.B.; Dai, B.; Shi, Y.L.; Guo, X.H. One-step Synthesis of Nickel-Iron Layered Double Hydroxides with Tungstate Acid Anions via Flash Nano-precipitation for the Oxygen Evolution Reaction. *Sustain. Energy Fuels* **2019**, *3*, 237–244. [[CrossRef](#)]
198. Xue, X.Y.; Yu, F.; Li, J.G.; Bai, G.; Yuan, H.F.; Hou, J.; Peng, B.H.; Chen, L.; Yuen, M.F.; Wang, G.; et al. Polyoxometalate Intercalated NiFe Layered Double Hydroxides for Advanced Water Oxidation. *Int. J. Hydrogen Energy* **2020**, *45*, 1802–1809. [[CrossRef](#)]
199. Su, L.; Du, H.F.; Tang, C.; Nan, K.K.; Wu, J.G.; Li, C.M. Borate-ion Intercalated NiFe Layered Double Hydroxide to Simultaneously Boost Mass Transport and Charge Transfer for Catalysis of Water Oxidation. *J. Colloid Interface Sci.* **2018**, *528*, 36–44. [[CrossRef](#)]

200. Xie, Q.X.; Cai, Z.; Li, P.S.; Zhou, D.J.; Bi, Y.M.; Xiong, X.Y.; Hu, E.Y.; Li, Y.P.; Kuang, Y.; Sun, X.M. Layered Double Hydroxides with Atomic-scale Defects for Superior Electrocatalysis. *Nano Res.* **2018**, *11*, 4524–4534. [[CrossRef](#)]
201. Wang, Y.Y.; Xie, C.; Zhang, Z.Y.; Liu, D.D.; Chen, R.; Wang, S.Y. In Situ Exfoliated, N-doped, and Edge-rich Ultrathin Layered Double Hydroxides Nanosheets for Oxygen Evolution Reaction. *Adv. Funct. Mater.* **2018**, *28*, 1703363. [[CrossRef](#)]
202. Long, X.; Li, J.K.; Xiao, S.; Yan, K.Y.; Wang, Z.L.; Chen, H.N.; Yang, S.H. A Strongly Coupled Graphene and FeNi Double Hydroxide Hybrid as an Excellent Electrocatalyst for the Oxygen Evolution Reaction. *Angew. Chem. Int. Ed. Engl.* **2014**, *53*, 7584–7588. [[CrossRef](#)] [[PubMed](#)]
203. Jia, Y.; Zhang, L.Z.; Gao, G.P.; Chen, H.; Wang, B.; Zhou, J.Z.; Soo, M.T.; Hong, M.; Yan, X.C.; Qian, G.R.; et al. A Heterostructure Coupling of Exfoliated Ni-Fe Hydroxide Nanosheet and Defective Graphene as a Bifunctional Electrocatalyst for Overall Water Splitting. *Adv. Mater.* **2017**, *29*, 1700017. [[CrossRef](#)] [[PubMed](#)]
204. Xu, H.J.; Wang, B.K.; Shan, C.F.; Xi, P.X.; Liu, W.S.; Tang, Y. Ce-doped NiFe-Layered Double Hydroxide Ultrathin Nanosheets/Nanocarbon Hierarchical Nanocomposite as an Efficient Oxygen Evolution Catalyst. *ACS Appl. Mater. Interfaces* **2018**, *10*, 6336–6345. [[CrossRef](#)]
205. Zhang, X.; Marianov, A.N.; Jiang, Y.J.; Cazorla, C.; Chu, D.W. Hierarchically Constructed Silver Nanowire@Nickel-Iron Layered Double Hydroxide Nanostructures for Electrocatalytic Water Splitting. *ACS Appl. Nano Mater.* **2019**, *3*, 887–895. [[CrossRef](#)]
206. Xiang, Q.; Li, F.; Chen, W.L.; Ma, Y.L.; Wu, Y.; Gu, X.; Qin, Y.; Tao, P.; Song, C.Y.; Shang, W.; et al. In Situ Vertical Growth of Fe-Ni Layered Double-Hydroxide Arrays on Fe-Ni Alloy Foil: Interfacial Layer Enhanced Electrocatalyst with Small Overpotential for Oxygen Evolution Reaction. *ACS Energy Lett.* **2018**, *3*, 2357–2365. [[CrossRef](#)]
207. Wang, L.; Huang, X.L.; Jiang, S.S.; Li, M.; Zhang, K.; Yan, Y.; Zhang, H.P.; Xue, J.M. Increasing Gas Bubble Escape Rate for Water Splitting with Nonwoven Stainless Steel Fabrics. *ACS Appl. Mater. Interfaces* **2017**, *9*, 40281–40289. [[CrossRef](#)]
208. Chen, J.D.; Zheng, F.; Zhang, S.J.; Fisher, A.; Zhou, Y.; Wang, Z.y.; Li, Y.y.; Xu, B.B.; Li, J.T.; Sun, S.G. Interfacial Interaction between FeOOH and Ni-Fe LDH to Modulate the Local Electronic Structure for Enhanced OER Electrocatalysis. *ACS Catal.* **2018**, *8*, 11342–11351. [[CrossRef](#)]
209. Yang, L.T.; Chen, L.; Yang, D.W.; Yu, X.; Xue, H.G.; Feng, L.G. NiMn Layered Double Hydroxide Nanosheets/NiCo₂O₄ Nanowires with Surface Rich High Valence State Metal Oxide as an Efficient Electrocatalyst for Oxygen Evolution Reaction. *J. Power Sources* **2018**, *392*, 23–32. [[CrossRef](#)]
210. Liang, Z.; Zhou, P.; Wang, Z.Y.; Wang, P.; Liu, Y.Y.; Qin, X.Y.; Zhang, X.Y.; Dai, Y.; Zheng, Z.K.; Huang, B.B. Electrodeposition of NiFe Layered Double Hydroxide on Ni₃S₂ Nanosheets for Efficient Electrocatalytic Water Oxidation. *Int. J. Hydrogen Energy* **2020**, *45*, 8659–8666. [[CrossRef](#)]
211. Zou, Y.J.; Xiao, B.; Shi, J.W.; Hao, H.; Ma, D.D.; Lv, Y.X.; Sun, G.T.; Li, J.; Cheng, Y.H. 3D Hierarchical Heterostructure Assembled by NiFe LDH/(NiFe)_x on Biomass-derived Hollow Carbon Microtubes as Bifunctional Electrocatalysts for Overall Water Splitting. *Electrochim. Acta* **2020**, *348*, 136339. [[CrossRef](#)]
212. Yu, L.; Zhou, H.Q.; Sun, J.Y.; Mishra, I.K.; Luo, D.; Yu, F.; Yu, Y.; Chen, S.; Ren, Z.F. Amorphous NiFe layered double hydroxide nanosheets decorated on 3D nickel phosphide nanoarrays: A hierarchical core-shell electrocatalyst for efficient oxygen evolution. *J. Mater. Chem. A* **2018**, *6*, 13619–13623. [[CrossRef](#)]
213. Yu, M.Z.; Zhou, S.; Wang, Z.Y.; Zhao, J.J.; Qiu, J.S. Boosting Electrocatalytic Oxygen Evolution by Synergistically Coupling Layered Double Hydroxide with MXene. *Nano Energy* **2018**, *44*, 181–190. [[CrossRef](#)]
214. Tian, M.; Jiang, Y.; Tong, H.L.; Xu, Y.M.; Xia, L.X. MXene-supported FeCo-LDHs as Highly Efficient Catalysts for Enhanced Electrocatalytic Oxygen Evolution Reaction. *ChemNanoMat* **2019**, *6*, 154–159. [[CrossRef](#)]
215. Chala, S.A.; Tsai, M.C.; Su, W.N.; Ibrahim, K.B.; Thirumalraj, B.; Chan, T.S.; Lee, J.F.; Dai, H.J.; Hwang, B.J. Hierarchical 3D Architected Ag Nanowires Shelled with NiMn-Layered Double Hydroxide as an Efficient Bifunctional Oxygen Electrocatalyst. *ACS Nano* **2020**, *14*, 1770–1782. [[CrossRef](#)]
216. Chala, S.A.; Tsai, M.C.; Su, W.N.; Ibrahim, K.B.; Duma, A.D.; Yeh, M.H.; Wen, C.Y.; Yu, C.H.; Chan, T.S.; Dai, H.J.; et al. Site Activity and Population Engineering of NiRu-Layered Double Hydroxide Nanosheets Decorated with Silver Nanoparticles for Oxygen Evolution and Reduction Reactions. *ACS Catal.* **2019**, *9*, 117–129. [[CrossRef](#)]
217. Wang, P.C.; Lin, Y.Q.; Wan, L.; Wang, B.G. Construction of a Janus MnO₂-NiFe Electrode via Selective Electrodeposition Strategy as a High-performance Bifunctional Electrocatalyst for Rechargeable Zinc-air Batteries. *ACS Appl. Mater. Interfaces* **2019**, *11*, 37701–37707. [[CrossRef](#)]
218. Zhou, D.J.; Cai, Z.; Lei, X.D.; Tian, W.L.; Bi, Y.M.; Jia, Y.; Han, N.N.; Gao, T.F.; Zhang, Q.; Kuang, Y.; et al. NiCoFe-Layered Double Hydroxides/N-doped Graphene Oxide Array Colloid Composite as an Efficient Bifunctional Catalyst for Oxygen Electrocatalytic Reactions. *Adv. Energy Mater.* **2018**, *8*, 1701905. [[CrossRef](#)]
219. Sun, F.C.; Zhou, Y.; You, Z.H.; Xia, H.H.; Tuo, Y.X.; Wang, S.T.; Jia, C.P.; Zhang, J. Bi-functional Fe₃O₄/Au/CoFe-LDH Sandwich-structured Electrocatalyst for Asymmetrical Electrolyzer with Low Operation Voltage. *Small* **2021**. [[CrossRef](#)]
220. Wang, Q.; Shang, L.; Shi, R.; Zhang, X.; Zhao, Y.F.; Waterhouse, G.I.N.; Wu, L.Z.; Tung, C.H.; Zhang, T.R. NiFe Layered Double Hydroxide Nanoparticles on Co,N-codoped Carbon Nanoframes as Efficient Bifunctional Catalysts for Rechargeable Zinc-air Batteries. *Adv. Energy Mater.* **2017**, *7*, 1700467. [[CrossRef](#)]
221. Wang, T.T.; Wu, J.H.; Liu, Y.L.; Cui, X.; Ding, P.; Deng, J.; Zha, C.Y.; Coy, E.; Li, Y.G. Scalable Preparation and Stabilization of Atomic-thick CoNi Layered Double Hydroxide Nanosheets for Bifunctional Oxygen Electrocatalysis and Rechargeable Zinc-air Batteries. *Energy Storage Mater.* **2019**, *16*, 24–30. [[CrossRef](#)]

222. Li, Y.; Zhao, M.J.; Zhao, Y.; Song, L.; Zhang, Z.P. FeNi Layered Double Hydroxide Nanosheets on a 3D Carbon Network as an Efficient Electrocatalyst for the Oxygen Evolution Reaction. *Part. Part. Syst. Charact.* **2016**, *33*, 158–166. [\[CrossRef\]](#)
223. Li, Z.S.; Xiao, K.C.; Yu, C.L.; Wang, H.Q.; Li, Q.Y. Three-dimensional Graphene-like Carbon Nanosheets Coupled with MnCo-Layered Double Hydroxides Nanoflowers as Efficient Bifunctional Oxygen Electrocatalyst. *Int. J. Hydrogen Energy* **2021**, *46*, 34239–34251. [\[CrossRef\]](#)
224. Zhan, T.R.; Zhang, Y.M.; Liu, X.L.; Lu, S.S.; Hou, W.G. NiFe Layered Double Hydroxide/Reduced Graphene Oxide Nanohybrid as an Efficient Bifunctional Electrocatalyst for Oxygen Evolution and Reduction Reactions. *J. Power Sources* **2016**, *333*, 53–60. [\[CrossRef\]](#)
225. Zhan, T.R.; Liu, X.L.; Lu, S.S.; Hou, W.G. Nitrogen Doped NiFe Layered Double Hydroxide/Reduced Graphene Oxide Mesoporous Nanosphere as an Effective Bifunctional Electrocatalyst for Oxygen Reduction and Evolution Reactions. *Appl. Catal. B Environ.* **2017**, *205*, 551–558. [\[CrossRef\]](#)
226. Zhang, G.Q.; Xing, J.Y.; Zhao, Y.Y.; Yang, F.L. Hierarchical N,P Co-doped Graphene Aerogels Framework Assembling Vertically Grown CoMn-LDH Nanosheets as Efficient Bifunctional Electrocatalyst for Rechargeable Zinc-air Battery. *J. Colloid Interface Sci.* **2021**, *590*, 476–486. [\[CrossRef\]](#)
227. Wang, Z.J.; Lu, Y.Z.; Yan, Y.; Larissa, T.Y.P.; Zhang, X.; Wu, D.; Zhang, H.; Yang, Y.H.; Wang, X. Core-shell Carbon Materials Derived from Metal-Organic Frameworks as an Efficient Oxygen Bifunctional Electrocatalyst. *Nano Energy* **2016**, *30*, 368–378. [\[CrossRef\]](#)
228. Yin, P.Q.; Yao, T.; Wu, Y.E.; Zheng, L.R.; Lin, Y.; Liu, W.; Ju, H.X.; Zhu, J.F.; Hong, X.; Deng, Z.X.; et al. Single Cobalt Atoms with Precise N-coordination as Superior Oxygen Reduction Reaction Catalysts. *Angew. Chem. Int. Ed. Engl.* **2016**, *55*, 10800–10805. [\[CrossRef\]](#)
229. Shang, L.; Yu, H.J.; Huang, X.; Bian, T.; Shi, R.; Zhao, Y.F.; Waterhouse, G.I.N.; Wu, L.Z.; Tung, C.H.; Zhang, T.R. Well-dispersed ZIF-derived Co,N-co-doped Carbon Nanoframes through Mesoporous-silica-protected Calcination as Efficient Oxygen Reduction Electrocatalysts. *Adv. Mater.* **2016**, *28*, 1668–1674. [\[CrossRef\]](#)
230. Zhao, C.X.; Liu, J.N.; Li, B.Q.; Ren, D.; Chen, X.; Yu, J.; Zhang, Q. Multiscale Construction of Bifunctional Electrocatalysts for Long-lifespan Rechargeable Zinc-air Batteries. *Adv. Funct. Mater.* **2020**, *30*, 2003619. [\[CrossRef\]](#)
231. Zhao, C.X.; Liu, J.N.; Wang, J.; Ren, D.; Yu, J.; Chen, X.; Li, B.Q.; Zhang, Q. A $\Delta E = 0.63$ V Bifunctional Oxygen Electrocatalyst Enables High-rate and Long-cycling Zinc-air Batteries. *Adv. Mater.* **2021**, *33*, 2008606. [\[CrossRef\]](#)
232. Yang, R.; Zhou, Y.M.; Xing, Y.Y.; Li, D.; Jiang, D.L.; Chen, M.; Shi, W.D.; Yuan, S.Q. Synergistic Coupling of CoFe-LDH Arrays with NiFe-LDH Nanosheet for Highly Efficient Overall Water Splitting in Alkaline Media. *Appl. Catal. B Environ.* **2019**, *253*, 131–139. [\[CrossRef\]](#)
233. Zhong, H.H.; Tian, R.; Gong, X.M.; Li, D.Q.; Tang, P.G.; Alonso-Vante, N.; Feng, Y.J. Advanced Bifunctional Electrocatalyst Generated through Cobalt Phthalocyanine Tetrasulfonate Intercalated Ni₂Fe-Layered Double Hydroxides for a Laminar Flow Unitized Regenerative Micro-cell. *J. Power Sources* **2017**, *361*, 21–30. [\[CrossRef\]](#)
234. Fan, K.; Li, Z.H.; Song, Y.J.; Xie, W.F.; Shao, M.F.; Wei, M. Confinement Synthesis Based on Layered Double Hydroxides: A New Strategy to Construct Single-atom-containing Integrated Electrodes. *Adv. Funct. Mater.* **2020**, *31*, 2008064. [\[CrossRef\]](#)
235. Fu, G.T.; Cui, Z.M.; Chen, Y.F.; Xu, L.; Tang, Y.W.; Goodenough, J.B. Hierarchically Mesoporous Nickel-Iron Nitride as a Cost-efficient and Highly Durable Electrocatalyst for Zn-air Battery. *Nano Energy* **2017**, *39*, 77–85. [\[CrossRef\]](#)
236. Gao, D.Q.; Zhang, J.Y.; Wang, T.T.; Xiao, W.; Tao, K.; Xue, D.S.; Ding, J. Metallic Ni₃N Nanosheets with Exposed Active Surface Sites for Efficient Hydrogen Evolution. *J. Mater. Chem. A* **2016**, *4*, 17363–17369. [\[CrossRef\]](#)
237. Sun, Z.M.; Zhang, J.Y.; Xie, J.F.; Zheng, X.J.; Wang, M.; Li, X.M.; Tang, B. High-performance Alkaline Hydrogen Evolution Electrocatalyzed by a Ni₃N-CeO₂ Nanohybrid. *Inorg. Chem. Front.* **2018**, *5*, 3042–3045. [\[CrossRef\]](#)
238. Wang, B.R.; Jiao, S.H.; Wang, Z.S.; Lu, M.J.; Chen, D.; Kang, Y.T.; Pang, G.S.; Feng, S.H. Rational Design of NiFe LDH@Ni₃N Nano/Microsheet Arrays as a Bifunctional Electrocatalyst for Overall Water Splitting. *J. Mater. Chem. A* **2020**, *8*, 17202–17211. [\[CrossRef\]](#)
239. Wang, Q.; Shang, L.; Shi, R.; Zhang, X.; Waterhouse, G.I.N.; Wu, L.Z.; Tung, C.H.; Zhang, T.R. 3D Carbon Nanoframe Scaffold-immobilized Ni₃FeN Nanoparticle Electrocatalysts for Rechargeable Zinc-air Batteries' Cathodes. *Nano Energy* **2017**, *40*, 382–389. [\[CrossRef\]](#)
240. Wang, H.F.; Tang, C.; Wang, B.; Li, B.Q.; Zhang, Q. Bifunctional Transition Metal Hydroxysulfides: Room-temperature Sulfurization and Their Applications in Zn-air Batteries. *Adv. Mater.* **2017**, *29*, 1702327. [\[CrossRef\]](#)
241. Han, X.T.; Li, N.N.; Kang, Y.B.; Dou, Q.Y.; Xiong, P.X.; Liu, Q.; Lee, J.Y.; Dai, L.M.; Park, H.S. Unveiling Trifunctional Active Sites of a Heteronanoshet Electrocatalyst for Integrated Cascade Battery/Electrolyzer Systems. *ACS Energy Lett.* **2021**, *6*, 2460–2468. [\[CrossRef\]](#)
242. Qian, L.; Lu, Z.Y.; Xu, T.H.; Wu, X.C.; Tian, Y.; Li, Y.P.; Huo, Z.Y.; Sun, X.M.; Duan, X. Ternary Layered Double Hydroxides as High-performance Bifunctional Materials for Oxygen Electrocatalysis. *Adv. Energy Mater.* **2015**, *5*, 1500245. [\[CrossRef\]](#)
243. Dresch, S.; Luo, F.; Schmack, R.; Kuhl, S.; Glich, M.; Strasser, P. An Efficient Bifunctional Two-component Catalyst for Oxygen Reduction and Oxygen Evolution in Reversible Fuel Cells, Electrolyzers and Rechargeable Air Electrodes. *Energy Environ. Sci.* **2016**, *9*, 2020–2024. [\[CrossRef\]](#)

244. Jia, X.D.; Gao, S.J.; Liu, T.Y.; Li, D.Q.; Tang, P.G.; Feng, Y.J. Fabrication and Bifunctional Electrocatalytic Performance of Ternary CoNiMn Layered Double Hydroxides/Polypyrrole/Reduced Graphene Oxide Composite for Oxygen Reduction and Evolution Reactions. *Electrochim. Acta* **2017**, *245*, 51–60. [[CrossRef](#)]
245. Guo, X.L.; Hu, X.L.; Wu, D.; Jing, C.; Liu, W.; Ren, Z.L.; Zhao, Q.N.; Jiang, X.P.; Xu, C.H.; Zhang, Y.X.; et al. Tuning the Bifunctional Oxygen Electrocatalytic Properties of Core-shell Co₃O₄@NiFe LDH Catalysts for Zn-air Batteries: Effects of Interfacial Cation Valences. *ACS Appl. Mater. Interfaces* **2019**, *11*, 21506–21514. [[CrossRef](#)] [[PubMed](#)]
246. Liu, Q.; Liu, X.; Xie, Y.; Sun, F.F.; Liang, Z.J.; Wang, L.; Fu, H.G. N-doped Carbon Coating Enhances the Bifunctional Oxygen Reaction Activity of CoFe Nanoparticles for a Highly Stable Zn-air Battery. *J. Mater. Chem. A* **2020**, *8*, 21189–21198. [[CrossRef](#)]
247. Li, S.J.; Xie, W.F.; Song, Y.K.; Shao, M.F. Layered Double Hydroxide@Polydopamine Core-shell Nanosheet Arrays-derived Bifunctional Electrocatalyst for Efficient, Flexible, All-solid-state Zinc-air Battery. *ACS Sustain. Chem. Eng.* **2020**, *8*, 452–459. [[CrossRef](#)]